Raymond P. Mariella, Jr., Center Director

The mission of the Center for Microtechnology is to invent, develop, and apply microtechnologies with the Lawrence Livermore National Laboratory (LLNL) programs in global security, global ecology, and bioscience.

Our capabilities cover materials, fabrication, devices, instruments, or systems which require microfabricated components, including microelectro-mechanical systems (MEMS), electronics, photonics, microstructures, and microactuators. Much of our microtechnology work revolves around our microfabrication facility. We also rely upon LLNL's precision manufacturing and characterization facilities in plastics and glass. Moreover, we incorporate modeling to assist the design of our instruments. An example of this is the report on the experimental testing and theoretical modeling of highly-filled polymers.

Our work is driven principally by the applications of LLNL programs, and, to a lesser extent, by external applications. For both of these we must have multi-disciplinary teams to deliver complete solutions to the problems. The Center for Microtechnology includes more than 60 people, who have training in electronics engineering, mechanical engineering, chemical engineering, chemistry, physics, and the biosciences. Our recent successes in analytical instrumentation reflect our broad, multidisciplinary base.

We continue to show a very high rate of return on investment with a total budget of roughly $17M, including $0.55M of Tech-Base projects. We have successfully performed collaborations with industry, and we have achieved considerable national recognition for the successes we have demonstrated in our Chem-Bio Nonproliferation (CBNP) Program instrumentation, supported by the DOE and the Defense Intelligence Agency. In April of 1999, we published a highlighted article in *Science* on the fastest poly-merase-chain-reaction (PCR) detection, starting with 1000 bacterial cells—seven minutes for automated detection. (The technology for this PCR instrument was invented under Engineering TechBase funds.)

The support for our work on detection instruments for the CBNP program has grown significantly for FY-00.

As the applications for microtechnology continue to grow, we continue to perform activities to fulfill the needs of our LLNL and external partners and stay in a leadership position, both nationally and world-wide.
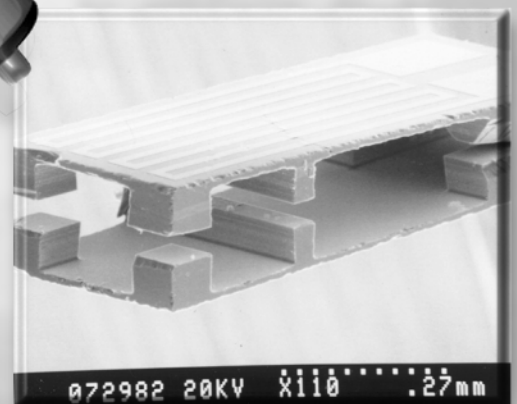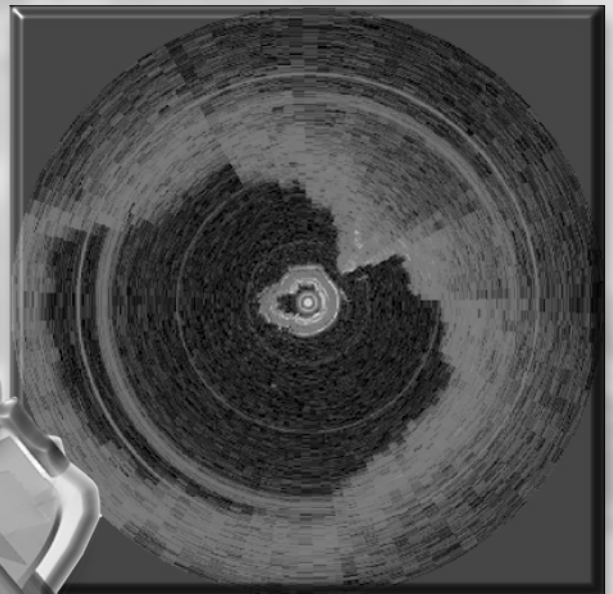
The small, previous TechBase investments in Microtechnology have paid off this year:
1) highlighted article in *Science* on the performance of the LLNL PCR instrument;
2) article in *Science* on Protein-DNA interactions in the flow cell built and operated by Microtechnology personnel;
3) laboratory success in DARPA-funded dielec-trophoresis technology for blood cells;
4) optical interconnects in partnership with the Photonics Program–significant demonstration of multiple-wavelengths carried per fiber;
5) a large CRADA with semiconductor houses for EUV lithography—we have expanded our facilities to accommodate this work, and the semiconductor industry has selected EUVL as the follow-on technology on their roadmap;
6) collaboration with UCLA on wireless sensors.

Articles in this report are: 1) Exploration of Novel Fabrication Methods for Microfuidics/Microelectromechanical Systems Devices; 2) Microtechnology for High-Explosive Testing; 3) Improved Microgripper Process; 4) Miniature Sample Collector/Concentrator for Biological Weapons Agent Detectors; 5) Microfabricated Deformable Mirrors for Adaptive Optics Applications; 6) High-Voltage Photovoltaics; 7) Microfabricated Flow Cell for DNA Analysis; 8) Microvalves for Microcatheters; 9) Microelectromechanical-Systems-Based Fuel Cell for Microscale Energy; 10) Custom Silicon Etching; 11) Micromechanical Characterization Tools for Highly-Filled Polymers; 12) Advanced Imaging Catheter; 13) Intelligent Wavefront Reconstructors for Adaptive Optics; 14) Lambda Connect: Multiwavelength Technologies for Ultrascale Computing; 15) Low Power Wireless Modem Technology; 16) Wireless Micropower RF Components; and 17) Acoustically-Driven Microfluidic Systems.

Center for Microtechnology

2

072982 20KV X110 .27mm

2. Center for Microtechnology

Exploration of Novel Fabrication Methods for Microfluidics/Microelectromechanical Systems Devices

Harold D. Ackler and Julie Hamilton
Electronics Engineering Technologies Division
Electronics Engineering

William J. Benett
New Technologies Engineering Division
Mechanical Engineering

Thomas E. Shell
Materials Science and Technology Division
Chemistry and Materials Science

We have developed a preliminary capability for fabricating microdevices from different glass and ceramic material systems. This project provided more flexible fabrication routes to expand the number of device designs accessible by the Center for Microtechnology staff and customers at Lawrence Livermore National Laboratory (LLNL).

Introduction

We investigated potential uses of commercial materials technologies, used in the fabrication of microelectronic packages and planar waveguides for photonic devices, for microfluidics and micro-electromechanical systems (MEMS) fabrication. General processes addressed include the fabrication of channels with or without electrodes and bonding the materials together. Materials to be studied are thick glass films and multilayers deposited on alumina substrates via dip-coating of glass slurries, which are then densified and channels etched therein, multilayer ceramics fabricated from ceramic tapes with channels and vias which may include screen-printed metal conductors, and the photostructurable glass Foturan™. The point is to explore how the selection of materials and sequencing of process steps may enable the fabrication of devices with as-yet unimagined functionality. Some materials may enable certain aspects of device packaging, for example fluidic and electronic interconnects, to be integrated into the device.

If LLNL's Center for Microtechnology were able to develop a suite of device fabrication methods that offered adequate flexibility to essentially make whatever an engineer wanted, then the initial emphasis in device and system development would shift from "what can we make?" to "what do we want?" By conducting this exploratory work with a team of materials researchers oriented to the needs of the Center for Microtechnology staff, not only may materials solutions to current limitations be discovered, but also new uses for "old" materials technology may arise.

Progress

Deliverables for this project included the following: (1) an evaluation of the viability of the above materials (microelectronic packaging materials, glasses other than Pyrex™) for microfluidic device fabrication; (2) process to fabricate multilayer ceramics, with channels and holes, from ceramic tapes; (3) process to bond the above materials. Measures of success: a new process that enables the fabrication of more functional devices, or current devices with reduced difficulty.

Dip-Coated Glass Films

Glass films have been deposited by dip-coating a glass slurry onto alumina substrates with patterned metal electrodes, then firing to densify the slurry coat. Channels were then etched into the glass film, their thickness determined by the film thickness as expected. The film thickness was only 5 μm for a single dip-coat. A means of producing thicker dip-coated glass layers on substrates was developed by patterning a thick layer of SU-8 photopatternable epoxy onto a substrate (patterned with metal) where channels are to be. The substrate is coated with an excess of glass slurry and the excess "squeegeed" off above the SU-8 features. The SU-8 thus acts like a mold, and is burned off during firing of the glass layer to leave the desired channels in the glass layer. However, more sophistication is required to produce glass films of very uniform thickness.

Photopatternable Metal and Dielectric Pastes

Photopatternable dielectric paste and gold paste (Fodel™ from DuPont) were screen printed and dried (by offsite vendor) on alumina substrates. Those coated with dielectric were prepatterned with metal electrodes. Pastes were photolithographically patterned and developed to form electrodes in the gold film, and channels in the dielectric film whose depth was determined by the dielectric layer thickness (25 μm) with the prepatterned electrodes in the channel bottom. The dielectric films were fired to densify the ceramic material. Screen printed, photopatternable conductor paste was successfully patterned and fired on commercial alumina substrates. The minimum resolvable feature size appears to be in the 30 to 50 μm range.

Green Tape

Channels and vias have been hand cut in ceramic green tapes. More precise features were formed by laser cutting green tape. Multilayer channel structures have been formed in laminated ceramic green tape and fired. Layers of tape have also been laminated to 0317 glass and fired. However, the moderate mismatch in thermal expansion (2 to 3 ppm/°C) is enough to cause deformation and/or cracking of the glass. A potential means of incorporating electrical connectors into a multilayer device formed from green tape has been designed. An initial attempt was made to fabricate such a structure, but deformation during firing of the multilayer tape structure rendered the part useless. The structure may be constrained during firing to prevent this, but it has not been tried.

Bonding

The bonding of Corning code 0317 glass to the commercial alumina substrates patterned with screen printed, photopatternable dielectric paste has been determined to be a nonviable process. While it is possible to achieve adherence of the glass to the dielectric layer, the moderate mismatch in thermal expansion (2 to 3 ppm/°C) between the glass and alumina substrate is enough to cause either spallation of the dielectric layer from the alumina or severe cracking of the glass. Substrates (glasses, ceramics) may be bonded at 600 to 650 °C if a thin layer of dip-coated glass (VIOX Corp. no. 12922) is between them. However, coefficient of thermal expansion mismatches must be very small. This process works very well for bonding code 0317 glass to Foturan™.

Smoothing Foturan™ Surfaces

A thin layer of dip-coated glass, when fired, was observed to smooth the roughness of etched Foturan™ significantly. However, the magnitude of the remaining roughness was not quantified.

Future Work

No actual devices were fabricated during this project. Many of these processes are well suited to the fabrication of microfluidic devices, so the next stage of this work is to develop the details of routes to fabricate working devices with these materials. ⬓

Microtechnology for High-Explosive Testing

Dino R. Ciarlo and Kirk P. Seward
Electronics Engineering Technologies Division
Electronics Engineering

Mehdi Balooch
Materials Science and Technology Division
Chemistry and Materials Science

Scott E. Groves
Manufacturing and Materials Engineering Division
Mechanical Engineering

We have used a high aspect ratio probe in an atomic force microscope to obtain images of the surface morphology of mock high explosives. This probe has a diameter of 0.2 μm and a length of 2 μm, which allows it to fit between the individual crystals of the material. In addition, a silicon force transducer for determining the viscoelastic properties of binder material has been built and tested.

Introduction

To better understand the material properties of composite materials it is necessary to measure the individual properties of the constituents as well as the adhesive forces between them. As an example, in the high-explosive (HE)—binder system, one would like to know the properties of the binder and the individual HE crystals as well as the adhesive forces between these two components. Groves *et al.*[1] discusses how this information can be used to develop models to predict the behavior and aging of such composites.

A relatively new technique uses atomic force microscopy (AFM) and nano-indentation to measure the modulus and the viscoelastic properties of a material on a microscale. Unfortunately most of the available probes for this work have large cone angles (60° to 90°), making it difficult to probe material that is thinly sandwiched between taller structures. In addition, the probes are designed to apply micronewtons (μN) of force instead of nanonewtons (nN). Microfabrication techniques can be used to provide these special probes and force transducers.

Progress

Plastic bonded explosives are composed of approximately 95% HE crystals and 5% binder. The crystal sizes tend to be in the 10- to 50-μm range and the space between crystals can be in the 2- to 5-μm range. To get a true representation of the surface morphology using an AFM, the probe must be capable of extending down in between the HE crystals. Standard AFM probes have very sharp tips, but they have large cone angles, as shown in **Fig. 1**. This prevents them from reaching down in between the HE crystals.

Recently, high aspect probes became available from Digital Instruments. They are called FISpike Probes and are fabricated using a focused ion beam to obtain the high aspect ratio. **Figure 2** is an SEM of one of these probes showing a shaft diameter of 0.2 μm and a length of 2 μm. We used this to probe the binder material in between the crystals in mock HE material (cyanuric acid). **Figures 3** and **4** show two images taken of this mock HE. The **Fig. 3** scan is with a standard AFM probe; **Fig. 4** is taken with the high aspect ratio probe, at a much higher resolution.

Ultimately the plan is to find an area of binder material between HE crystals and to measure the viscoelastic properties of this binder by recording the displacement versus time for a constant applied force. To do this, the force in the nN range needs to be measured and displacements of tenths of a micron need to be recorded. This is a challenge for most commercially available force transducers.

Figure 5 is a photograph of a silicon force transducer we built and tested. Four silicon cantilever beams hold the central 3-mm-×-3-mm silicon platform. Each beam is 500 μm wide, 3.4 mm long and 0.1 mm thick. The force versus distance for this transducer was measured using a differential variable-reluctance transducer (DVRT) made by MicroStrain. The results are
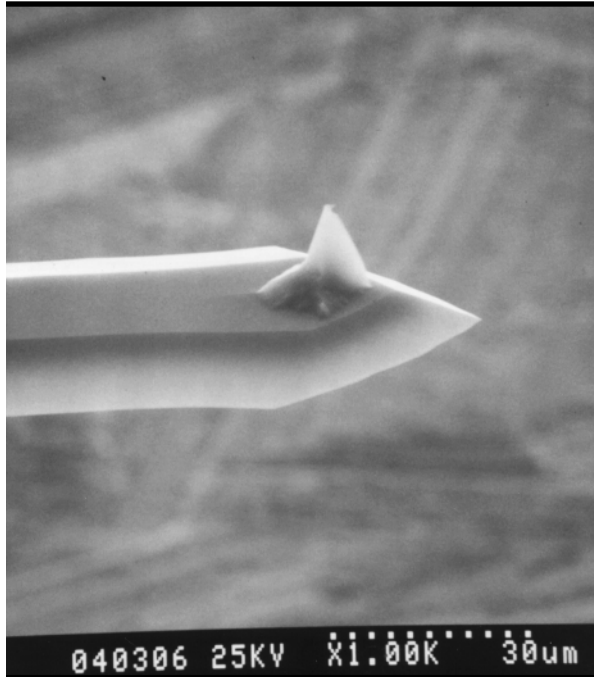
Figure 1. SEM of a standard AFM probe with a large cone angle.

Figure 2. SEM of a high aspect ratio AFM probe. The diameter of the probe is 0.2 μm and the length is 2 μm.

Figure 3. SEM scan of mock HE taken with the standard AFM probe shown in Fig. 1.

NanoScope	Tapping AFM
Scan size	13.45 μm
Setpoint	1.400 V
Scan rate	0.8846 Hz
Number of samples	256

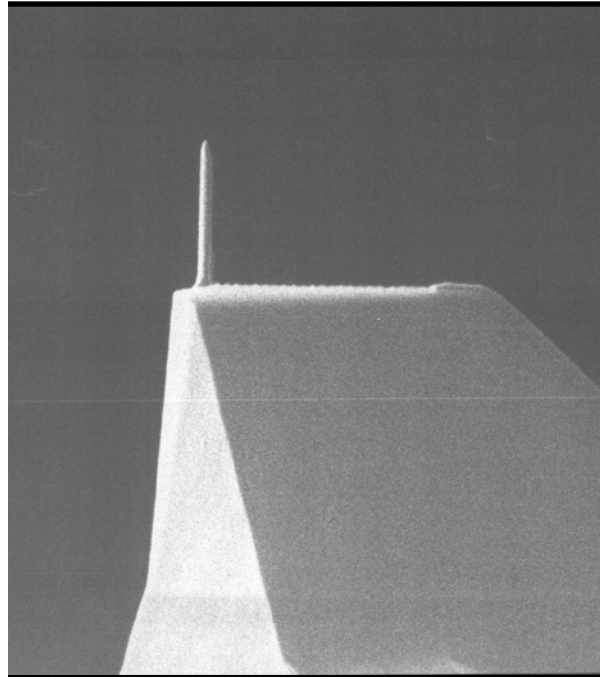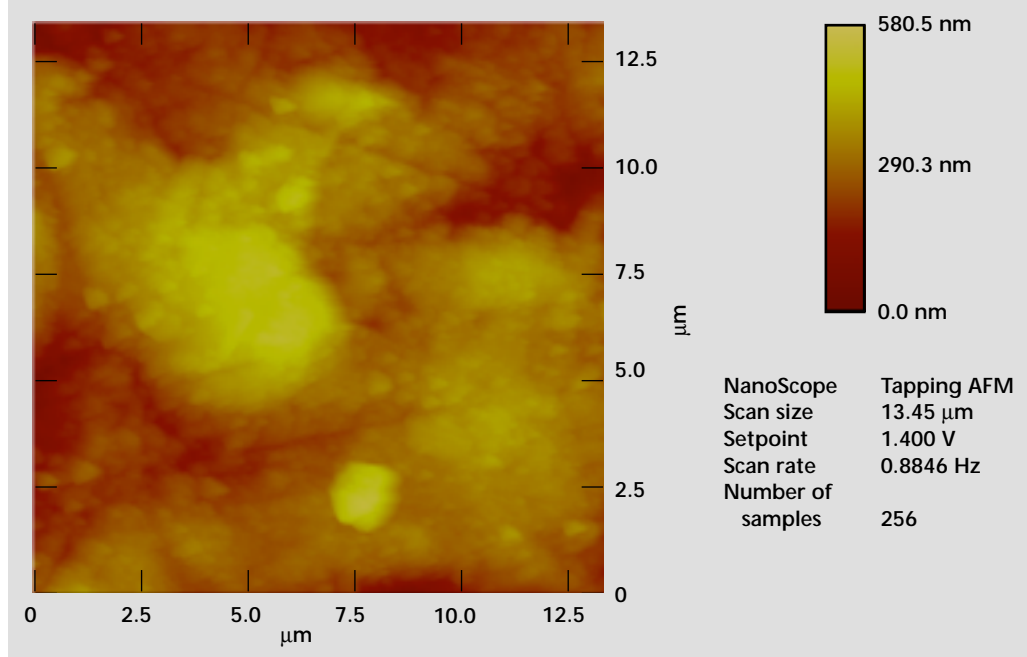shown in **Fig. 6**. The advantage of this type of silicon transducer is that the motion of the 3-mm-×-3-mm silicon plate is piston-like, without tilt. The motion of this plate can be measured by sensing the change in capacitance between the moving plate and a reference ground. The equation governing the deflection of the cantilevers is:

$$F = \frac{EB}{4}\left(\frac{H}{L}\right)^3 X, \tag{1}$$

where

F = force at the cantilever end (N)
X = cantilever deflection (mm)
E = silicon modulus (1.8×10^5 N/mm^2)
B = cantilever width (0.5 mm)
H = cantilever thickness (0.1 mm)
L = cantilever length (3.4 mm)

In **Eq. 1**, the spring constant for the force transducer can be considered to be:

$$\frac{EB}{4}\left(\frac{H}{L}\right)^3. \tag{2}$$

For the values listed, **Eq. 1** reduces to:

$$F = 0.6\ X. \tag{3}$$

Since there are four of these cantilevers supporting the central 3-mm plate, the relation between the force on this plate and its displacement is:

$$F_T = 2.4\ X. \tag{4}$$

The data taken in **Fig. 6** shows a spring constant of 1.4 as opposed to 2.4 in **Eq. 4**. The difference, less than a factor of two, can be accounted for by errors in the true dimensions of the fabricated transducer.

For the transducer design shown in **Fig. 5**, a force of 100 µN will cause a deflection of 71 nm. To get a nanometer deflection with a nanonewton force, the spring constant needs to be lowered by a factor of 100. This can be easily accomplished by halving the value of the thickness (H) and the width (B) and by lengthening the cantilevers by 50%.
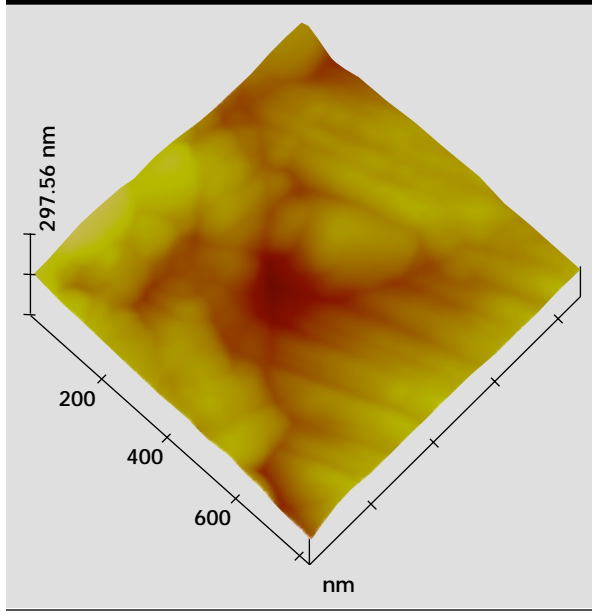

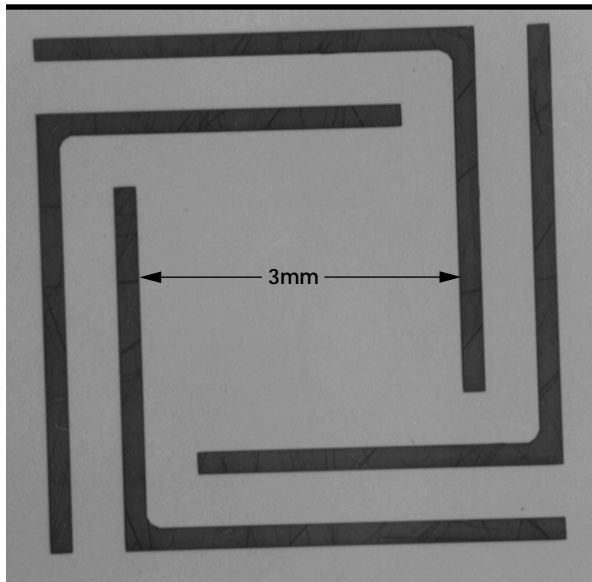Figure 4. SEM scan of mock HE taken with the high aspect ratio probe shown in Fig. 2.

Figure 5. Planar view of a silicon force transducer consisting of a 3-mm-×-3-mm silicon plate supported by four silicon cantilever beams.
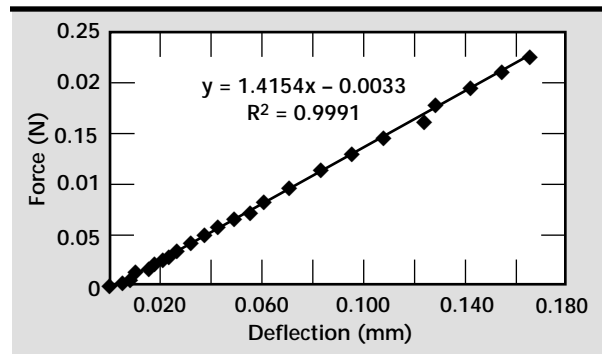
Figure 6. Force versus deflection measurements of the force transducer shown in Fig. 5.

Future Work

The next logical task is to build the nanonewton force transducer and combine it with the commercially available high aspect ratio probes. The viscoelastic properties of composite materials can then be measured.

Reference

1. S. Groves, S. DeTeresa, B. Cunningham, D. Ciarlo, D. Allen, K. Clayton, and C. Yoon (1999), "Micromechanical characterization tools for highly-filled polymers," *Engineering Research, Development and Technology*, Lawrence Livermore National Laboratory, Livermore, California (UCRL-53868-99).
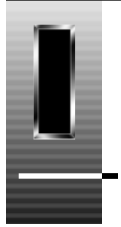
Improved Microgripper Process

Dino R. Ciarlo, Abraham P. Lee, Dawn L. Hilken, and Jimmy C. Trevino
Electronics Engineering Technologies Division
Electronic Engineering

A deep etch RIE silicon process has been used to simplify the fabrication of a silicon microgripper. The microgripper is 1 mm long, 0.2 mm wide and can grip objects as big as 110 μm with a force of 13 mN.

Introduction

Several years ago, a silicon-based microgripper[1] was developed at Lawrence Livermore National Laboratory (LLNL). This microgripper had many uses, including the delivery of coils for the treatment of aneurysms and the manipulation of very small parts. The overall size of the microgripper is 0.2 mm × 1.0 mm, with a gripper opening of 100 μm. The gripper action is actuated by shaped-memory-alloy (SMA) films, deposited on silicon cantilever beams. The original microgripper was fabricated using silicon etch-stop technology to define the thickness of the gripping cantilevers. This report describes a simplified microgripper fabrication process.

Progress

Following the installation of the STS deep silicon etcher in LLNL's Microfabrication Laboratory, it was evident that the fabrication of the Lee microgripper could be simplified. **Figure 1** is a cross-sectional view of the simplified fabrication procedure. The simplification comes in the step shown in **Fig. 1b** where the thickness of the gripping cantilever is defined by a controlled STS etch instead of the more complicated wet-etch-stop procedure. The etch rate for silicon using the STS etcher is 5 μm/min, so the cantilever thickness can be controlled by etching 100-μm-thick wafers for 18 min. Following the cantilever formation, the two halves of the microgripper are bonded together using a gold eutectic. The final microgrippers are then defined by a sawing operating which establishes the length and width of the microgripper. **Figure 2** shows three SEM views of an assembled microgripper.

a) Pattern a 100-μm-thick wafer with oxide.

b) Evaporate heater elements on one side.

c) Etch silicon with STS etcher to form 10-μm-thick cantilevers.

d) Evaporate gold eutectic for bonding.

e) Bond wafers together and saw to final size.
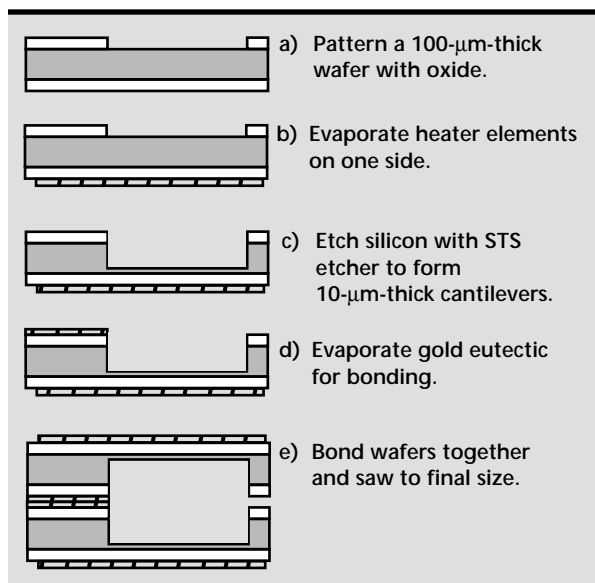
Figure 1. Cross-sectional view of the improved microgripper process.
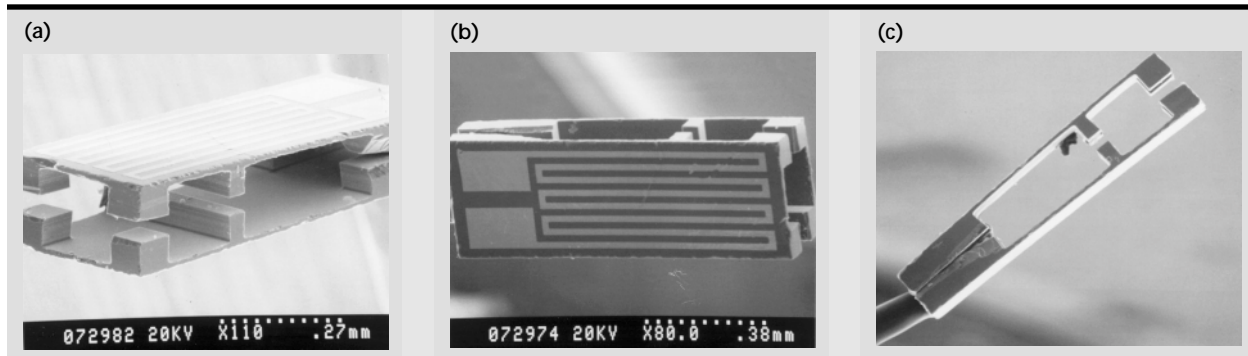
Figure 2. Three SEM views of a completed microgripper, 1 mm long by 0.2 mm wide. The serpentine gold pattern is used to heat the shaped memory alloy actuator.

Future Work

To save time, the above process did not include the SMA films, since the purpose was to demonstrate the timed etch in the STS deep etcher. To fabricate a fully-functional microgripper, this SMA actuator needed to be applied to the silicon cantilevers.

Reference

1. A. P. Lee, D. R. Ciarlo, P. A. Krulevitch, S. Lehew, J. Trevino, and A. M. Northrup (1996), "A practical microgripper by fine alignment, eutectic bonding and SMA actuation," *Sensors and Actuators A* **54**, pp. 755–759.

Miniature Sample Collector/Concentrator for Biological Weapons Agent Detectors

Jonathan Simon
Center for Microtechnology

Miniature aerosol samplers are desired by the nonproliferation community to detect the use of biological weapons consisting of aerosolized pathogens such as bacterial spores. A prototype miniature collector has been developed which decouples the sampling time from the final sample volume, allowing for greater concentration of trace pathogens. The device would be used at the front end of a portable biological weapons agent detection system.

Introduction

As the threat of biological weapons (BW) increases, both in military theaters and on civilian populations, the need for portable systems for the rapid analysis of pathogenic organisms becomes increasingly important. At the front of any system for the detection and characterization of biological agents is a sample collector. This can take the simple form of a swab for solid surfaces, or as in the case of airborne pathogens, an aerosol sample collector used to collect and concentrate particles into a liquid sample volume for subsequent analysis. An aerosol sampler is most appropriate for continuous monitoring scenarios, where repeated swabbing of settled particles is impractical.

The agents to be sampled are in the form of respirable particles with sizes in the range of 1 to 10 μm. Commercial sample collectors now available for field use are large, power-hungry, and typically produce sample volumes of many milliliters. Prototypical portable fieldable systems use assays that analyze much smaller sample volumes, typically <100 μL. Collector technology, however, has not entirely kept pace with this trend towards miniaturization, and present milliliter samples must be subsampled, reducing sensitivity, or preconcentrated, increasing complexity and the probability of breakdown.

Several commercial collectors use a thin film of liquid to capture target particles. Current designs generally have a lower limit to their sample collection volume because they send captured particles to a reservoir in a continuous stream. In the case of a low concentration sample, this leads to a large sample volume since the sampling time must increase to capture enough particles to be detected. Typical sample collectors provide for concentration factors of 104 to 106. That is, one particle per liter of air yields 103 particles per milliliter of solution, after a set time for collection. Subsampling for a miniature detector can reduce the number of organisms available for analysis by a factor of 10 or more.

Progress

During FY-99, we developed a prototype low power, miniature sample collector which concentrates the sample into a volume <100 μL. Its major advantages over existing samplers are: (1) decoupling of sample volume and sample time, making it very attractive for low (air) concentration samples; (2) miniature size and low weight, making it easily portable; (3) low power consumption, also adding to portability and ease of deployment; and (4) low noise operation. The prototype device is very quiet.

Our design (patent pending[1]) uses a two-step process to capture respirable particles in a way that decouples sample concentration from final sample volume. An illustration of the concept of the device is shown in **Fig. 1**. The heart of the system is the capillary surface, which consists of a cylinder of material with an array of vertical slits. These slits are connected to a supply reservoir, and fill with water by capillary action. This provides a wetted surface of prescribed volume which captures particles present in the air, and makes the sample volume independent of sample time.
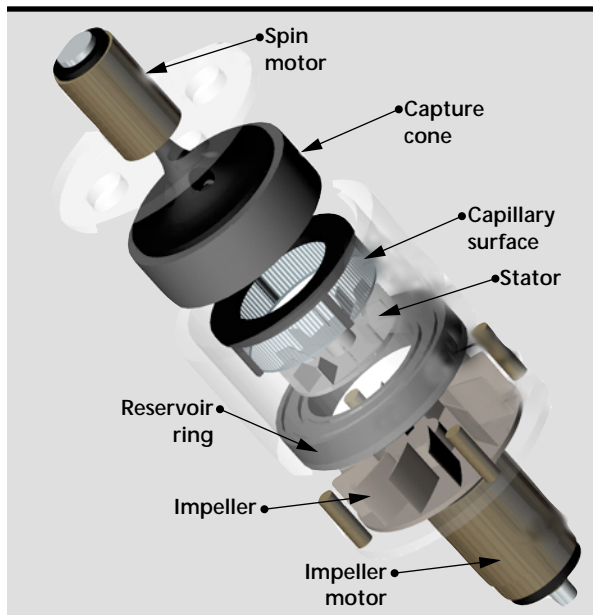
Figure 1. Illustration of the concept of the miniature aerosol sample collector.

Figure 2. Flow Cytometer scattering plot of sample, indicating 300,000 particles in sub-micron to several micron size range.

In the first step of operation (inspiration), which may last for several minutes, an impeller draws turbulent air (>200 L/min at 2 W of power consumption) through the device and over the capillary surface, collecting and concentrating particles present in the air. An optional stator turns the flow towards the surface to increase likelihood of capture at the expense of throughput. The capillary channels are connected to a central reservoir which also replenishes the capillary fluid as it evaporates. The channels arranged around the perimeter yield a total volume <100 μL with a wettable area of several cm^2.

In the second step (spin), the upper portion of the device consisting of the capillary surface and the capture cone is spun, and the sample volume is forced out of the capillary channels by centrifugal force. The liquid impinges on the non-wetting surface of the capture cone, and is deflected to the bottom of the device where it is finally collected in the capture portion of the reservoir ring.

In a short smoke test consisting of particles ranging from sub-micron to several microns in size, the device captured over 300,000 particles in a 50 μL volume (2×10^{11} particles/ft^3), demonstrating the working principle of the device **(Fig. 2)**. Further characterization with known aerosol concentration is needed to determine collector efficiency and concentration factors for longer sample times.
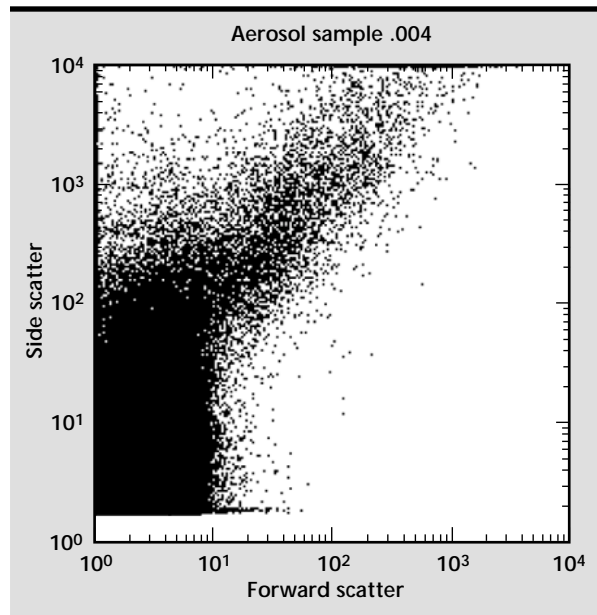
Future Work

The device and associated final sample volume are an order of magnitude smaller than existing collectors, providing for a truly portable, high quality aerosol sample collector.

Future works include iterative refinement of the device, supported by detailed experimental analysis and quantitative testing to measure capture efficiency and other flow properties. Integration of a separately developed microfabricated fractionator to removed particles outside of the target size range (1 to 10 μm) is also planned.

This sample collector could be used in a system both as a monitor, or in a response deployed situation. Any organizations responsible for BW incident response (National Guard, FBI, CDC, USAM-RIID) are potential customers, as well as the Chem-Bio Nonproliferation Program at DOE. While we are targeting the BW application, the collector could also be used for gathering forensic evidence, and as such it would be useful to the FBI and local law enforcement.

Reference

1. Lawrence Livermore National Laboratory, ROI IL-10401.

Microfabricated Deformable Mirrors for Adaptive Optics Applications

June Yu, James A. Folta, Peter Krulevitch, and Harold D. Ackler
Electronics Engineering Technologies Division
Electronics Engineering

Scot S. Olivier
Information Science and Technology
Laser Programs

William D. Cowan
Air Force Research Laboratory
Wright-Patterson Air Force Base

We have designed a high-stroke actuator suitable for adaptive optics (AO) applications. The advantage of this new actuator design are its simplicity of fabrication (only four lithography steps), and low susceptibility to lateral actuation forces which would cause contact and binding during displacement. Microelectromechanical systems-fabricated deformable mirrors based on this actuator will allow for broadband AO applications. Preliminary bonding experiments performed show great promise of the Au-to-Au compression technique for transferring mirror structures to foundry fabricated microactuator arrays.

Introduction

Adaptive optics (AO) technology is critical for many current and developing applications at Lawrence Livermore National Laboratory (LLNL). In particular, most large laser systems, including those being developed for inertial confinement fusion and laser isotope separation, require AO to correct for internal aberrations. In addition, AO can provide capability for both high-resolution imaging and beam propagation through the atmosphere. Requirements for laser systems, imaging, and propagation applications are currently driving wavefront control technology toward increased spatial and temporal frequency capacity, as well as reduced system costs.

Three classes of wavefront control devices can be considered for AO applications: standard deformable mirror (DM) technology using ceramic (for example, piezoelectric) actuators, liquid crystal (LC) spatial light modulators (SLMs), and microelectromechanical systems (MEMS) DMs.

Some disadvantages of standard DM technology are limitations on the number of controllable degrees of freedom, large separation between active elements, significant power requirements, weight, and expense. The large physical size of conventional DMs also leads to large optical components, making the entire AO system more cumbersome and costly. LC SLMs have the advantage of providing capability for high spatial frequency control applications. However, commercially available LC SLMs have the disadvantage of slow operating speeds, limited stroke, and low damage thresholds in comparison to conventional DMs.

The use of MEMS techniques to fabricate DMs for AO represents a nearly ideal match of technology and applications. These devices have the advantage of low power consumption, fast response, and high spatial density. Using MEMS fabrication techniques, the cost of DMs for AO can be reduced by a factor of 1000 from that of standard DM technology. Proper design and coating of the MEMS DM arrays will extend the operation of these devices to high average and peak power conditions. On-chip integration of electronic control circuits and batch fabrication will lead to reduced complexity and cost of AO systems. Taken together, the advantages of MEMS DM technology have the potential to revolutionize the field of AO.

For MEMS DM devices, several important technical issues must be resolved before they can be routinely used for wavefront control applications. Optical surface quality remains a principal challenge. Improvements of a factor of ~5 are needed over the current state of the art in the surface quality. Stroke (in and out of plane movement) is limited to ~1 μm for existing MEMS DMs. Scaling to large arrays also presents a technical challenge, mostly limited by the ability to address individual pixels.

In addition, further studies on high reflectivity, low-stress coatings for MEMS DMs and the optical damage characteristics of MEMS DMs remain to be carried out. Despite the unresolved issues, MEMS DMs offer tremendous potential for greatly expanding the use of AO in both laser and imaging system applications. It is our expectation that activities over the next few years will lay the technical groundwork for incorporation of these devices into laser and imaging systems.

Progress

In this first year, we accomplished the following:
1. Designed a high-stroke actuator. MEMS DMs based on this high-stroke actuator can offer vertical strokes up to tens of microns with kHz response time.
2. Identified a technical approach to improve the mirror surface quality and optical fill-factor of existing MEMS DM prototypes. Technologies developed will also be applied to the high stroke device.

High-Stroke Actuator Design

Existing MEMS DM designs suitable for AO applications are based on the parallel-plate electrostatic actuation principle. These devices have the advantage of low power dissipation, fast response time,
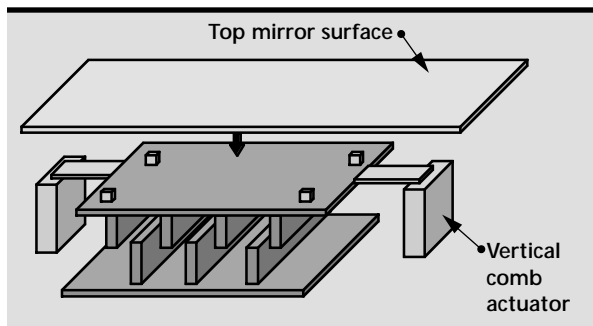

Figure 1. Conceptual picture of a vertical comb actuator. Details of our design are not shown here.

and compatibility with standard MEMS fabrication process. Actuation ranges of these devices are limited to ~1 μm with reasonable actuation voltages. These devices are therefore best suited for single wavelength or low-stroke AO applications. In some cases, a hybrid AO system architecture with a low-order standard DM coupled with a high spatial resolution MEMS DM could extend the dynamic range. Another approach to extend the dynamic range is to design MEMS DM devices based on a high-stroke actuator (greater than 4 μm).

We have analyzed a variety of actuation concepts to achieve high stroke. Actuator concepts analyzed included piezoelectric (bulk-, fiber-, and thin film-based), electromagnetic, and capacitive. We have selected a design based on the vertical comb capacitive actuator (**Fig. 1**) from among the various designs analyzed. Vertical comb actuators have the potential of allowing up to tens of microns stroke with very low power consumption.

Fabrication of these actuators has been made possible by the recent acquisition of an STS deep silicon etcher at LLNL. The simple four lithography step fabrication process we have developed for this design solves long-standing challenges in microfabrication and addresses deleterious lateral actuation forces. Mechanical and electrostatic calculations show large actuation can be achieved with reasonable voltage. **Figure 2a** shows the pull-in force as a function of voltage for a vertical comb with geometry shown in **Fig. 2b**. For 50 V, the force is approximately 0.01 μN/μm. To determine the total force, this number must be multiplied by the total length of drive fingers. For example, if there are ten 200-μm-long fingers, then the force is $(0.01)(10)(200) = 20$ μN. This is enough force to achieve a 4-μm stroke for our existing design. Further optimization of our suspension design will increase the stroke. For comparison, the gravitational force on a solid piece of silicon 50 μm × 50 μm × 5 μm is 0.3 nN. Risk reduction experiments addressing a potentially difficult Si-etching step in the STS etcher were successful.

Au-to-Au Compression Bonding of Mirror Membranes

The two most critical issues limiting the application of current prototype MEMS DMs are surface quality and the fill factor. There are currently no available devices that meet minimum requirements for LLNL AO applications. Even for the most advanced MEMS DM prototypes, significant

improvements are needed to make them useful for LLNL AO applications. Our goal is to accelerate MEMS DM development in collaboration with external groups to produce a working device for evaluation in the LLNL advanced AO test-bed. We have established collaboration with Major Cowan at the Air Force Research Laboratory at Wright-Patterson Air Force Base. The Cowan MEMS DMs are the most advanced in terms of quality, reliability, and availability.

We are improving MEMS DM surface quality by performing post-processing on Cowan devices by adding a final mirror surface to the foundry fabricated

Figure 2. (a) Pull-in force as a function of voltage for the vertical comb actuator shown in (b). (b) The geometry and pull-in force field line for the vertical comb actuator.

actuator array. **Figure 3** shows a 12-×-12 array Cowan microactuator with a 203-μm period. These actuators have up to 0.7 μm vertical stroke. The 90-μm circular post in the middle of each actuator is designed to accept the bonding of a continuous or pixilated mirror facesheet.

The technique we are using for bonding our mirror facesheet is an Au-to-Au compression bonding technique developed at BSAC for micro-component transfer processes. This bonding technique is superior to other micro-component transfer processes in a number of ways: (1) it is a room temperature process; (2) it does not require atomically clean or smooth interfaces; and (3) it does not require large bond bumps as does solder bump technology. This last advantage makes the technique suitable for fabrication of MEMS structures with small features. The ability to develop the technique with single die (chips) greatly reduces the cost and lowers the development risk by maximizing the number of experiments that can be performed at reasonable cost.

We have selected a multilayer stack to serve as our mirror facesheet. Experimental data show we can accurately tune the stress of this multilayer during and post deposition, thus allowing us to precisely control the mirror flatness. Since the mirror facesheet is fabricated in a separate process, what we do with them (such as high temperature anneal) will not affect the properties of the actuator and circuitry structures. Some of the fabrication challenges included electroplating uniform arrays of
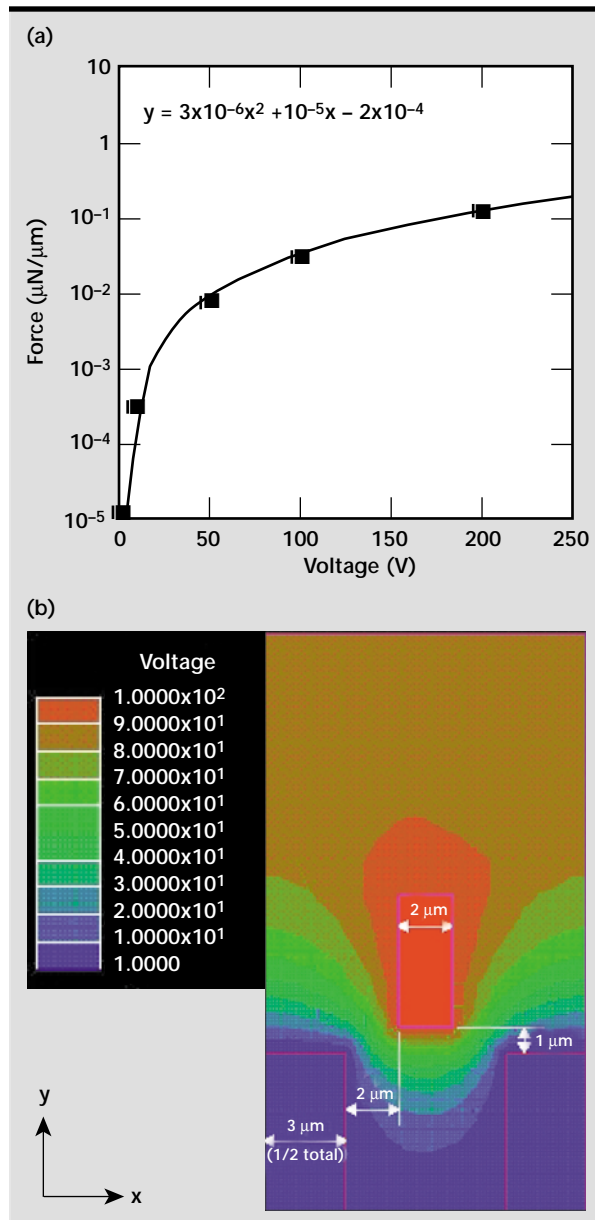

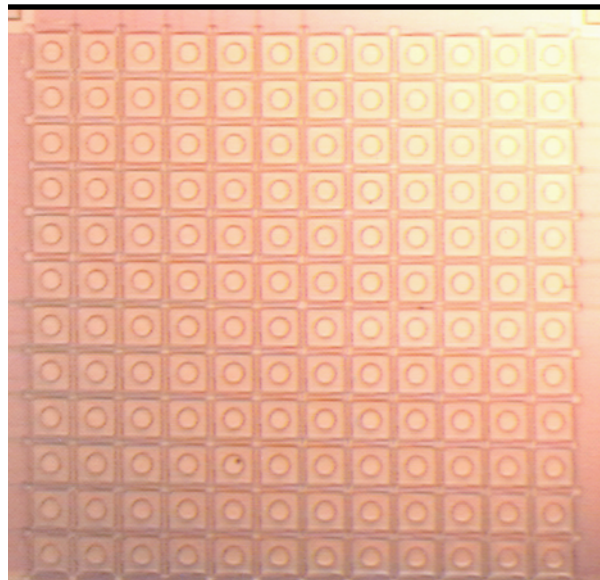*Figure 3. Photograph of a 12-×-12 Cowan microactuator array designed and fabricated for mirror facesheet bonding experiments.*

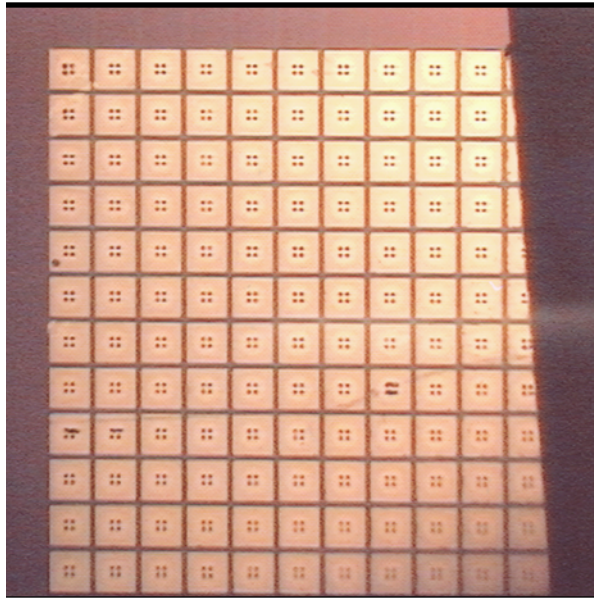Figure 4. Photograph of a 12-✕-12 array of 11-μm-tall electro-plated Au bumps sitting on a continuous mirror facesheet.

Figure 5. Photograph of a portion of a continuous multilayer facesheet that has been pixilated to a 12-✕-12-μm mirror array. A group of four 11-μm-tall Au bumps used to bond are located in the center of each mirror element.

high-aspect ratio Au bumps for bonding process. **Figure 4** shows a uniform array of 11-μm-tall Au bumps that were electroplated onto a continuous mirror facesheet.

In **Fig. 5**, the 1.38-μm mirror facesheet has been pixilated, resulting in a 12-✕-12 mirror array. The gap between each mirror element will be reduced in the future by using our high-resolution projection aligner to do the lithography. We have successfully bonded mirror facesheets to Au-coated Si wafers. The bond has greater than 9 MPa tensile strength (we have not tested the bond to failure) and endured greater than 6 h of hydrofluoric acid release bath without failure. We are currently working on the release process.

High-Voltage Photovoltaics

Jeffrey D. Morse and Gregory A. Cooper
Electronics Engineering Technologies Division
Electronics Engineering

Karla G. Hagans
Defense Sciences Engineering Division
Electronics Engineering

We have generated high-voltage power directly with an array of low-voltage photocells. The concept is to optically illuminate an array of photocells in parallel. While the low-voltage power generation of approximately 6 V has been previously demonstrated with commercial photocells using this approach, many program applications at Lawrence Livermore National Laboratory (LLNL) require the generation of significantly higher voltages (hundreds to thousands). Previous efforts have shown the generation of 1200 V using discrete arrays of GaAs diodes. A limitation in voltage scaleup and forming a compact, integrated photocell is excessive leakage current due to parasitic electric fields as arrays of series diodes are placed in parallel to minimize footprint. The result is a collapse of the voltage across each component of the array, thereby degrading the overall voltage generated by the entire photocell. To demonstrate an integrated photocell array, we are developing a current isolating buffer layer integrated with the diode array.

Introduction

High-voltage photovoltaic arrays are being developed as a means to provide power via fiber optics for a variety of applications. **Figure 1** shows an example of high-voltage arrays which have been previously fabricated and tested. The limitation has been a collapse of the voltage across each component of the array, thereby degrading the overall voltage generated by the entire photocell. This collapse is believed to be due to excess leakage current being generated between the rows of the diode array having opposite polarity as the rows are placed in parallel (**Fig. 2a**), which results in a maximum voltage difference of 180 V at the unconnected ends of adjacent diode array rows (1 V/diode × 90 diodes/row = 90 V differential/row).

Thus, with a distance of 300 μm between adjacent rows, the field strength between certain portions of each row is high enough to inject current into the substrate, resulting in a leakage
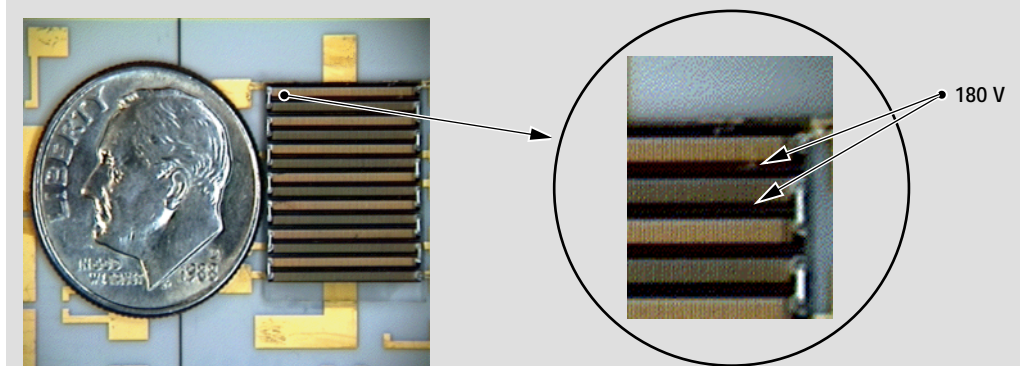

180 V

Figure 1. Photocell. High-voltage array developed to provide power via fiber optics.

current path between adjacent rows. The problem can be solved by physically separating adjacent rows and connecting the leads at each end by a wire, thus isolating the substrates electrically, as illustrated in **Fig. 2b**. However, this approach is not consistent with increasing the overall voltage of the array and reducing the footprint. An array having current isolating buffer layers between the diode structures and the substrate provides an integrated solution to the problem.

Progress

To reduce or eliminate the leakage current between adjacent rows, a current isolating buffer layer is required. Since the photocell array is fabricated using the gallium arsenide (GaAs)
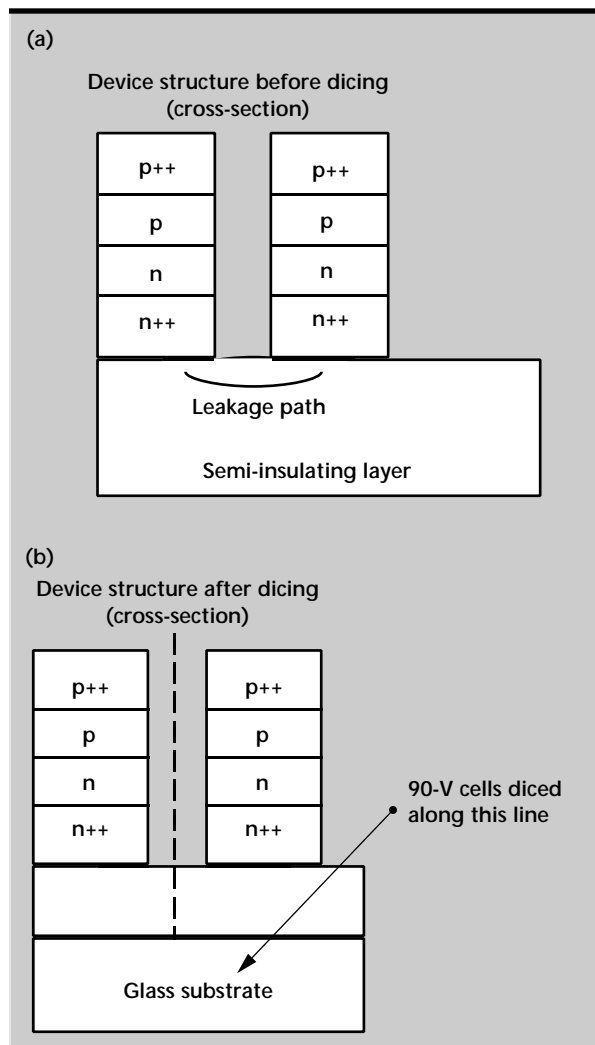
materials system grown by metallorganic chemical vapor deposition (MOCVD), the natural approach to reduce substrate leakage current is to incorporate a layer between the substrate and diode structure which acts as a barrier to current flow. For this work, the growth of aluminum arsenide (AlAs) epitaxial layers on the substrate provides an offset in the conduction and valence bands at the GaAs-AlAs interface, as illustrated in **Fig. 3a**. As the voltage across the structure increases, causing the bands to bend, the path of flow of electrons is impeded by this band offset, until the effective distance across the barrier becomes small enough such that the electrons can tunnel through the barrier (**Fig. 3b**), at which point the current has an exponential dependence on voltage. Intuitively, the thicker the barrier layer, the higher the voltage at which the electrons begin to conduct current.

Test structures were grown on semi-insulating GaAs substrates by MOCVD. An AlAs film was grown first, varying in thickness from 200 Å to 2 μm, followed by 5000 Å N+ GaAs to provide an electrical contact.

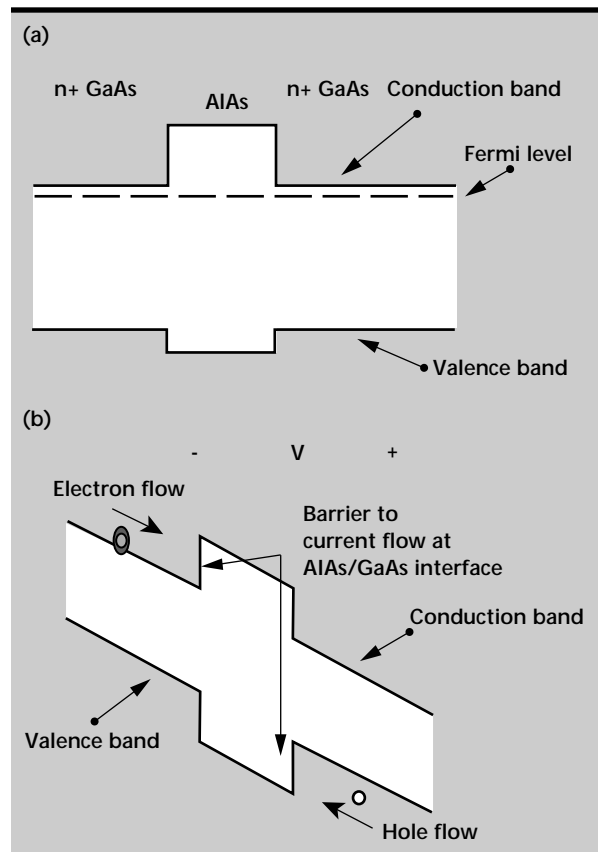Figure 2. Device structure before (a) and after (b) dicing.

Figure 3. (a) Illustration of band diagram for N = GaAs/AlAs/n + GaAs structure at equilibrium.
(b) Band diagrams with applied voltages showing barriers to current flow at AlAs/GaAs interface.
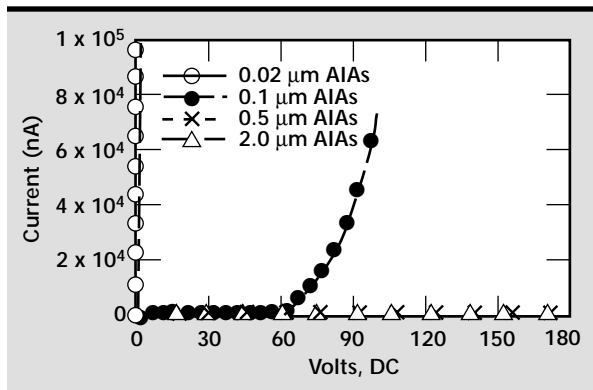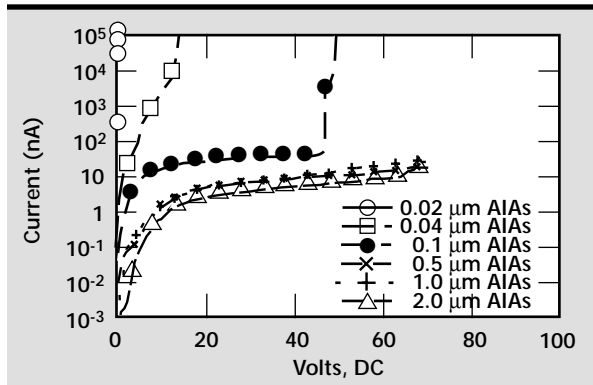
Figure 4. Leakage currents for 200-μm electrode spacing.

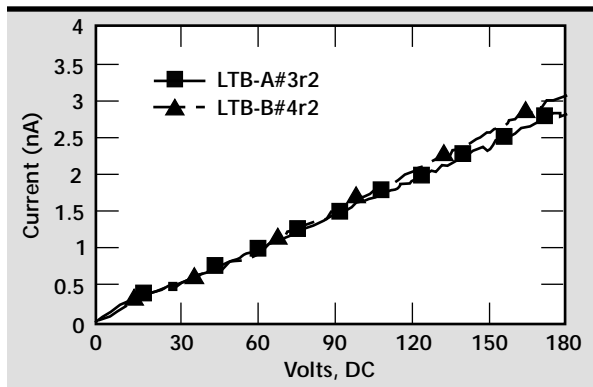

Figure 5. Leakage currents for 20-μm electrode spacing.

Figure 6. Leakage currents for 1-μm-thick low-temperature buffer.

Test devices were fabricated by forming a mesa ridge structure on which a contact metal pad was patterned. The current vs. voltage characteristics were then measured as a function of distance between the electrodes. These results are shown in **Fig. 4**.

From the data, it can be seen that the voltage or electric field at which the current begins to conduct significantly increases as a function of AlAs layer thickness. A similar comparison presented on a log-I plot (**Fig. 5**) shows the leakage current is reduced by 3 to 5 orders of magnitude as the buffer layer thickness increases.

Additional buffer layers based on the low temperature growth of GaAs (LTB-GaAs) by molecular beam epitaxy (MBE) was investigated. The LTB-GaAs has the property that the crystal lattice of the MBE layer has a significant level of naturally occurring defects which act to trap any charge which is injected into it, yet retains adequate crystalline properties such that high quality layers can be grown on top of it. Similar structures were fabricated in 1-μm-thick LTB-GaAs layers. The resulting current/voltage characteristics are shown in **Fig. 6** where a current of only a few nanoamps is exhibited at 200-V bias, thus the current is essentially eliminated.

Future Work

We are proceeding to the fabrication and testing of the entire high-voltage photovoltaic array with integrated buffer layers as discussed above. Both AlAs and LTB-GaAs layers are being investigated, and will likely provide an integrated solution to next generation high-voltage photocells for applications at LLNL.

Microfabricated Flow Cell for DNA Analysis

Peter Krulevitch and Laurence R. Brewer
Electronics Engineering Technologies Division
Electronics Engineering

We have microfabricated a flow cell for investigating the interaction of various proteins with DNA molecules. The cell proved to be superior to previous designs, with improved optical clarity and low background fluorescence.

Introduction

We have microfabricated a flow cell for investigating the interaction of various proteins with DNA molecules. The objective was to produce a flow cell with microchannels such that two fluid streams could be made to converge under laminar flow conditions, with mixing occurring only by diffusion across the interface between the two fluids. The top surface of the cell was required to be thin (0.007 in.) to enable visualization within the channel using a confocal microscope. An additional specification called for the cell to be made of a material with low background fluorescence. The challenge was to devise a fabrication scheme that did not introduce a fluorescing or optically-diffusing layer in the illumination or viewing path.

Progress

A new process was developed to fabricate flow cells having high optical clarity, with the channels formed in such a way as to produce a smooth surface which does not scatter the illuminating laser beam. The original plan was to investigate quartz as a material for the flow cell. However, Lawrence Livermore National Laboratory has considerable expertise in etching smooth microchannels in borosilicate glass substrates (20 to 40 nm roughness for 20-µm-deep channels), and the glass was found to have low autofluorescence at the desired wavelength.

Figure 1 illustrates the fabrication process. Twenty-micron-deep flow channels were photolithographically patterned in 1.1-mm-thick borosilicate glass substrates. Holes were wet-etched through 0.007-in. cover slips for fluid ports. These two substrates were placed in contact, and a low viscosity UV-curable epoxy was introduced along the edge. The epoxy wicked in between the substrates under capillary forces, but stopped at a moat that surrounded the flow channels. Using this approach, no epoxy layer was present in the optical pathway. The sandwich was then exposed to UV radiation to cure the epoxy. Finally, HPLC tubing connectors were bonded to the fluid ports using Ablestick sheet adhesive.

The flow cell was connected to a syringe pump and tested under pressure, and no leakage was observed. The cell proved to be superior to previous designs, with improved optical clarity and low background fluorescence.

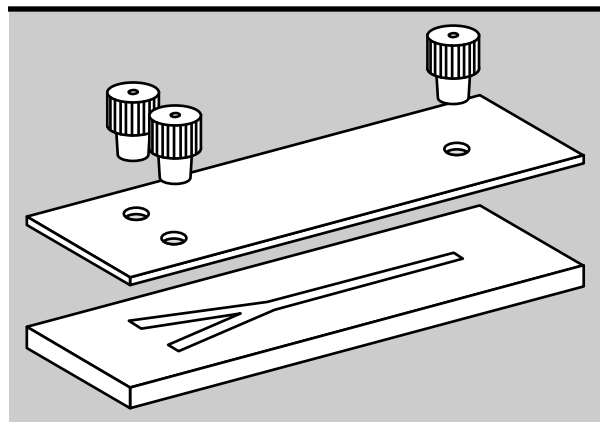High-resolution images of DNA condensing with this flow cell were recorded.

Figure 1. DNA flow cell fabrication process.

Microvalves for Microcatheters

Kirk P. Seward
New Technologies Engineering Division
Mechanical Engineering

Amy W. Wang and Abraham P. Lee
Electronics Engineering Technologies Division
Electronics Engineering

We have invented and are developing microvalves compatible with microcatheters for interventional neuroradiology applications. The main goal was to control the flow rate of fluid injection into the brain arteries with inner diameters as small as 1 mm. The applications are for the deposition of therapeutic material to close off arteriovenous malformations (AVMs) or for localized drug delivery. This technology is aligned with core competencies in microfluidics and advanced packaging at Lawrence Livermore National Laboratory (LLNL)'s Microtechnology Center (MTC). The project has also supported LLNL's Medical Technology Program (MTP).

Introduction

Beginning in 1995, LLNL began to focus on stroke as an area where its expertise in lasers, optics, computer modeling, and micromechanical systems could be used to develop treatments where few options were available. The MTC and MTP have invented several microtools that fit through microcatheters (0.5-mm inner diameter) including microgrippers, microcauterizers, micro-biopsy devices and microsensors.

A mechanical release mechanism to deposit coils into brain aneurysms resulted in a major cooperative research and development agreement (CRADA) and to date the animal tests have been 100% successful.

Microfluidics has also been a core competency at LLNL. Several microvalves have been developed over the last five years. The integration of microvalves onto microcatheters would be a natural evolution of this technology. A manager at Boston Scientific made the request to implement a microvalve at the tip of their microcatheters for depositing therapeutic fluids into brain AVMs. Current methods use an external shut-off valve that leaves undesirable residual traces. As we develop a proof-of-concept prototype, a collaborative effort is likely.

Another application of microvalves on microcatheters is to position and steer the distal tip of microcatheters within the blood vessels.

Progress

Several design options were considered for a microvalve to attach to the distal tip of a microcatheter. One of the designs that was tested was a one-shot valve consisting of a shape memory polymer (SMP) tube that is initially set to a closed position by heating it above its glass transition temperature T_g, crimping it shut, and allowing it to cool and form to the closed shape. Actuation of this tube is accomplished by optically heating the pigment-dyed polymer with a laser via an optical fiber. A SMP tube with 460-μm outer diameter and 50-μm wall thickness was extruded and tested to determine the opening force against a spring-loaded transducer. Tests confirmed the validity of a SMP microtube valve as the tube produced ~20 mN of radial opening force from a fully closed loading condition. After opening and allowing the tube to cool below its glass transition temperature, it could withstand >160 mN of radial force before crushing to half of its original diameter. The behavior of these tubes is illustrated in **Fig. 1**, and the data from the experiments is displayed in **Fig. 2**.
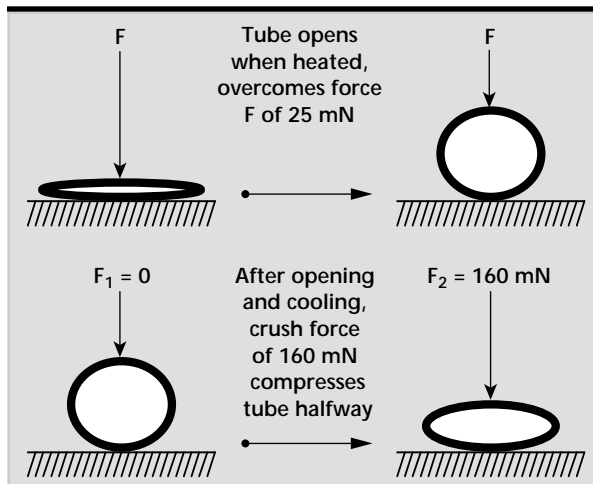
Figure 1. Behavior of SMP tubes during loading and heating (tube diameter = 460 μm, wall thickness = 50 μm).
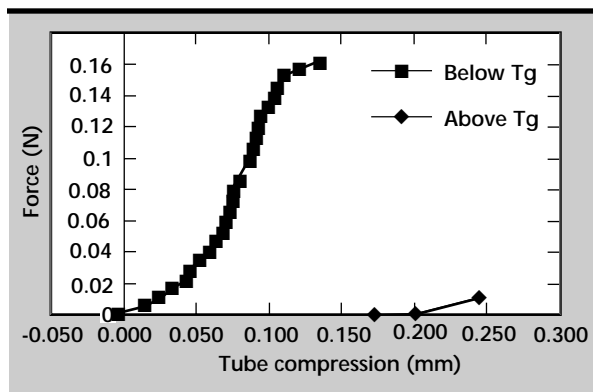

Figure 2. Experimental data, illustrating increased stiffness in tube below glass transition temperature, and 18 mN of force produced by the tube at full compression above the glass transition temperature.

A second valve design using molded SMP was also investigated. This design draws from typical micromachining capabilities to create mold cavities in silicon and glass wafers and then to use these molds, male and female, to create intricate polymer shapes with high repeatability and extremely tight tolerance. The valve, illustrated by the axial cross-section seen in **Fig. 3**, looks much like a micro-sombrero with the top of the hat cut off to allow fluid flow. It has therefore been dubbed the "sombrero-valve."

The valve is operated by optical heating and fluidic pressure changes. While at ambient temperature, the valve has 200× the stiffness as when it is heated above the glass transition temperature by the optical fiber laser. Fluid flow is therefore not inhibited because the valve retains its stiffness. Upon heating, however, a high enough pressure difference across the orifice of the valve will close or open it, depending on the direction of the pressure drop. This
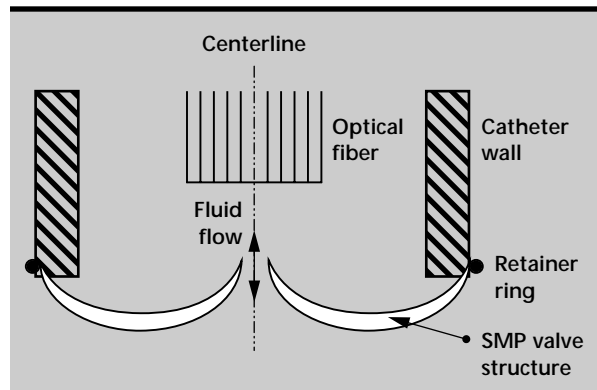

Figure 3. Cross-sectional view of sombrero valve attached to the distal end of a catheter. The diameter of the entire structure is <1 mm.

design for a bistable valve that can be used to precisely control the flow of fluids through the distal end of a microcatheter has not yet reached proof-of-concept, but the molds are nearly completed, at which time the valves can be created and tested.

Summary

Through our effort on this project, we have met the following milestones:

1. Two new bio-compatible microvalve technologies have been conceived that use the properties of SMPs to create molded or extruded valves to be fit onto catheter tips. The extruded valves have been reduced to proof-of-concept, while the molded valves are being processed.
2. One record of invention (IL-10569) has been filed for the sombrero valve and a second record of invention is being written for the one-shot tube valve.
3. An NIH proposal has been submitted with the collaboration of SUNY-Buffalo to design additional SMP BioMEMS devices for catheter-based surgery.
4. Processing knowledge to extrude and mold SMP and to create silicon and glass "micromolds" was gained and mold cavities are near completion.

We are currently taking steps to develop proof-of-concept devices so that patents can be more avidly pursued and collaborations can be realized with medical device companies.

Acknowledgments

Microelectromechanical-System-Based Fuel Cell for Microscale Energy

Jeffrey D. Morse
Electronics Engineering Technologies Division
Electronics Engineering

Alan F. Jankowski
Materials Science and Technology Division
Chemistry and Materials Science

We have investigated a novel approach to a miniature fuel cell power source by combining thin-film solid-oxide or proton-exchange-membrane electrolyte-electrode materials with microelectromechanical system (MEMS) techniques to integrate a fuel-cell stack monolithically on a manifolded host structure. This will enable a scalable, portable fuel cell power source system for a broad range of applications having requirements in the <1 W to >10 W regime. The MEMS approach offers a direct means to integrate the fuel cell stack with required manifolding and fuel delivery system, while providing the means to control the performance of the power source for specific applications. Results describing our progress in the fabrication, integration, and testing of MEMS-based fuel cells are presented below.

Introduction

Miniature fuel cells are receiving renewed interest for applications in portable power generation. Fuel cells store energy as fuel rather than as an integrated part of the system, which is the case with batteries. Therefore, fuel cells can potentially exhibit significantly higher energy densities in comparison to other energy storage devices.

While this power source has been demonstrated in bulk for higher power portable applications (50 to 500 W), effective scaling of fuel cell systems has not been demonstrated for low-power applications (<1 to 20 W). Present applications in portable power include the full range of consumer electronics, such as cell phones, laptop computers, video camcorders, and radios. New applications in portable power span the range of power consumption from micro, as in long duration sensors and remote communication devices, to macro, as in light-weight packages for use in the field.

Present requirements for autonomous remote sensors and communications devices for the intelligence community and the military are for power sources having extremely long shelf life and operating times, which are not presently available from battery technologies. The demonstration of a novel, high-performance power source will provide a mission-enabling technology that will expand the range of applications for electronic sensors and communication devices in intelligence gathering, military, and commercial applications. Furthermore, demonstration of the viability of this technology will accelerate the prototype system development time cycle, thereby expediting the deployment for realistic applications.

Progress

Technical Concept

The MEMS-based fuel cell is conceptually illustrated in **Fig. 1**, with an expanded detailed schematic
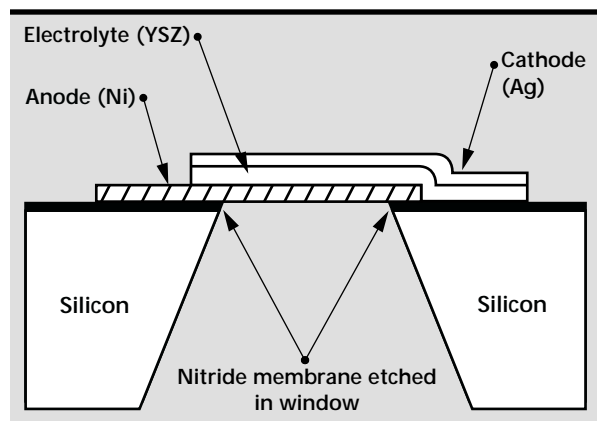

Figure 1. Schematic illustration of MEMS-based fuel cell concept.

of the thin film assembly approach in **Fig. 2**. This approach represents a completely new method for fuel-cell technology, potentially circumventing several problems traditionally associated with fuel cells, while further opening up a new range of applications for fuel cells as portable power sources. The MEMS-based fuel cell offers advantages in terms of manufacturability, fuel flexibility, reduced temperature of operation, and higher specific energy in comparison to other fuel-cell and battery technologies.

A further advantage of a thin modular design is the direct stacking of individual fuel cell modules, as shown in **Fig. 3**, enabling applicability to a wide range of power requirements.

The impact of the proposed effort is that a new, miniature power source will be established which provides an alternative to battery technologies, providing lighter weight, longer life, and potentially lower cost of portable power. This provides new functionality for use of sensor systems under development at Lawrence Livermore National Laboratory (LLNL) and the military for autonomous and manual use in the field. This technology will ultimately find its way into the commercial sector for portable electronics, and will open new markets for US manufacturers.

Experimental Results

Our efforts during the past year[1–5] were to determine the viability of thin-film MEMS-based fuel-cell technologies. These efforts have demonstrated the fabrication and initial operation of both solid-oxide and proton-exchange-membrane (PEM) electrolytes in fuel cells, monolithically integrated on silicon chips having micromachined manifold systems.

In developing the fabrication process we have addressed several issues associated with the integration and performance of a fuel-cell stack, micromachined fuel manifold, and flow field structure. This was accomplished by creating a thin-film porous-anode structure using photolithographic and etching techniques, combined with micromachining of silicon to form a free-standing fuel-cell membrane.

Photographs of these structures are shown in **Figs. 4** and **5**. Similar structures have been formed in the cathode layer by a comparable method. This allows the rapid diffusion of fuel and oxidant through the electrode structures to the electrolyte interface, as well as the exhaust of reaction byproducts (water).

A test fixture, illustrated in **Fig. 6**, was constructed to enable manifolding of fuel and oxygen to the anode and cathode respectively while the entire assembly was positioned in a furnace. Thus, the fuel-cell structure on the micromachined silicon chip was mechanically stabilized as the temperature was increased.

The fuel cell performance was measured by sweeping the voltage applied across the electrodes and measuring the current drawn from the power supply. The current-voltage characteristics for both
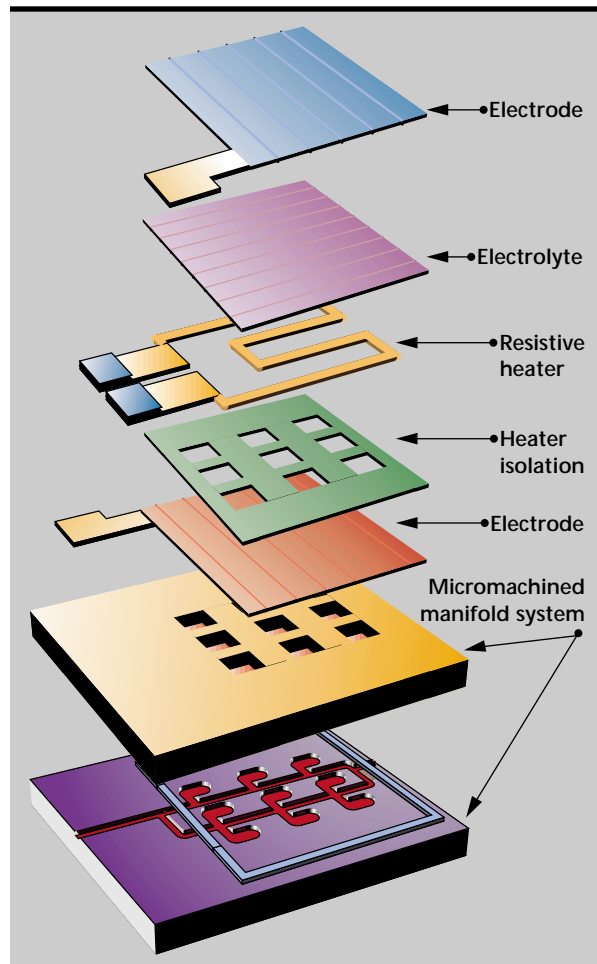

Figure 2. Schematic illustration of MEMS-based fuel cell thin film assembly.
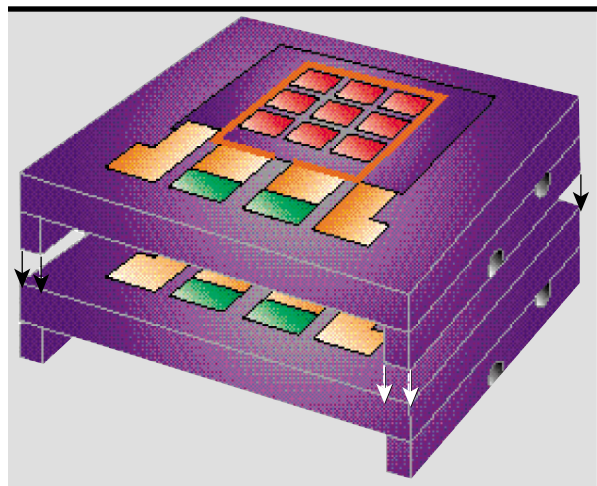

Figure 3. Power scaling by stacking of fuel cell modules.

the PEM and solid-oxide fuel cells (SOFC) at various temperatures of operation are shown in **Figs. 7** and **8**, respectively. From a technical standpoint, there are several key points to be drawn from these data. First, the PEM thin-film fuel cell operates over the temperature range from 50 to 90 °C, with a cell overpotential exhibited at room temperature. The fuel used for these tests was dilute hydrogen (4%) in argon, for safety reasons. For the PEM device, steam was added to the fuel feed, since the electrolytes require water to be retained in the membrane for adequate proton conduction.

Perhaps more compelling is operation of the solid-oxide thin film fuel cell over the temperature range 250 to 320 °C. The SOFC used a porous nickel anode, yttria-stabilized-zirconia electrolyte, with a silver cathode, all deposited using vacuum sputter-deposition techniques. The free standing SOFC membrane was tested using dilute (4%) hydrogen fuel, with the resulting current voltage characteristics plotted in **Fig. 8**. This is the lowest temperature of operation reported to date for a SOFC, the advantage offered by using thin-film components for the electrode and electrolyte.
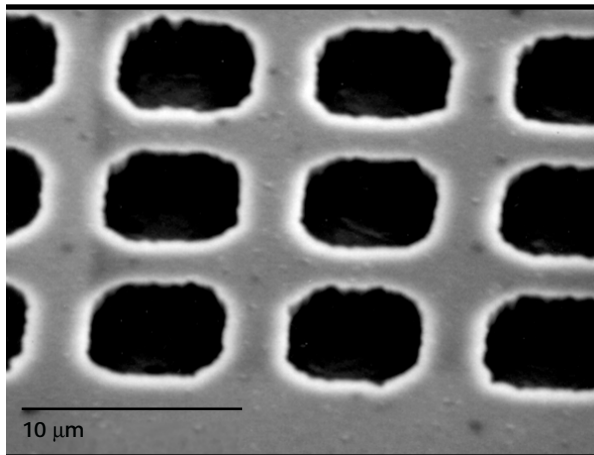

Figure 4. Top view of 0.5-μm thick Ni anode layer, imaged using scanning electron microscopy at higher magnification.
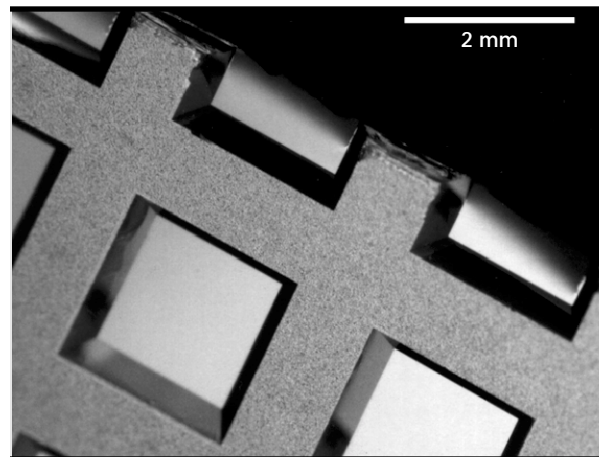

Figure 5. Bottom view of Ni anode layer deposited on the substrate platform, imaged using scanning electron microscopy.
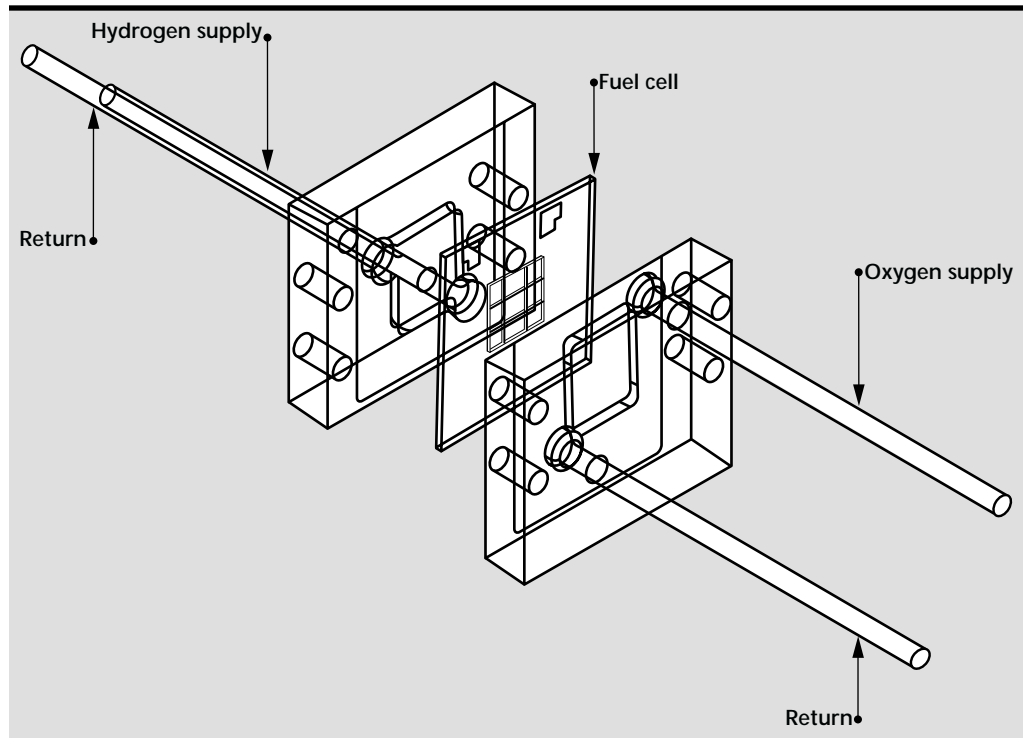

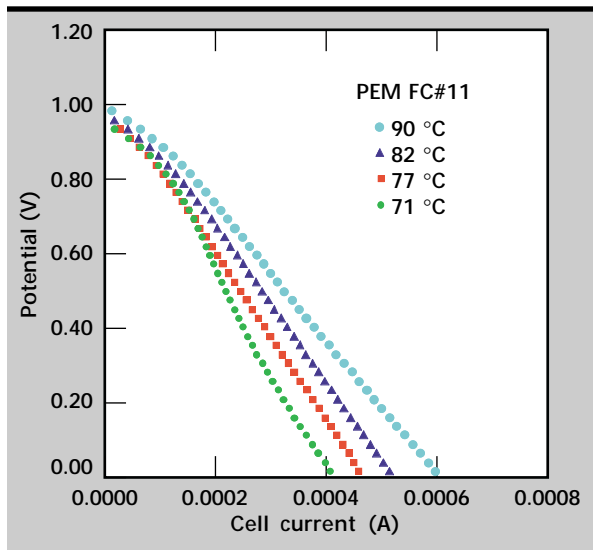*Figure 6. Schematic illustration of test fixture design.*

Figure 7. Current-voltage characteristics of MEMS-based PEM fuel cell (Pt/NafionTM) with 4% dilute hydrogen fuel.
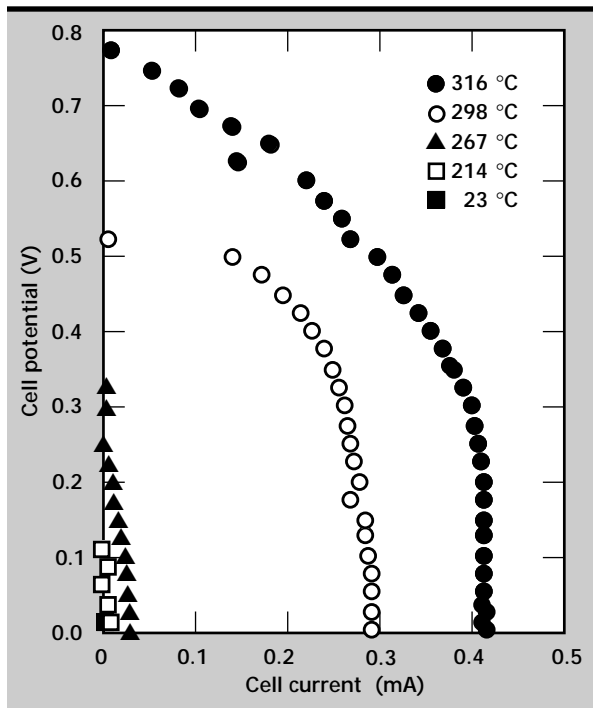

Figure 8. Current-voltage characteristics of MEMS-based solid oxide (Ni/YSZ/Ag) fuel cell with 4% dilute hydrogen fuel.

Future Work

Our efforts continue to optimize the process integration of the electrode/electrolyte material and structure for both the PEM and SOFCs. We are testing at fully-concentrated hydrogen fuel, and developing a computational modeling capability that will enable optimal design and thermal isolation approaches for the fuel cell. This is of particular importance now having demonstrated the operation of SOFC technology in the 250 to 320 °C range, which is thermally compatible with a wider range of materials for packaging, wafer bonding, stacking, and fuel delivery and control. We will begin the design and test of integrated resistive heaters based on the thermal modeling results. The primary focus, entering FY00, will be the integration, packaging, and stacking of several fuel-cell modules to demonstrate a power source at nominal voltage and current output of 3 V and 300 mA. Additional investigations will look at the use of hydrocarbon fuel and the fuel-cell design optimized for overall power efficiency.

References

1. J. D. Morse, R. T. Graff, J. P. Hayes, and A. F. Jankowski (1999), "Porous thin-film anode materials for solid-oxide fuel cells," submitted to *Mat. Res. Soc. Symp. Proc.* **575**, April.

2. A. F. Jankowski and J. D. Morse, "A MEMS-based thin film fuel cell," patent pending.

3. A. F. Jankowski and J. D. Morse (1998), "Thin film synthesis of novel electrode materials for solid oxide fuel cells," *Mat. Res. Soc. Proc.* **496**, 155–158.

4. J. D. Morse, A. F. Jankowski, J. P. Hayes, and R. T. Graff (1999), "A novel thin-film solid-oxide fuel cell for microscale energy conversion," submitted to ASME Symp. on Microscale Energy Conversion, November.

5. A. F. Jankowski, R. T. Graff, J. P. Hayes, and J. D. Morse (1999), "Testing of thin-film SOFCs for micro to macro power generation," accepted for publication in *Electrochem. Soc. Proc.*, SOFC-VI, October.

Custom Silicon Etching

Jeffrey D. Morse and Leslie M. Jones
Electronics Engineering Technologies Division
Electronics Engineering

Robert T. Graff
New Technologies Engineering Division
Mechanical Engineering

We have developed new, customized silicon etch processes to fabricate deep, anisotropic microstructures in support of present and future microelectromechanical systems (MEMS) projects at Lawrence Livermore National Laboratory (LLNL). The processes were established in the STS Plasma Etch system which uses sequential etch and passivation steps to achieve high etch rates for silicon, selectivity in etching silicon over silicon dioxide or photoresist masking materials, and highly anisotropic, high-aspect-ratio features.

Introduction

Present MEMS projects at LLNL require the capability to etch high-aspect-ratio, anisotropic structures in bulk silicon, which is critical for continued development of silicon MEMS-based technologies. This need has been addressed with the acquisition of an STS Plasma Etch system. While the system has validated processes for a specified set of structures and mask selectivities, we expect requests for numerous custom designs. Each design will require time and effort to optimize the process to achieve the desired results. In other words, the etch processes are not simple turn-key approaches, and each custom design will require variations in the operating parameters of the system.

The basis for the deep anisotropic etch capability of the STS Plasma Etch System is an iterative cycle of plasma etch and passivation layer deposition steps. A masking layer is formed from either a thick photoresist or a silicon-dioxide layer (3 to 6 µm) on a silicon wafer, and is subsequently patterned using photolithographic and etching techniques to expose the silicon surface pattern to be etched.

The actual silicon etch process in the STS system begins with a brief etch step in which the silicon is etched on the order of 1 to 2 µm, followed by a passivation step. During this step in the cycle, the gas composition and power levels are adjusted such that a Teflon™-like polymer is actually deposited, and no silicon is etched. With appropriate power and pressure during this portion of the cycle, the sidewalls of the etched structure will be coated with a thicker passivation layer than the bottom. As the cycle iterates to the etch step, the silicon is etched preferentially downward because the sidewall passivation prevents lateral etching. The key is to iterate the etch and passivation steps, each with specific durations, such that the desired relative profile is achieved.

Competing requirements include etch rate, selectivity of etching silicon over mask material, critical dimensions and aspect ratio of the features being etched, and effective area of silicon being etched. Thus, small variations in a given design can significantly complicate the etch procedures.

Progress

For initial process development, three specific project requirements were selected, each having different critical requirements to be achieved from the deep anisotropic etch capability. The first is a new impedance sensor fabrication process for the dielectrophoresis project, which used our STS deep-trench etcher to etch 20-µm channels with vertical walls in a silicon substrate. The first step was to back-etch the silicon with the STS etcher to make the fluid input and output ports and electrical contact openings, followed by the growth of 0.2 µm

of thermal oxide on the silicon for electrical insulation. Subsequently, electrodes are formed down the sidewall of the etched channel; thus, it is critical to achieve a uniform, smooth sidewall surface.

The initial process used a standard etch procedure to form the channels with nominally vertical sidewalls.

Upon further inspection, the sidewalls were heavily scalloped, as shown in **Fig. 1**. To solve this problem and create a smoother sidewall surface, the etch and passivation steps were reduced to

where the etch step only proceeded to the point at which the sidewall passivation was removed. While this had the overall effect of reducing the etch rate, it eliminated lateral etching, which resulted in the scalloped profile. **Figure 2** illustrates the final structure with sidewall metallization down into the channel.

The second process investigated the fabrication of a test structure for a high-sensitivity accelerometer for the wireless sensor project. The critical need

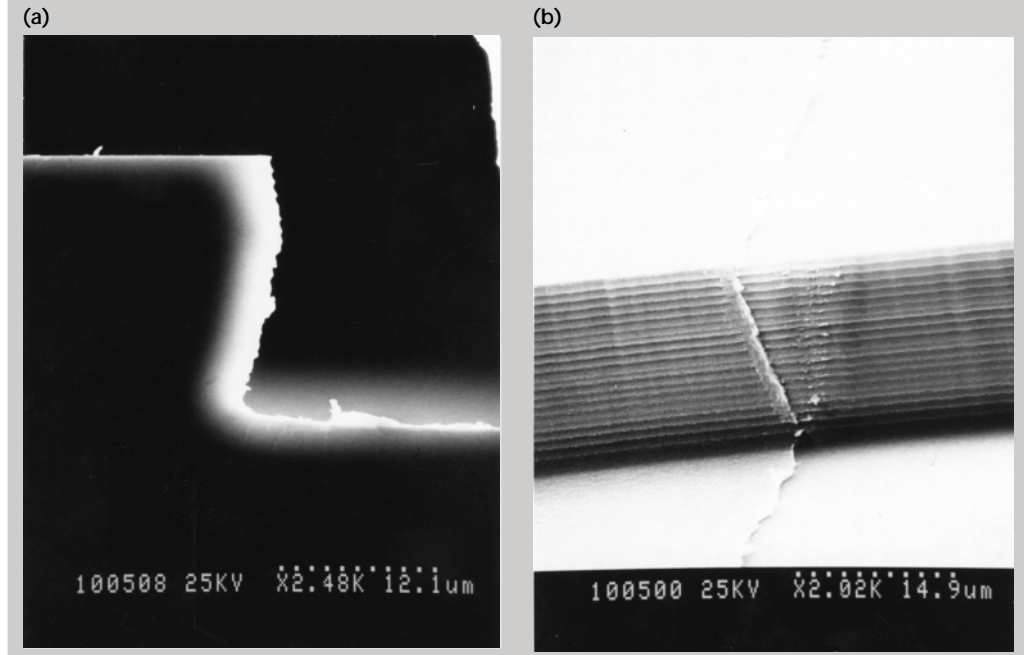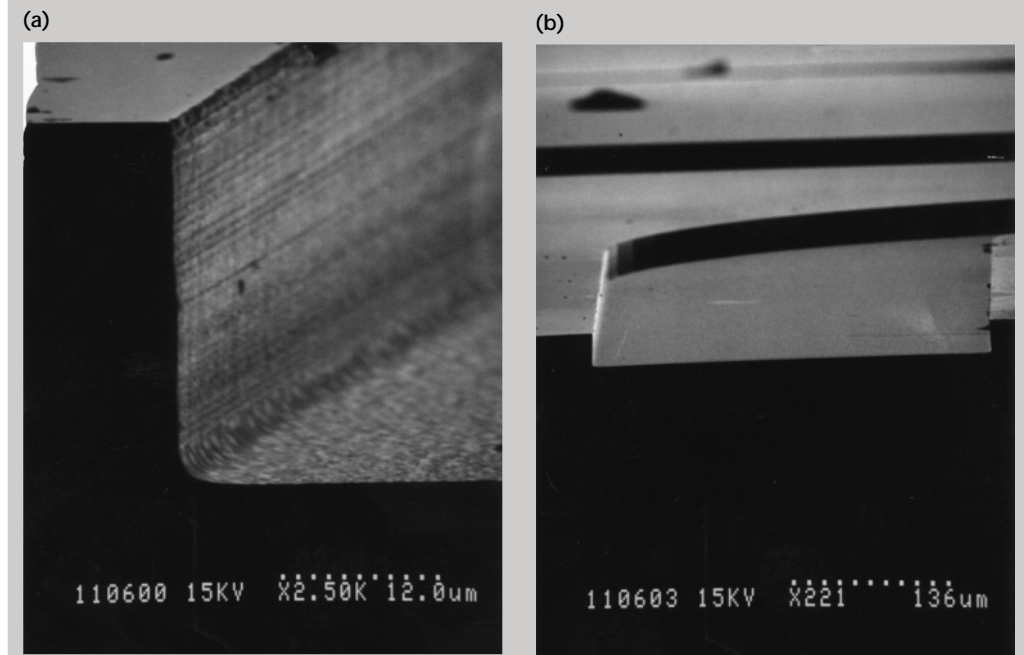*Figure 1. Channels formed with standard etch procedure. Note the heavily scalloped sidewalls.*

(a)

(b)

Figure 2. Final structure, with sidewall metallization into the channel.

(a)

(b)

for this device is an interdigitated finger structure, as illustrated in **Fig. 3a**, in which the fingers are perfectly straight structures through the entire silicon wafer. The critical dimension shown in the blown-up illustration in **Fig. 3b** is 14 μm. The initial process that we used was limited as the depth approached ≥250 μm because the trench would become significantly narrower towards the bottom.

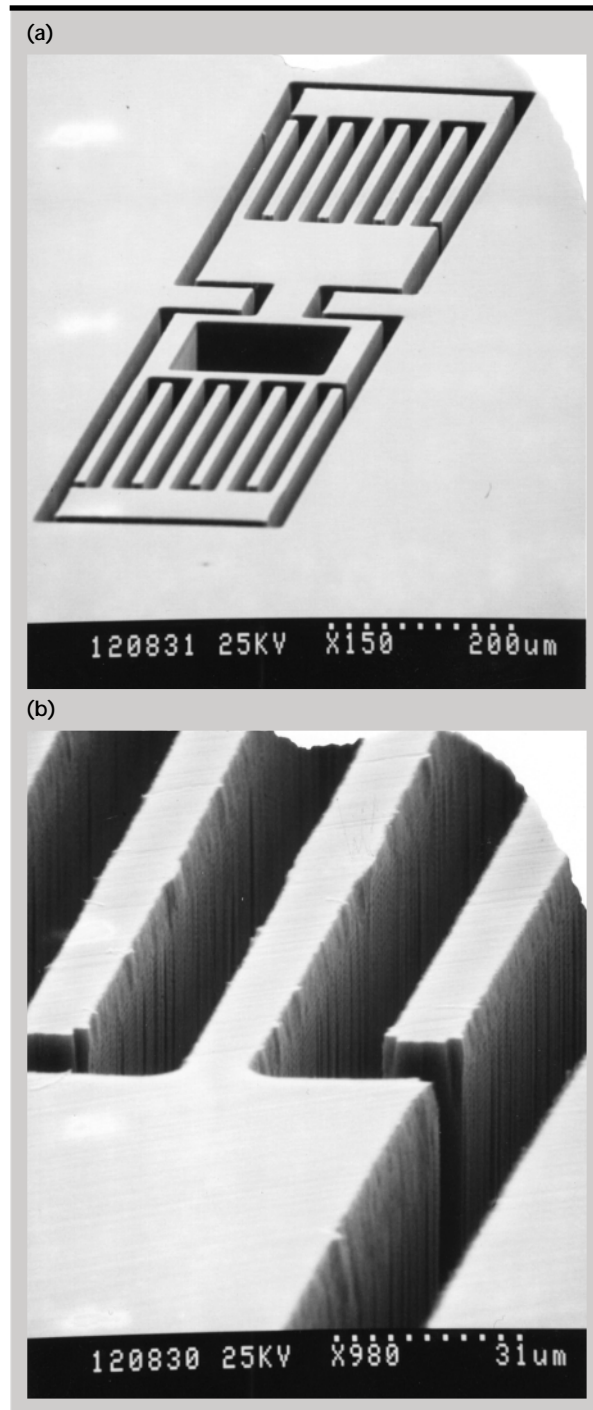

Figure 3. (a) Interdigitated finger structure. (b) Enlargement of (a), with critical dimension 14 μm.

To improve this, the passivation step time was reduced, and the process pressure was increased as the trench depth approached this range. These changes enabled the process to achieve straight sidewall trenches to a depth of 280 μm (14:1 aspect ratio), as shown in **Fig. 4**, but fell short of the required 380 μm of the full silicon wafer. Thus, a hard limitation in aspect ratio was determined, and in this case the structure had to be redesigned with larger critical dimensions (20 μm).

The final process investigates the opposite situation in which a larger trench or via of silicon is etched while leaving a narrow, high-aspect-ratio wall remaining. In this case, a large (1-in. square) array of 100-μm-×-100-μm vias having 20-μm separations was etched (**Fig. 5**). The initial processes resulted in undercutting of the wall structures at fairly shallow depths, leaving a grid structure suspended over a large well. By increasing the passivation step time, the lateral etching was eliminated, and the wall profile was completely vertical. **Figure 6** illustrates the cross section of a wall structure remaining between two etched cavities. The trench is etched to approximately 300 μm in this case, and features are presently being etched through entire silicon wafers (500 μm). Problems still remain in achieving a smooth bottom to the etched cavity as the entire wafer is etched, likely as a result of scattering of the ions off the oxide layer on the back of the silicon wafer, resulting in lateral etching of the trench.
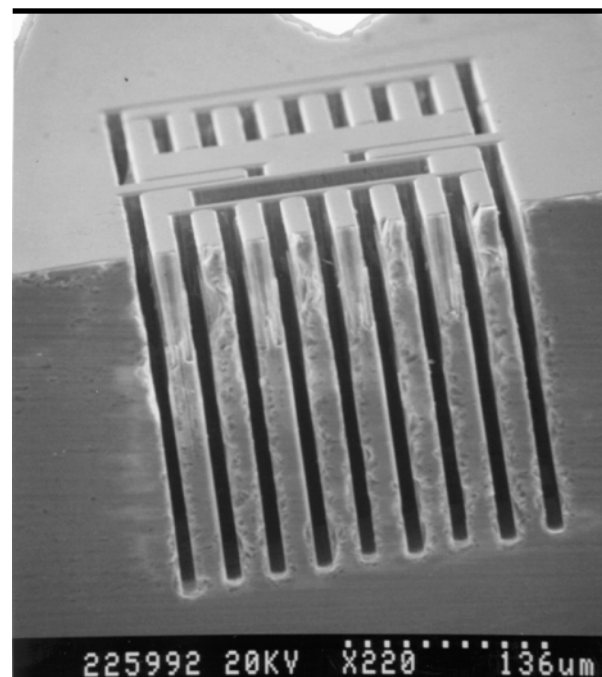
Figure 4. Channels with straight sidewall trenches to a depth of 280 μm (14:1 aspect ratio).

(a)

101125 25KV X37.0 .81mm

(b)

301993 20KV X200 150um
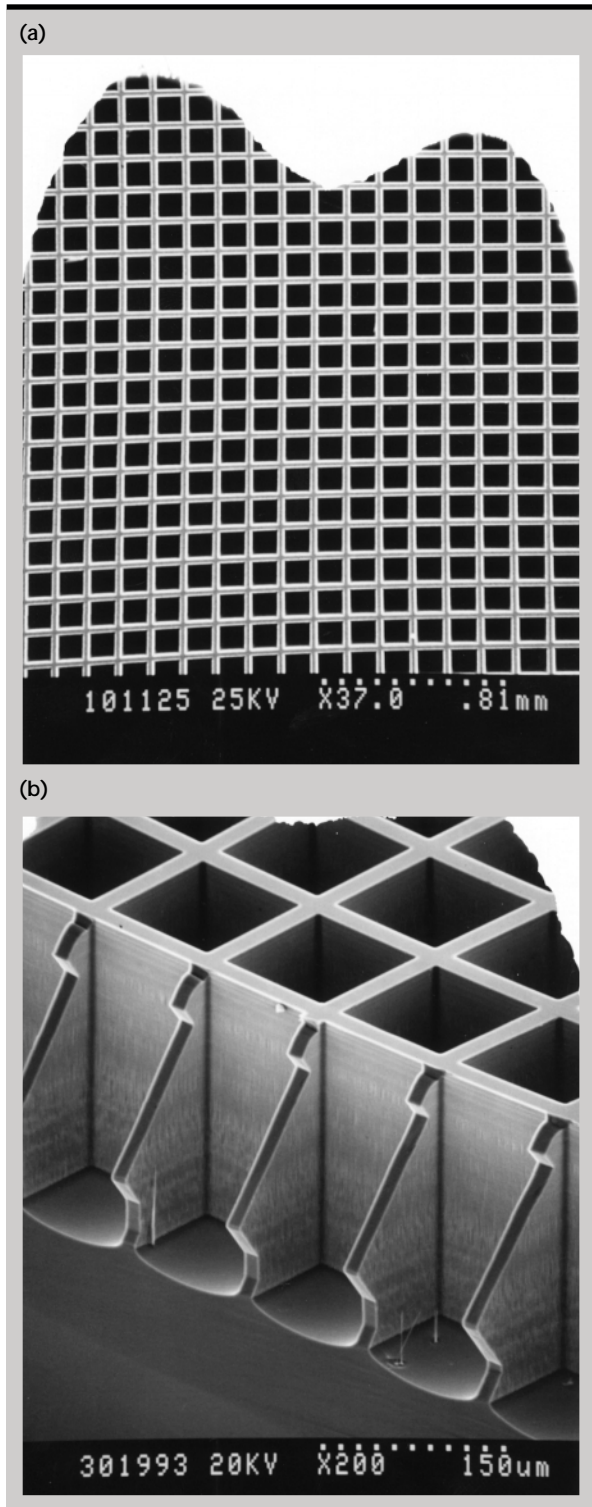
Figure 5. Etching of silicon trench: 1-in. square array of 100-μm-$\times$-100-μm via with 20-μm separations.

301995 20KV X400 75um
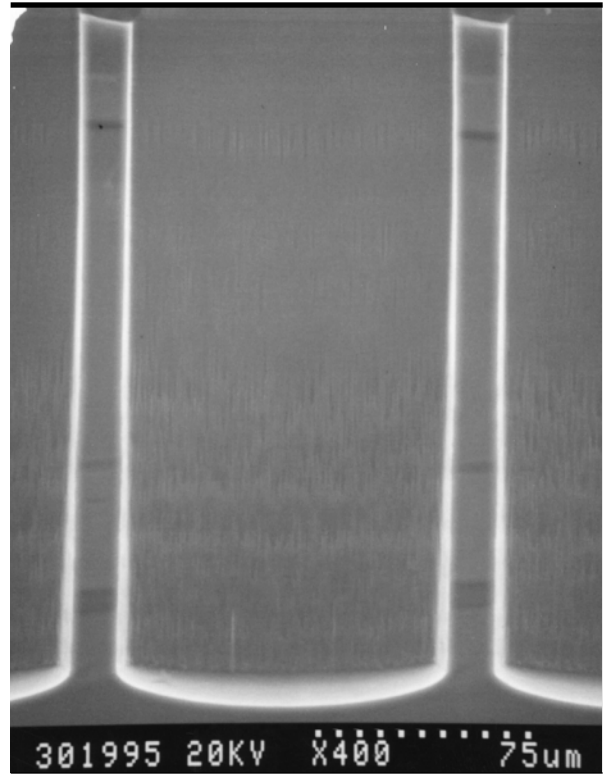
Figure 6. Cross-section of wall structure between two etched cavities.

Future Work

Several processes have been established for the STS Plasma Etch system which enable deep, anisotropic etching of silicon structures for MEMS applications. Our understanding has improved as to which subtle changes in parameters affect the final etch profile and structure. While several key issues remain to be resolved, this effort has provided an important database which will reduce the process design cycle for MEMS projects requiring this capability, and further provide critical design rules and methodologies for future projects.

Micromechanical Characterization Tools for Highly-Filled Polymers

Scott E. Groves and Steve J. DeTeresa
Manufacturing and Materials Engineering Division
Mechanical Engineering

Bruce J. Cunningham
Chemistry and Materials Science
Chemistry

Dino R. Ciarlo
Engineering Research Division
Electronics Engineering

David Allen, K. Clayton, and C. Yoon
Texas A&M University

We are attempting to characterize and model the micromechanical response of highly-filled polymers. In this class of materials, the continuous plastic binder used to bond the highly-filled material dominates the observed viscoelastic response. As a result, realistic lifetime analysis of these materials will require a thorough understanding of the contribution of the plastic binder. In support of our activities we have explored numerous techniques to characterize the microstructure of these materials.

We have made progress in developing an appropriate micromechanical constitutive modeling framework, based on a finite-element method incorporating a cohesive zone model to represent the binder contribution within a Voronoi tesselation mesh structure for plastic bonded explosive (PBX) grains. A second modeling approach was used to incorporate analytical micromechanics (generalized self-consistent schemes). However, preliminary theoretical analysis strongly suggested that this approach would be invalid for extremely high-filled systems like PBX.

Introduction

The mechanical properties of highly-filled polymers (HFPs) are generally dominated by the properties of the binder, because the binder is still a continuous phase, even at low concentrations. An example of this effect is shown in **Fig. 1**. Here, the mechanical properties of a representative PBX are shown to be highly dependent on relatively small changes in temperature. This particular system is composed of 95% high explosive (HE) crystals and 5% binder. Over the temperature range shown, the HE crystals experience no significant change in properties, whereas the binder experiences significant mechanical property changes. This is in large part because the binder has a glass transition temperature that falls within the range of operation.

In general, HFPs are highly time-dependent and nonlinear, with typical applications at Lawrence Livermore National Laboratory (LLNL) requiring more than 30 years of expected service. Long-term modeling will require accurate thermo-visco-elastic/plastic material models with the ability to capture microstructural/*in-situ* properties of the constituents. Developing material models that can relate constituent properties to macroscopic composite properties has considerable benefits, especially in the case of energetic materials. Characterizing the polymer binder independently is simpler and with PBX, poses no safety concern. These tools would also facilitate the incorporation in models of any identifiable chemical or physical aging mechanisms, thus forming a solid foundation for conducting accelerated aging studies on these materials. Furthermore, this suite of tools and models

will enhance the prediction of the mechanical response of new HFP formulations, which in turn, could reduce the qualification time for the replacement of material components.

This paper will discuss our efforts to characterize the local microstructure, to measure *in-situ* properties of the local volume, to measure binder constituent properties, and to perform micromechanical modeling.

Progress

Microscopic Characterization of the Local Volume

This task is associated with developing tools for determining the local microstructure of HFPs. In extremely high-volume filled polymers like PBX, it has been difficult to distinguish the location of the binder phase. Traditional surface microscopy has not been very useful. The example shown in **Fig. 2** represents a Los Alamos National Laboratory (LANL)-developed polarized light microscopy image of a very thin wafer of PBX (which required considerable effort to produce).

Micro-computed x-ray tomography has been explored, but proved to lack the resolution necessary to clearly identify the binder. The best resolutions available are 3 to 5 μm, which falls short of the requirement by better than an order of magnitude.

Atomic force microscopy (AFM) was also explored, but suffered from having incompatible tip designs for probing and identifying soft binder between the grains of HE crystals.

To improve our ability to characterize the local microstructure of PBX, this project applied the majority of its funding to purchase a new type of scanning electron microscope (SEM) that can image organic materials without the need to apply a thin layer of conductive coating such as gold. With regard to coating, our concern has been that the conductive coating would mask some of the microstructural features of interest. The SEM purchased was an LEO 438 Variable Pressure System (**Fig. 3**). LEO is the new name of Cambridge Instruments (developer of the first commercial SEM). This facility has only recently been approved for HE work. Some of the images that we have obtained with this system are shown in **Fig. 4a–f**.

Figure 4c represents our first attempt at imaging a polish surface of LX17. This surface was hand-lapped in an ice water bath to improve KELF polishing. We believe that the lighter material is the KELF binder. It appears light in this image due to electron charging.

To further enhance our imaging capabilities we are exploring stereo image capture and rerendering within the SEM. Modern software and tools developed for the computer gaming industry have made it very user friendly within the PC environment. Our preliminary work with 3-D imaging on filled organics and mock explosives reveals significantly greater depth of field information.

We also intend to explore tagging the binder with a stain or a higher density element during processing to enhance its contrast relative to the filler.

In-situ Property Characterization

A relatively new technique, "Atomic Force Microscopy with Nano-Indentation," was explored to investigate the *in-situ* response (that is, to measure force deflection behavior) on mock HE. It became apparent quickly that current probe
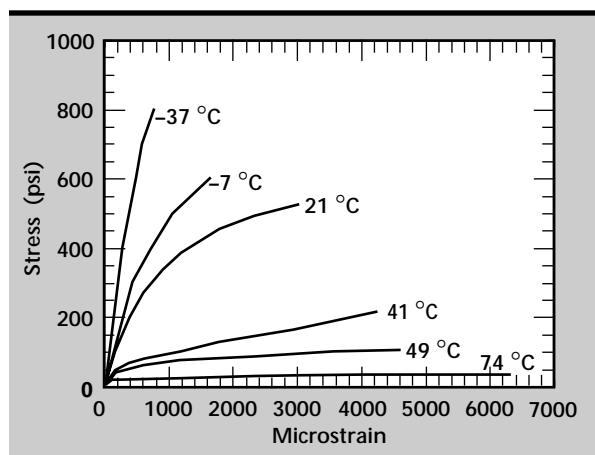

Figure 1. Temperature dependence of tensile properties of PBX-LX14.
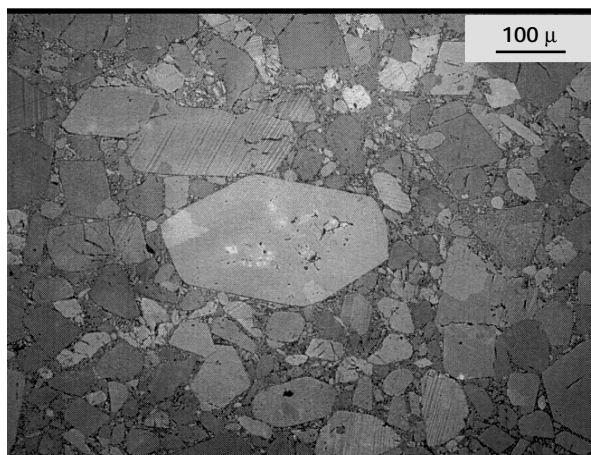

Figure 2. Polarized light microscopy image for PBX from LANL.

designs are grossly inadequate to determine the required *in-situ* properties. What is needed is to reduce the size of the probe diameter while at the same time increasing the probe length. Concurrently, we must also reduce applied forces from micronewtons to nanonewtons.

An effort was initiated to develop our own nano-indentation system around a newly designed, high-aspect-ratio probe tip. Hardware was purchased for what was expected to be our base system foundation, including three stages of nanometer motion control as well as hardware to develop a stereo microscopic viewing system for positioning the nano-indentation probe on the material.

Initially, we planned to measure the viscoelastic properties of the binder material in its position surrounding the HE. To do this, a special probe was needed to apply a constant force on the binder material and measure the displacement as a function of time. It is expected that the material will yield plastically as well as creep. We will also apply a constant strain to the material and monitor the relaxation in force required to maintain this strain. The forces, displacements, and time constants resulting from these measurements will be used in developing micromechanics models.

With limited funding, we have made some progress in the development of the tool set. In some sense, commercial technology has passed us by, with the newly available nano-indentation systems.

We continued development of the high-aspect-ratio tip. For our applications, we need a probe with a circular contact area having a diameter of 0.1 μm and a shaft length of 2 μm. Silicon micromachining
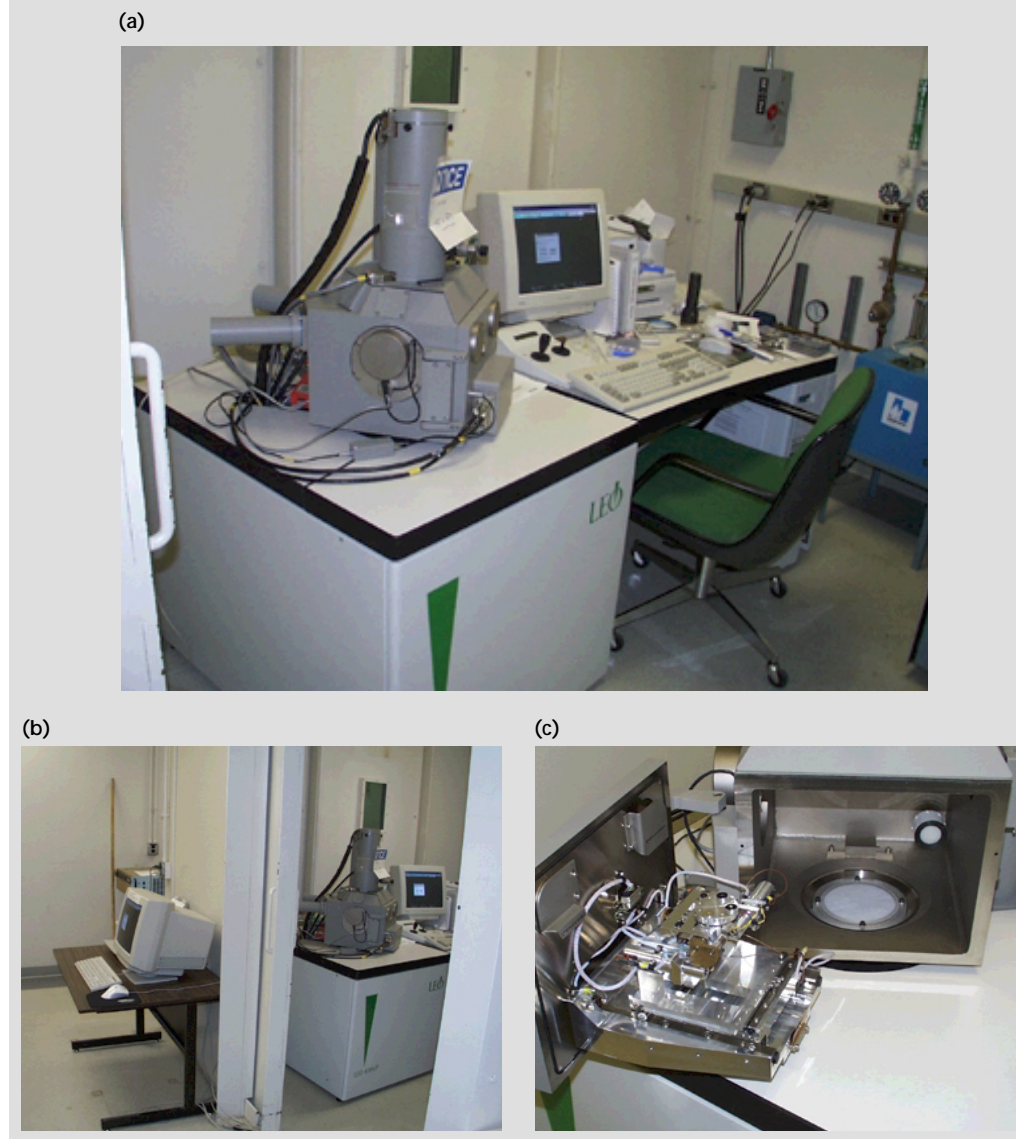
Figure 3. (a) LEO 438 Variable Pressure Scanning Electron Microscope; (b) configured in remote operation for high explosives; (c) scanning chamber open, revealing high explosive filters on turbo pump.

was used to fabricate this probe. The tip has a radius of ~1.5 nm. Just recently this new nano-tip was installed in a traditional AFM. Our recent scans on mock HE have been very encouraging, with the

results shown in **Fig. 5**. In these results, shading is used to denote surface height.

Additional progress has included demonstration of stereo microscopic imaging tools, as well as

(a) Clusters of TATB particles
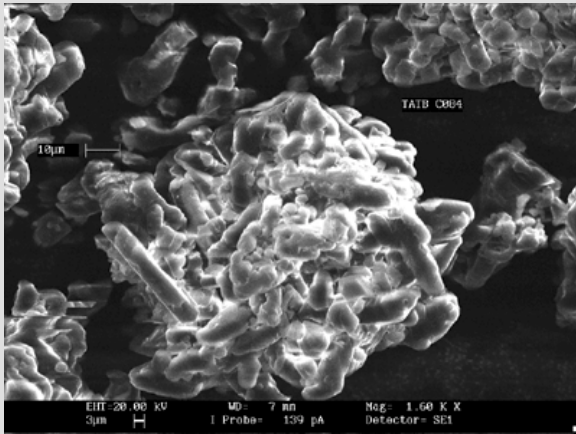
(b) Individual TATB particles
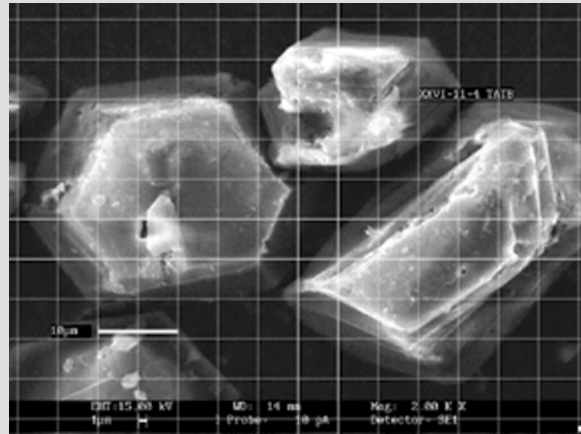
(c) LX17-1 polished surface
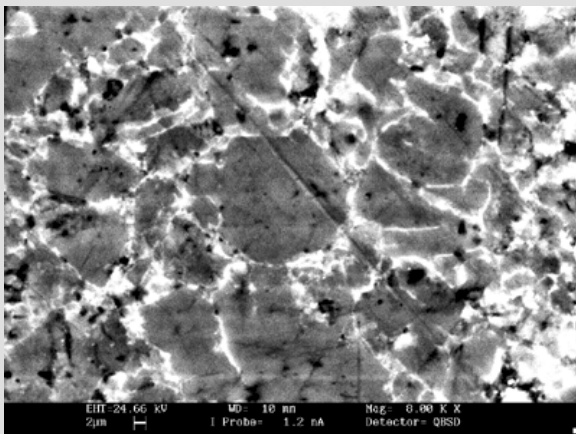
(d) PETN particles used in detonators
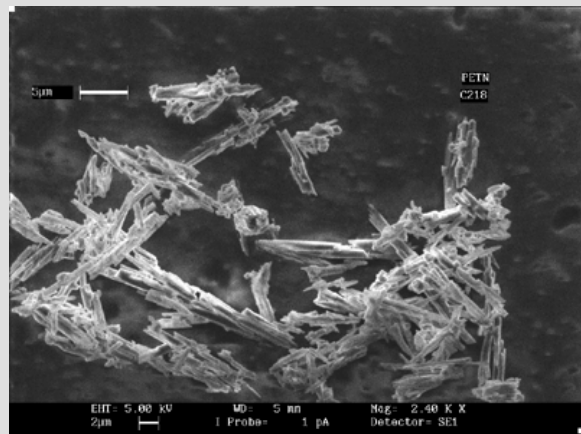
(e) Torsion failure surface of foam
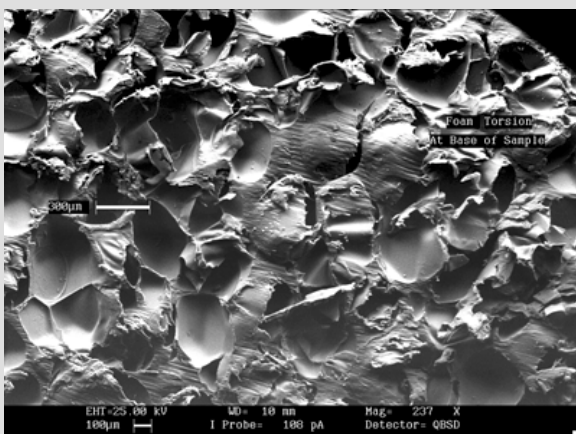
(f) A filled foam
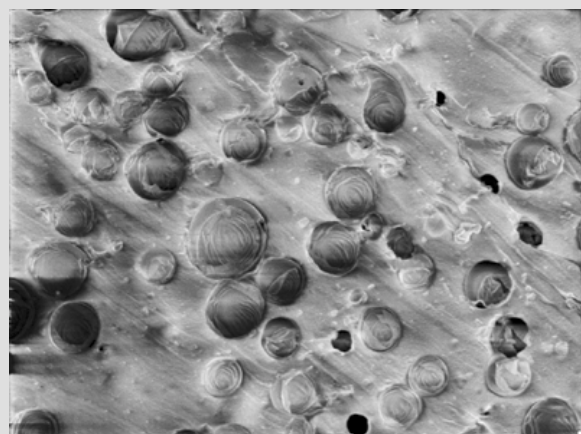
Figure 4. SEM images obtained with LEO 438 Variable Pressure Scanning Electron Microscope. All of the pictures shown were obtained without conductive coatings.

development of a baseline labview control system for the nano-mover stages.

Characterization of Binder Constituent Properties

The objective of this task was to determine the mechanical properties of the individual constituents for the selected material systems. For the case of PBX, our focus was on characterizing the response of the KELF binder used in LX17. Other groups are attempting to characterize the elastic properties of the explosive crystals. Characterizing the mechanical response of binders is not a trivial task. These materials are very soft and require self-supporting grips to prevent premature deformation or bending of the specimen. Furthermore, since the glass transition temperature is spanned by the operating
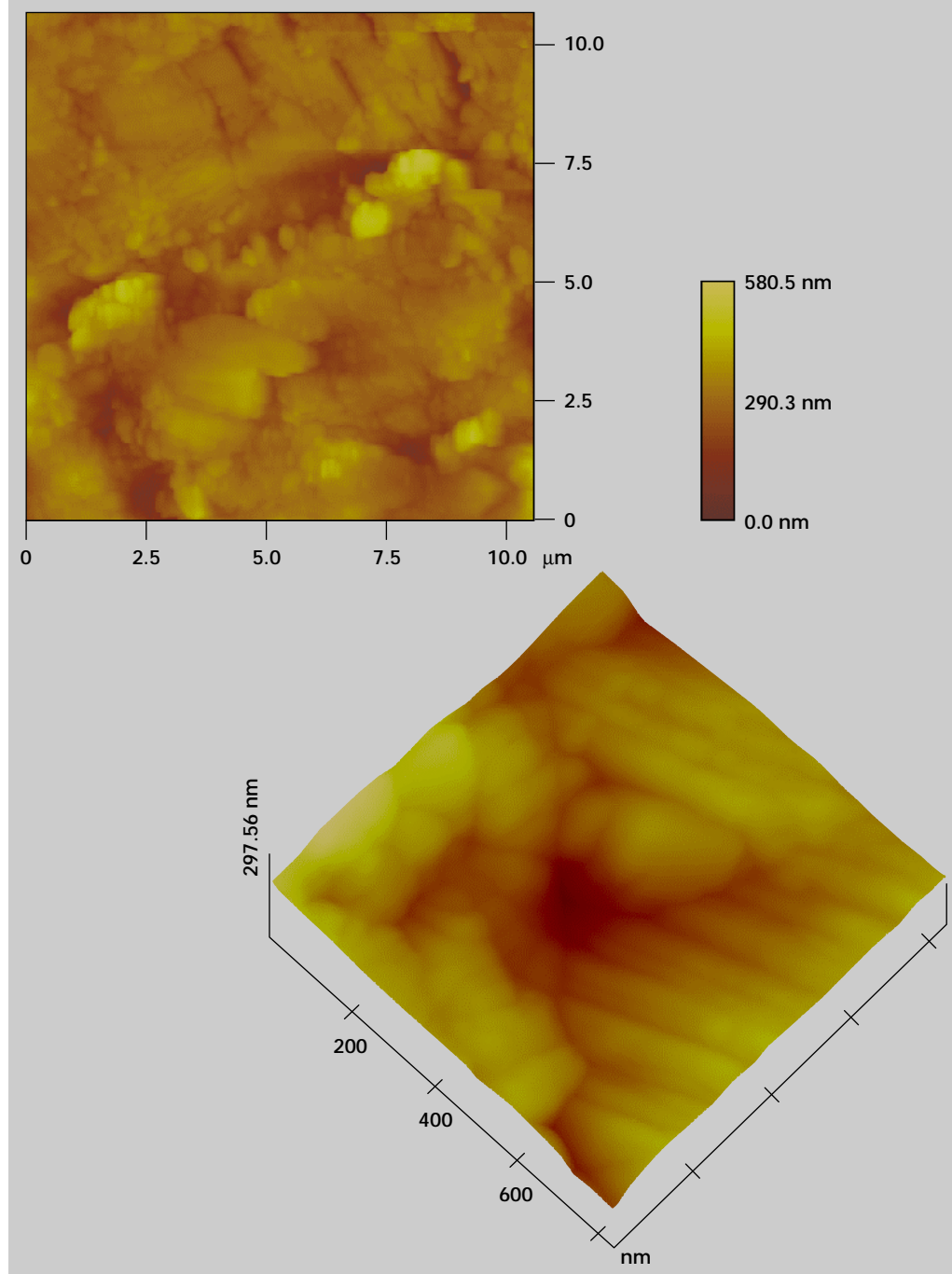
Figure 5. Atomic Force Microscope scans using the recently developed nano-tip probe.

temperature of this system, temperature control during testing is very critical. This has required the installation of water bath temperature controls for maintaining temperature stability, especially at any temperatures near and below 22 °C.

A suite of thermal creep data has been generated on the KELF binder. These results are shown in **Figs. 6** and **7**. This data was converted into compliance data as shown in **Fig. 8**.

For use in finite-element material modeling codes, compliance data must be recast into relaxation modulus data using the following inversely proportional relationship:

$$\tilde{E}(s) = \frac{1}{\tilde{D}(s)}$$

where $D(s)$ is the creep compliance in Laplace space, $E(s)$ is the relaxation modulus in Laplace space, and the ~ indicates the Carson transform. The inverse Laplace transform (ILT) was taken of $E(s)$ to get the relaxation modulus as a function of time. The ILT was performed two different ways—analytically, and using Schapery's Direct method.[1] The different curve fits and different ILT methods were used to make comparisons and thereby decide which method would be the best. The predicted relaxation moduli are shown in **Fig. 9**.

Since the values of the relaxation moduli at the different temperatures differ so greatly, the higher temperatures do not show up well on **Fig. 9**. However, this graph shows the potential for making the master curve of the binder. By using a shift factor and a time scaling factor for the relaxation moduli at different temperatures, the master curve can be obtained for the binder. The shift factor is typically calculated using different methods for above and below the glass transition temperature (T_g).[2, 3] Below T_g, the Arrhenius relation can often be used:

$$\log a_T = \frac{\Delta F}{2.303R}\left(\frac{1}{T} - \frac{1}{T_M}\right)$$

where a_T is the shift factor, ΔF is a constant activation energy per gram mole when R = 1.987 (cal/g-mole K) and T_M is the reference temperature. Above T_g, the WLF form is often used:

$$\log a_r = \frac{-C_1(T - T_M)}{C_2 + T - T_M}$$

where C_1 and C_2 are constants. T_g of this material is around 25 °C, so all except the 35 °C data will be shifted using the Arrhenius form.

Figure 6. KELF binder tensile creep at 15 °C.
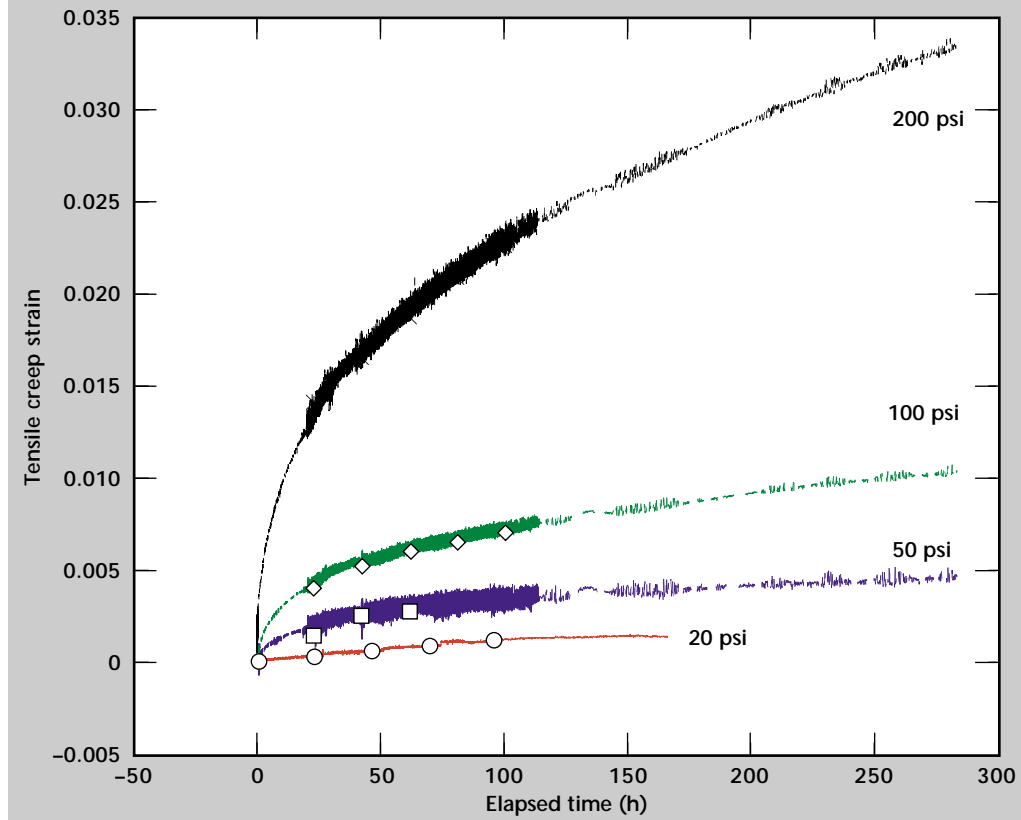
These transformations are made to model the thermorheologically simple thermoviscoelastic material properties of the PBX.

Micromechanical Modeling

In our micromechanical modeling effort we are assessing the merits of two different approaches: analytical micromechanics (a composite spheres model) and finite-element analysis. Common in all methods is the desire to develop a representative local volume element of material. Theoretical
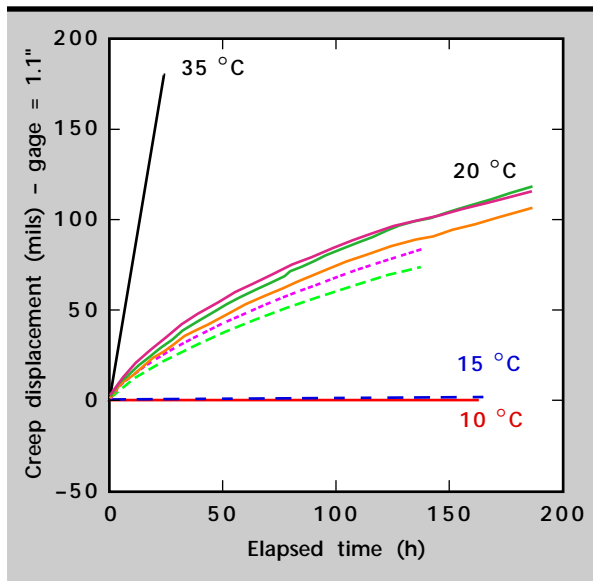
Figure 7. Variation in the thermal tensile creep response of KELF at 20 psi.
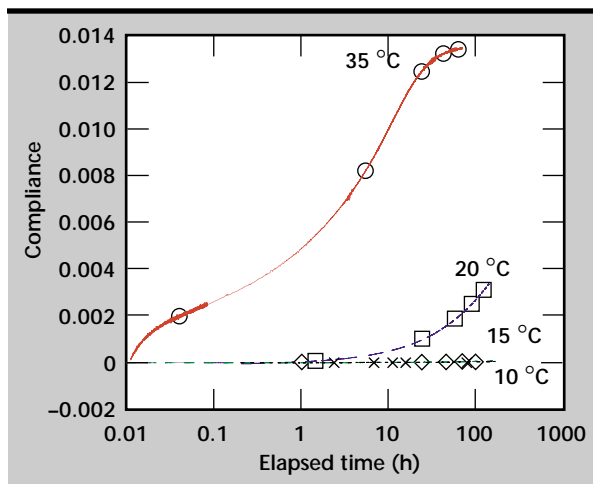
Figure 8. KELF creep compliance data.

analysis of the former analytical approach suggests that method would be inappropriate for modeling extremely highly-filled systems like PBX. The discussion of this is given below.

Inefficiency of Analytical Micromechanics (Composite Sphere Model) for Material System with Inclusions of High Volume Concentration. A very small or large volume concentration formula for heterogeneous material can be validly obtained from the analytic solutions of classical micromechanics by truncating the higher order terms of volume fraction of the inclusion or that of the matrix. However, it has been assumed in the theoretical micromechanics analysis that the contact length between particles (called 'contiguity') is always zero for all concentrations, no matter what the configuration of the inclusion is. Clearly, this assumption cannot be expected to hold for the case of PBX. A citation from a well-known work in the field of theoretical micromechanics reads:

"A fundamental assumption made in this work is that of zero contiguity. Obviously, this cannot be true for a real material. The contiguity is an increasing function of the fractional volume of inclusions and can be expected to be very small only in the case of small concentration. When the concentration is close to unity it would appear more reasonable to assign the role of matrix to the inclusion material and that of inclusions to the matrix."[4]

The suggestion about switching the roles of inclusions and matrix does not seem to be reasonable even when no damage is introduced, since the inclusions (explosive particles) have elastic material behavior whereas the binder material (matrix) behaves viscoelastically. Once damage evolves and cracks propagate in the

Figure 9. Predicted relaxation moduli for KELF binder.

matrix, this proposed role reversal continues to be unrealistic.

Aside from the contiguity problem, there are other difficulties in using analytic estimation to obtain the effective moduli. It is commonly believed t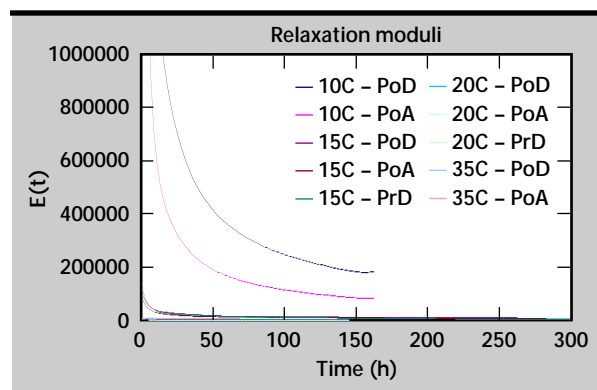hat whenever the difference in moduli between inclusions and matrix materials is not too large, the upper and lower bounds will be close together. However, in such an extreme case as PBX, the bounds are not close enough to provide a good estimation of an effective moduli of the composite.

Analytic theory has another discrepancy. The composite spheres model cannot account for the size deviation effect and irregular shape effect that play critical roles in estimating the effective material properties. Inclusion particle sizes in PBX show large scatter. In addition, it has been shown that the inclusion particles in PBX have various irregular shapes and most of them are of sharp configuration. Wherever the explosive particles have sharp corners or acute angled edges, a stress concentration is expected. These stress concentrations will make damage evolve in the binder material, and the damage evolution consequently leads to more stress concentrations. With the composite spheres model these effects are not accounted for, so that the subsequent prediction of damage evolution will necessarily be erroneous. For these reasons, finite-element methods are being studied in this research with the expectation that they will better predict damage-dependent, effectively averaged properties for PBX.

Finite-Element Approach. In our finite-element material modeling effort we are using Voronoi tessellation mesh structures[5–7] to simulate the distribution of the highly-filled component and a cohesive zone model[8, 9] between each component. The fundamental idea in this approach is to reduce the effects of the extremely low volume material to that of a line function in the finite-element mesh, thus avoiding the tremendous memory penalty for modeling both grains and binder.

The later method of modeling both grains and binder from a pure continuum sense within the finite-element algorithm will be explored in the future. It is essential to have correct material properties for the line function. (This approach might be considered similar to having a tied slide line, as in NIKE, except

the line will have constitutive properties). The advantage of the cohesive zone model, which contains double nodes at each point, is in the facilitation of simulated damage (fracture between the grains) in our representative local volume. Homogenization of the boundary response (with or without damage) leads to a set of representative properties.

For our particular case the highly-filled component is the explosive grains, and the low concentration material is the viscoelastic binder, KELF.

Two meshes, shown in **Fig. 10**, will initially be used to model the material. They are double-noded meshes with 30 grains and 100 grains, respectively. Since the material has such a high volume fraction (~92%), a refined mesh with a finite space between grains is difficult to generate. Therefore, we are using these meshes with a cohesive zone model and zero opening dimension in the undeformed configuration along the grain boundaries to model the binder. The relaxation moduli obtained through the method described previously are fitted using a Prony series that is used in the cohesive zone model. The characteristic length scale of the cohesive zone and the Young's modulus of the particles (grains) are still unknown but are necessary if we hope to achieve an accuracy in our finite-element models. Preliminary
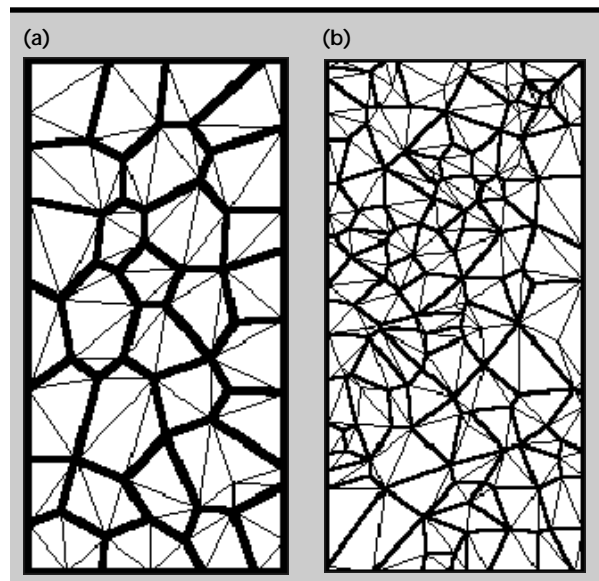

Figure 10. Preliminary Voronoi finite-element mesh structures for PBX. Mesh (a) is a 30-grain and 97-element model. Mesh (b) is a 100-grain and 292-element model. One of our goals is to determine the convergence of mesh refinement.

properties for the elastic behavior of the explosive grains will have to be initially estimated by extrapolation from measured PBX global properties.

Summary

This project has served to further the development of those tools necessary to characterize HFPs. When further developed and linked together with the viscoelastic modeling tools, this methodology will provide a basis for estimating the useful lifetime and identifying any age-related problems for these materials.

References

1. R. A. Schapery (1967), "Stress analysis of viscoelastic composite materials," *J. of Comp. Mat.*, Vol. **1**, pp. 228–267.

2. L. C. E. Struik (1978), "Physical aging in amorphous polymers and other materials," Eksevier Scientific Publishing Co.

3. R. M. Christensen (1962), "Theory of viscoelasticity," Academic Press, New York, New York.

4. Z. Hashin (1962), "The elastic moduli of heterogeneous materials," *J. of Appl. Mech.*, pp.143–150.

5. G. J. Rodin (1995), "Stress transmission in polycrystals with frictionless grain boundaries*," J. of Appl. Mech.*, March, Vol. **61**/2.

6. M. W. D. Van Der Burg and E. Van Der Giessen (1994), " Delaunay-network modelling of creep failure in regular polycrystalline aggregates by grain boundary cavitation*," Int. J. of Damage*, Vol. **3**, April.

7. M. O. Starzewski and C. Wang (1989), "Linear elasticity of planar Deluanay networks: random field characterization of effective moduli," *Acta Mechanica*, Vol. **80**, pp. 61–80.

8. C. Yoon and D. H. Allen, "Damage dependent constitutive behavior and energy release rate for a cohesive zone in a thermoviscoelastic solid," submitted to *Int. J. of Fracture.*

9. F. Costanzo and D. H. Allen (1993), "A continuum mechanics approach to some problems in subcritical crack propagation," *Int. J. of Fracture*, Vol. **63**, pp. 27–57.

Advanced Imaging Catheter

Amy W. Wang and Abraham P. Lee
Electronics Engineering Technologies Division, Center for Microtechnology
Electronics Engineering

Daniel L. Schumann
Manufacturing and Materials Engineering Division
Mechanical Engineering

**Luiz Da Silva, Matthew J. Everett, Billy W. Colston, Jr.,
Steve B. Brown, and Dale L. James**
Medical Technologies Program

Richard A. London and Peter Amendt
Defense and Nuclear Technology

Optical coherence tomography (OCT) imaging of arterial vessels has been previously demonstrated using a single fiber rotated in the central lumen of a catheter. OCT images have been shown to provide improved resolution (<10 µm) over ultrasound images. We have fabricated a prototype catheter that uses embedded optical fibers in the inter-wall lumens of a catheter tube for OCT imaging. Using inter-wall lumens of the catheter keeps the central lumen open for insertion of surgical instruments during minimally invasive procedures, while permitting continuous on-board imaging. We have also explored actuation techniques for articulating the tip of the catheter for steering through arterial vessels during catheter positioning.

Introduction

Minimally invasive surgery (MIS) is an approach whereby procedures conventionally performed with large and potentially traumatic incisions are replaced by several tiny incisions through which specialized instruments are inserted. The key advantage of this technique is that recovery time can be reduced from months to a matter of days. Early MIS, often called laparoscopic surgery, used video cameras and laparoscopes to visualize and control surgical devices. The difficulty is that the images produced using these techniques are 2-D projections of a 3-D network. The surgeon, as a consequence, is often uncertain which direction to navigate the catheter. Toxicity issues, moreover, limit the continuous use of contrast agents, so often the surgeon is unable to visualize any component of the arterial network.

Catheter-based minimally invasive procedures are a rapidly-growing sector of all surgical procedures. These include balloon angioplasty, now performed on an outpatient basis, aneurysm treatment, and laser thrombolysis. In the U.S. over one million catheter procedures are performed annually, representing a market of over $500 million. An example of a catheter-based procedure is one in which a catheter is navigated into the neck of an aneurysm, and then embolizing coils coated with thrombolytic (clotting) agents are inserted into the aneurysm to initiate thrombus. This is a very difficult procedure that can often take hours of manipulation to accurately position the catheter within the neck of the aneurysm. At times, the procedure cannot be performed, simply because the catheter cannot be positioned.

Practicing clinician contacts have repeatedly mentioned the frustration at not being able to navigate and image at the catheter tip. The difficulty can be appreciated when you consider that catheters are hollow polymer tubes that can be as long as 2 m and taper down to outside diameters of 800 µm and working channel diameters of 500 µm. They are made soft and pliable to reduce the possibilities of perforating

arteries or damaging the arterial wall. This makes the control problem similar to pushing on a string. Both the navigation and artery damage problems could be solved if we could produce a compact catheter that offers imaging and active control capabilities to guide and position the distal end (the end in the body). Clinicians have emphasized that if we could produce such a device it would be a tremendous breakthrough.

Previous work[1] demonstrated imaging through the use of optical coherence tomography (OCT), a non-invasive, non-contact optical technique for imaging through highly scattering media.[2–4] Although analogous to ultrasound imaging in many ways, OCT offers superior depth (<20 µm) and lateral spatial resolution (<10 µm). In addition to providing improved resolution over current "snap-shot" imaging systems, the use of OCT will also significantly reduce the amount of x-ray dosage to patients and physicians and allow procedures to be completed without the need of cumbersome lead vests. The ultimate benefit of the advancement of catheter and surgical technology is a critical path for improving patient survival and clinical success.

Progress

To date we have demonstrated an OCT imaging system that is ten times faster than our previous system. This gives us the ability to acquire eight fiber images at 10 Hz, which is adequate for a practical medical device. In addition, we have developed a compact (18-in. × 18-in. × 3-in.) fiber optic system replacing large rack-mounted instruments and improving reproducibility. The design of the optics at the distal ends of the fibers has been greatly

improved, making 150-µm-diameter probes feasible while significantly reducing manufacturing cost and enhancing robustness. An *in vivo* image of a pig artery taken with the OCT system using a 250-µm-diameter probe is shown in **Fig. 1**.

A prototype catheter (**Fig. 2**) has been built in which optical fibers are threaded through internal lumens in the catheter wall (**Fig. 3**). An imaging prototype is being fabricated that integrates two single-mode optical fibers in the 250-µm-diameter inter-wall lumens of a 1.5-mm-diameter catheter tubing with a 900-µm-diameter center lumen. This fiber optic probe has the capability of imaging the tissue through the side walls of the catheter, while leaving the central lumen of the catheter available for a medical device.
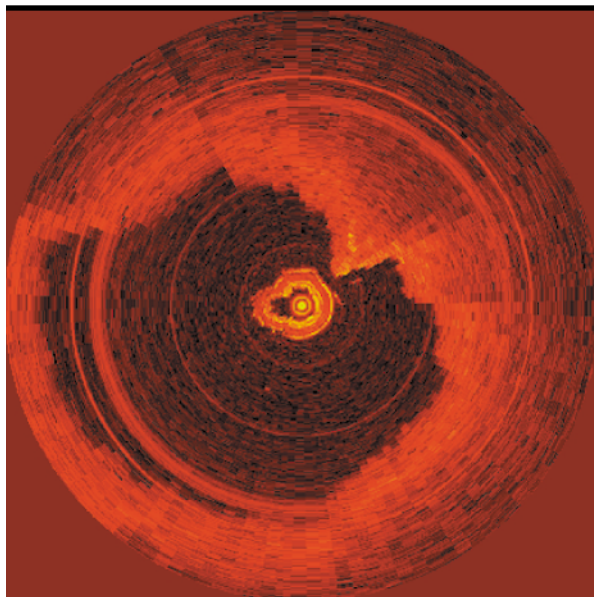

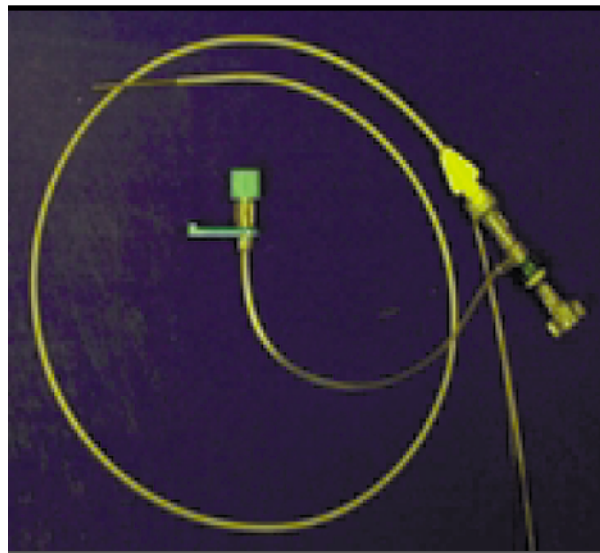Figure 2. Multi-lumen catheter prototype.

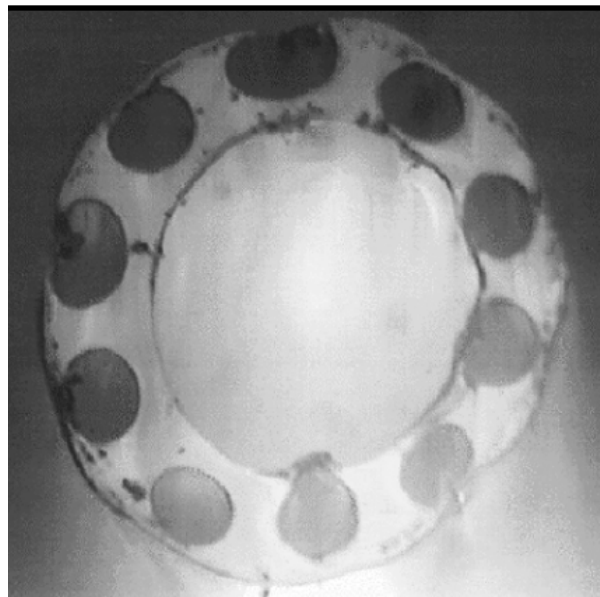Figure 1. In vivo image of a pig artery using the OCT system.

Figure 3. Example of multi-lumen catheter tubing with inner-wall lumens for optical fiber and actuator integration.

(a)

(b)
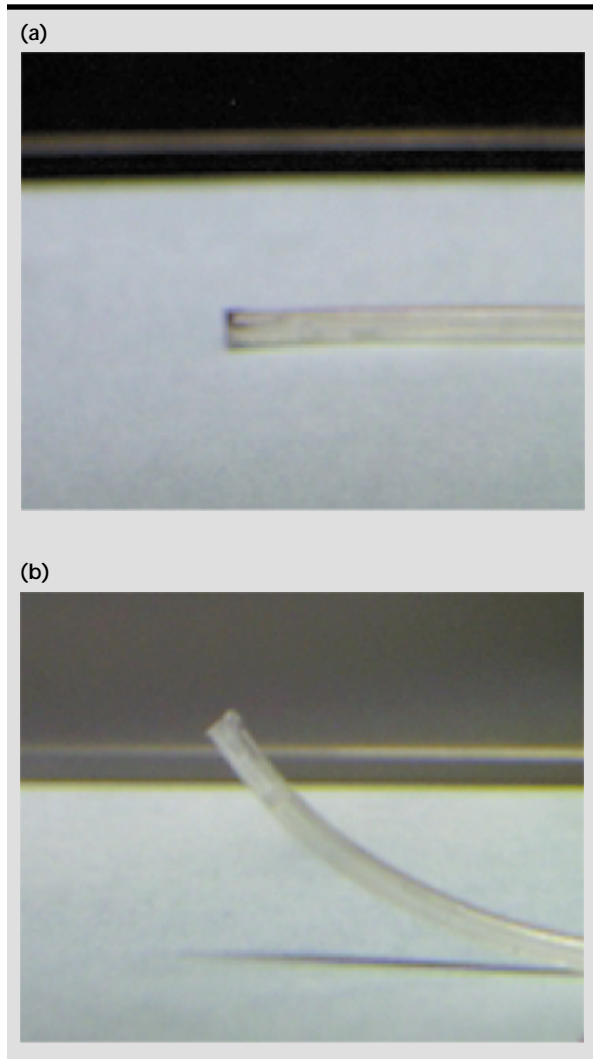
Figure 4. Catheter tip articulation actuated by heating of SMA wire threaded along catheter wall lumens.

Figure 5. Predicted OCT signal from a single imaging fiber in blood-filled artery.

Catheter tip actuation has been tested using a shape memory alloy (SMA). SMAs undergo a reversible temperature-dependent transformation between a low-temperature martensite phase and a high-temperature austenite phase. These materials are able to recover large amounts of mechanical deformation (strain) upon heating. In a technique similar to Takizawa *et al.*[4], nickel titanium (NiTi) wire was mechanically stretched in length then threaded up and down two adjacent catheter wall lumens. The wire was resistively heated, shrinking the NiTi wire to its original length, causing the catheter tip to bend (**Fig. 4**).

We have also developed the capability to model OCT imaging. Specifically, we modified existing Monte Carlo photon transport codes to track the phase and path length of photons propagating through biological tissue and an OCT imaging system. In **Fig. 5** we show the predicted OCT signal from a single imaging fiber in an artery filled with blood. The results show the rapid decay in photon signal as you move away from the fiber surface due to the high scattering coefficient of blood. The artery wall is identified by a jump in the observed signal attributable to increased scattering. The results are in good agreement with the data collected in previous experiments.

Future Work

We have demonstrated a prototype catheter with on-board imaging capability with an open central lumen for introducing surgical instruments during a procedure. We have also tested an initial tip articulation using SMA-based actuation. In the future we will pursue alternative designs for catheter tip articulation.

References

1. B. W. Colston, Jr., M. J. Everett, L. B. Da Silva, L. L. Otis, P. Stroeve, and H. Nathel (1998), "Imaging of hard and soft tissue structure in the oral cavity by optical coherence tomography," *Appl. Opt.*, **37**(16), 3582.

2. D. Huang *et al.* (1991), "Optical Coherence Tomography," *Science* **254**, 1178.

3. G. J. Tearney, S. A. Boppart, B. E. Bouma, M. E. Brezinski, N. J. Weissman, J. F. Southern, and J. G. Fuijimoto (1996), "Scanning single-mode fiber optic catheter-endoscope for optical coherence tomographys," *Opt. Lett.*, **21**, 541.

4. H. Takizawa, H. Tosaka, R. Ohta, S. Kaneko, and Y. Ueda (1999), "Development of a microfine active bending catheter equipped with MIF tactile sensors," *Proc. Twelfth IEEE Ann. Conf. on MEMS*, Orlando, Florida, 412.

Intelligent Wavefront Reconstructors for Adaptive Optics

Chi Yung Fu
Electronics Engineering Technologies Division
Electronics Engineering

George F. Chapline
Physics Directorate

Scot S. Olivier
Information Science and Technology Program
Laser Programs

Loren I. Petrich
University of California at Berkeley
Berkeley, California

We have successfully demonstrated our algorithm for wavefront reconstruction from gradients in one dimension. We have achieved both of our goals: a great reduction in computational load within an error of less than 2%.

Introduction

Developing different paradigms for adaptive and intelligent control systems for adaptive optics (AO) will provide state-of-the-art control technology for many Lawrence Livermore National Laboratory (LLNL) programs.

For example, many current and future high-priority programs, such as the National Ignition Facility (NIF) and Laser Guide Star (LGS) for the Lick and Keck Observatories, are critically dependent on their capabilities in advanced wavefront control for their success. Unless this problem is solved, it may impact the delivery of these systems at a reasonable cost. The economic implications for just two of the many important applications—the development of programs for DOD laser weapons with potential values of $10 to 100M, and the extreme UV lithography programs worth over $100M—provide strong motivation for this project.

This project directly aligns with LLNL's core competency areas and also impacts areas such as national defense and nonproliferation, advanced sensors and instrumentation, atmospheric sciences and geosciences, and computational engineering.

Scope

The central problem in AO is reconstructing the distorted wavefront of incoming light so that one can then adjust a deformable mirror to compensate for its distortion. Using traditional technology, these calculations require solving a system of linear equations resulting in a computational complexity of N^2, where N is the degree of freedom or the number of actuators for the deformable mirror.

The goal of this project is to develop different paradigms for adaptive and intelligent AO control that would be scalable for systems with a few hundreds of degrees of freedom, up to tens of thousands or even hundreds of thousands of degrees of freedom.

The specific problems we are trying to solve here are the performance and cost issues that arise for adaptive wavefront control when we scale the number of degrees of freedom up to tens or hundreds of thousands. Our first goal is to demonstrate that in 1-D, the computational requirement of our proposed new paradigm will scale with N, rather than N^2. This new scaling implies that desirable performance and reasonable cost will be attainable

even if N is very large, thus getting to the heart of this problem. Our second goal is to demonstrate that the error in adopting our paradigm will be acceptable (less than 2%).

Solutions and Architecture

Broadly speaking, there are two very different approaches to solving the problem. One would be to replace the current sensors with more sophisticated ones. An example is the use of interferometers to directly measure phase rather than the phase gradient and thus eliminate the need for wavefront reconstructors. This new approach, however, faces uncertainty in terms of cost, noise, and other factors. The other approach would be to improve wavefront reconstruction by using existing or future sensors. By speeding up the wavefront reconstruction at a lower cost, one could essentially solve the problem.

Up to now the existing technology has been adequate for addressing the requirements of most AO as long as the number of degrees of freedom is limited. However, for many new applications that require a multiple-order-of-magnitude scale-up in the number of mirror segments, or equivalently, the number of pistons that control the mirror's shape, and also an increase in system speed to accomplish wavefront control in real time, the traditional approach is neither efficient nor economical.

Thus for applications that need corrections not only at local and global levels but at all the levels in between, we have investigated a multi-level, multi-resolution solution. Using an iterative method, we work towards an approximate solution instead of an exact one and thus a substantial amount of computational time can be eliminated.
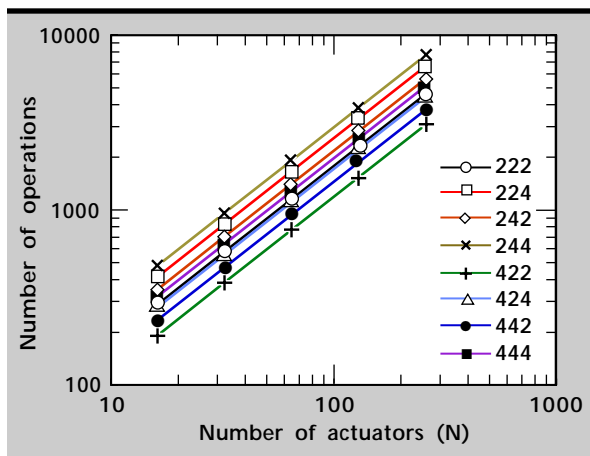
Computational Performance–Cost Analysis and Results

Through 1-D simulation we have worked out the number of calculations needed for various configurations. These are shown in **Fig. 1**. The parameter values are shown in the legend, and are, in order, the averaging factor, the number of outputs, and the pad size. As we can see within this range of parameters, for 256 degrees of freedom the number of operations is between 3840 and 7680, instead of 65536 in the case of traditional methodology. Using our algorithm, the range of computational load also allows us to trade off computational complexity with accuracy.

Error Analysis and Results

Though we have demonstrated an approach that reduces the computational complexity, there is the serious question of whether it is possible to get the error down to an acceptable level with the number of operations much less than N^2. For Fourier transforms, the answer seems simple: the translational symmetry of the problem makes the solution of the problem a simple $O(N)$ calculation in the Fourier domain, though there is the complication of boundary conditions.

For our algorithm, there is no such exploitable symmetry, but the expected behavior of the turbulence provides an answer. Atmospheric turbulence follows Kolmogorov's law, with the turbulent energy being proportional to $k^{-11/3}$. This translates into a turbulent amplitude that is proportional to $k^{-4/3}$, and our system made use of this feature to achieve acceptable errors, as can be seen in **Fig. 2**, which shows the error achieved for each level in the multi-level structure.

Figure 1. Number of operations as a function of number of actuators and local configuration.
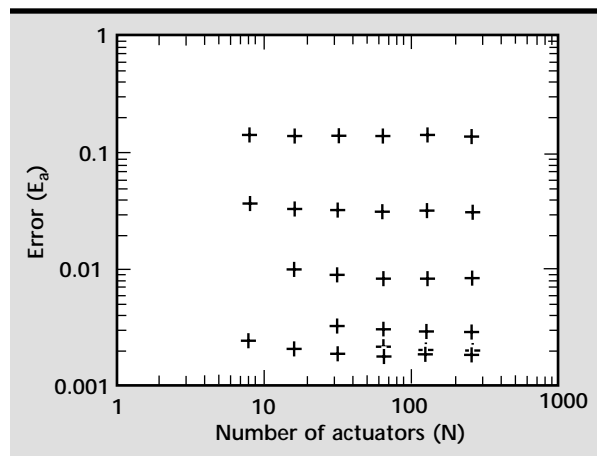

Figure 2. Error per level.

Acknowledgments

We would like to acknowledge the support of the Engineering Department and the Laser Directorate for this work. We are especially indebted to Drs. R. Deri, J. Brase, G. Suski, and R. Langland for their encouragement and their faith in this project.

Lambda Connect: Multiwavelength Technologies for Ultrascale Computing

Michael C. Larson, Steven W. Bond, and Michael D. Pocha
Electronics Engineering Technologies Division
Electronics Engineering

Mark A. Emanuel
Laser Science and Technology Program
Lasers

Mark E. Lowry
Information Science and Technology Program
Lasers

Byte-wide, multiwavelength optical interconnects can substantially improve the performance of the system interconnects used in ultrascale computing platforms ("supercomputers"), leading to substantial improvements in overall system performance for applications that require global communications within the supercomputer. Optical hardware required for such interconnects includes byte-wide multiwavelength transmitters and wavelength routing and filtering modules. This year, we have fabricated and characterized a byte-wide four-wavelength transmitter and developed the technology to increase wavelength count to eight and beyond. In addition, we have dramatically increased the wavelength range available for large-wavelength count systems by demonstrating long-wavelength emitters. Finally, we have developed a photon-conserving wavelength routing module to more efficiently connect multiple transmitter and receiver modules.

Introduction

Ultrascale computing—the integration of large numbers of processors into a single, highly capable multiprocessor system—is currently of great interest in several DOE and other government programs. These systems contain 100s to upwards of 1000 CPUs, to attain computing capabilities from 100 GFLOPS to 100 TFLOPS and beyond. The provision of fast data communications within such systems poses a significant challenge. Effective communication is currently hampered by the bandwidth, latency, and congestion characteristics of the electronic fabric used to interconnect the many system processing and memory elements. This communications bottleneck can substantially degrade computational performance, significantly complicate programmability, and cause inefficient use of costly memory resources.

The recent emergence of byte-wide optical interconnects, which use linear arrays of multimode optical fibers in a ribbon cable assembly, has substantially improved the cost and performance of

Gbyte/s point-to-point communications. To fully leverage this technology, however, the latency and congestion issues with distributed electronic switching must be overcome. We have recently proposed to perform source-routed switching in the optical domain using a wavelength-switching mechanism, and shown that this approach can yield highly capable switches that support 100s of Gbyte/s ports and yield minimal internal congestion and latency. Instruction-level simulation has demonstrated the advantages of this approach.[1]

To implement this multiwavelength optical interconnect requires the addition of multiwavelength capability to the existing byte-wide optical interconnect. The required components, which include optical transmitters capable of fast wavelength tuning and fixed optical filters, differ substantially from existing telecommunications fiber optics. All components must be compatible with existing multimode fiber ribbon cables, and provide compact form factors suitable for populating electronics boards. This project aims at developing prototypes of these

components, to investigate the feasibility of implementing byte-wide, multiwavelength optical interconnects for ultrascale computers.

Progress

Multiwavelength Transmitters

We have fabricated and characterized prototype modules with the capability of transmitting on any of four selectable wavelengths. The module wavelength is selected by directing current into different lasers, each laser emitting at a different wavelength, so that current switching is used to provide fast wavelength switching on a timescale of the laser modulation bandwidth (1 to 2 ns switch time). Each module contains one linear array of 10 laser diodes for each wavelength, with a moderate channel separation (8 to 10 nm) that minimizes issues associated with wavelength registration, uniformity, and drift between different photonic components within the interconnect. Each array element can be independently addressed (modulated) by a current drive, so that the module can transmit 10 independent data streams comprising the 8 bits in an electronic data word of 1 byte capacity, plus clock and framing.

Our modules use arrays of vertical cavity surface-emitting lasers (VCSELs), which we have fabricated from GaAs/InGaAs/AlGaAs semiconductor layers grown by molecular beam epitaxy. Our VCSEL design uses an oxidized AlAs layer to control the "active region" of the laser which is pumped by the applied current drive, to achieve lasing thresholds of less than 2 mA for devices of 7 to 10 µm oxide aperture. The VCSELs are sized to emit in multiple transverse modes (1.5 nm spectral extent), to minimize speckle noise during multimode fiber transmission. These devices provide milliwatts of optical power when pumped with <10 mA at voltages ≤3 V, conditions compatible with conventional complementary metal oxide semiconductor (CMOS) electronic drive electronics.

This year, we fabricated and fully characterized a byte-wide four-wavelength transmitter module under high speed modulation. We used a combination of direct fiber coupling and broad-band add/drop filtering to demonstrate a four-wavelength by 10-fiber VCSEL-based transmitter in a pin grid array (PGA) package with mechanical transfer (MT)-connectorized optical output.[2]

A schematic diagram and photograph of the four-wavelength parallel fiber transmitter are shown in **Fig. 1**. It consists of four single-wavelength VCSEL arrays fabricated from separately-processed wafers, emitting near 825, 845, 977, or 988 nm, fastened to a silicon optical bench submount. VCSEL chips are

cleaved such that the ~8-µm-diameter emitter active area is centered within 15 µm of the chip edge, so that two arrays can be placed back-to-back to directly couple to the 62.5-µm core diameter and 250-µm pitch of the fiber ribbon.

Dual-wavelength optical signals are separately collected in bands near either 830 nm or 980 nm. These two bands are then multiplexed using a fiber-guided add/drop filter, which is a parallel-fiber three-port device consisting of an AlGaAs/AlAs Bragg mirror embedded at 45° within a fiber ribbon rigidly encased in an MT ferule.[3] Vertical emission at the 830-nm band is reflected horizontally by the Bragg mirror and combined with 980-nm band light transmitted through the filter in the horizontal direction. A (nonmultiplexing) gold turning mirror, packaged in a similar fashion to the Bragg mirror, directs the vertical 980-nm band emission to the horizontal input of the add/drop filter. Together these turning and multiplexing optics form a fiber-guided superstrate with the four-wavelength output terminated in a MT connector.

Spectra for each of the ten output fibers of the fiber ribbon are plotted on a logarithmic scale in **Fig. 2**; VCSELs at all four wavelengths were simultaneously biased at 3 mA. Due to wire bonding difficulties, not all wavelengths were demonstrated for
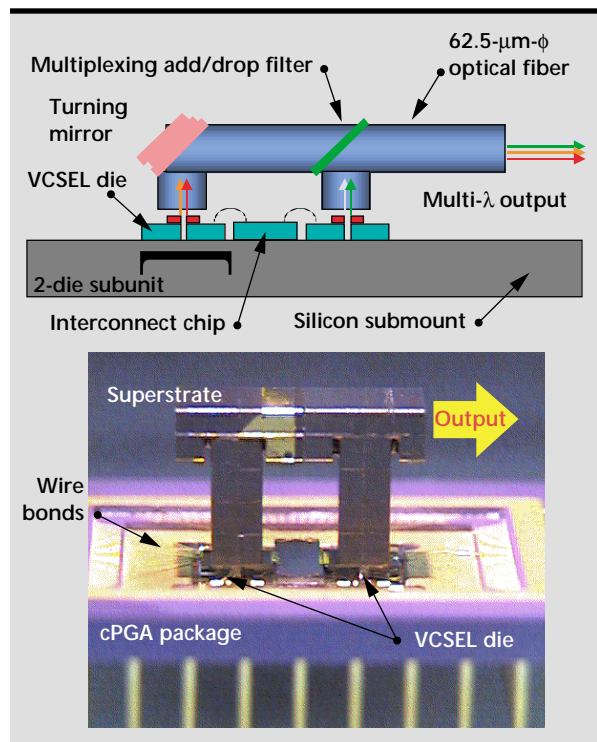

Figure 1. (top) Cross-sectional schematic diagram of the four-wavelength transmitter. This structure is repeated on a 250-µm pitch for each of the ten fibers comprising the fiber ribbon; (bottom) photograph of the completed module.

all fibers. Coupled output power as high as –2 dBm is achieved; the lower than expected power for the 977-nm emitter is likely due to misalignment. An eye diagram showing digital modulation at 1.25 Gbit/s under a 2^{23}-1 pseudo-random bit stream (channel #3, 988 nm) is plotted in **Fig. 3**.

Cross-talk between wavelengths and between fiber channels was studied using bit error rate testing. The bit error rate was measured as a function of

signal power over a link consisting of the multiwavelength transmitter modulated with a pseudo-random bit sequence at 1 Gbit/s and connected by fiber ribbon successively through a variable attenuator and a wavelength filter[3] to a commercial receiver. **Figure 4** shows the error rate on a particular fiber of the 825-nm channel with and without modulation of a 990-nm channel. Essentially, no cross-talk penalty is seen within experimental measurement limits. Furthermore, the lack of a power-independent noise floor indicates the absence of speckle noise. Similar results are observed for adjacent fiber-to-fiber cross-talk.

To achieve higher wavelength counts in a compact form factor requires the monolithic fabrication of multiple wavelengths per VCSEL chip to complement the hybrid packaging scheme described above. This leads to a total wavelength count equal to the product of the number of hybridly-multiplexed VCSEL chips and the number of wavelengths per chip. This year, we have developed several different approaches that selectively shift the lasing wavelength by altering the VCSEL's effective cavity length. A major challenge is satisfying the requirements of (1) a tightly-spaced multiple-wavelength cluster
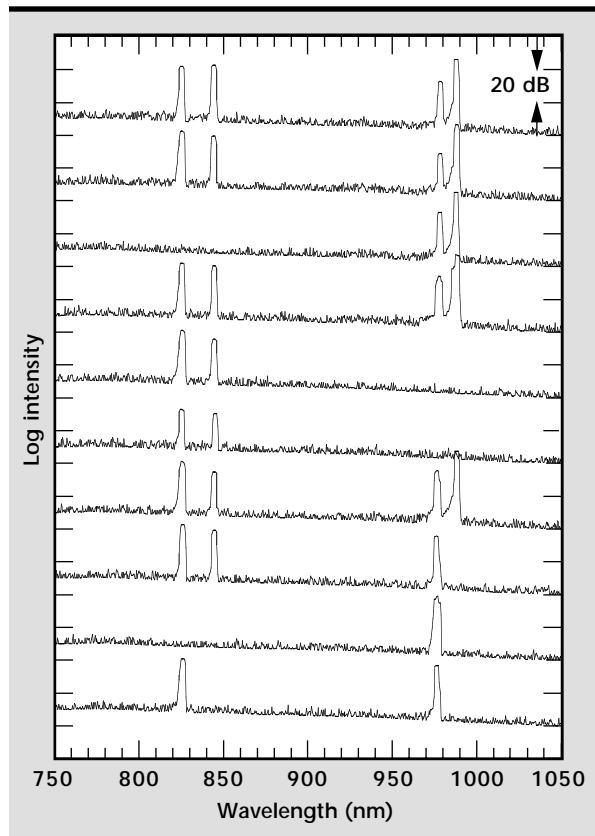

Figure 2. Output spectra for each fiber with VCSELs simultaneously biased at 3 mA each. Note that the spectrum is displayed on a logarithmic (decibel) scale.
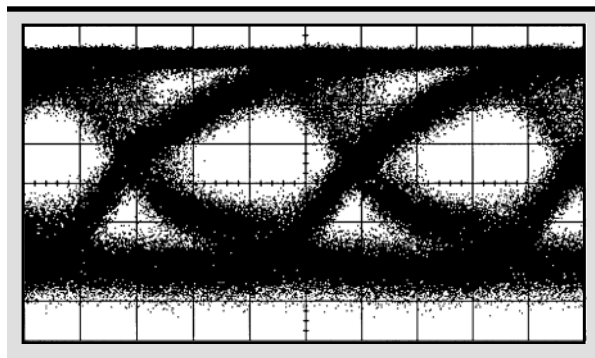

Figure 3. Eye diagram at 1.25 Gbit/s of fiber channel #3, 988 nm. The vertical axis is signal level and the horizontal scale is 200 ps/div.
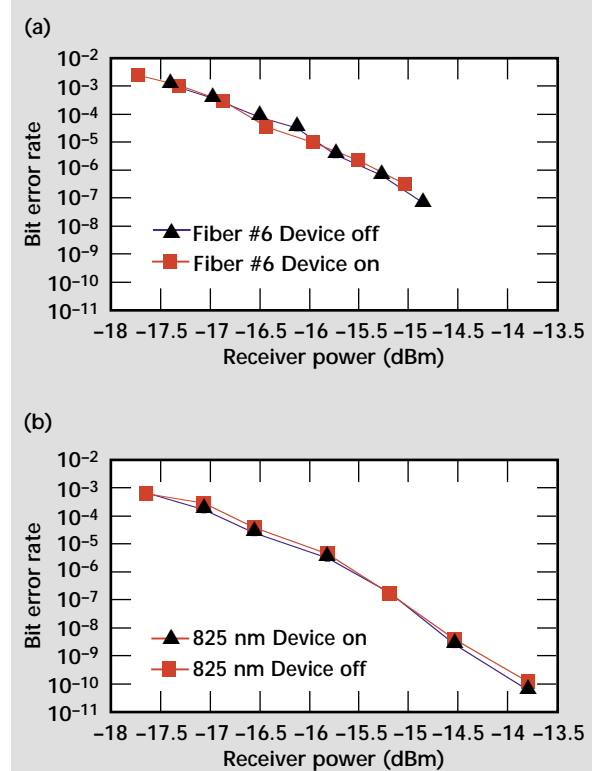

Figure 4. (a) Wavelength-to-wavelength (single fiber) and (b) fiber-to-fiber (single wavelength) bit error rate measurements vs. received optical power. The deviation between curves is within experimental error.

such that all emitters in the cluster can be efficiently coupled to one multimode fiber, (2) repeating this structure for each fiber in the ribbon, and (3) a controllable, manufacturable fabrication process.

Figure 5 shows our first results using a technique whereby the physical cavity length is etched before deposition of the top mirror. Lasing spectra were obtained for two emitters—one of which had its cavity layer etched—spaced apart by a center-to-center distance of only 27 µm, allowing for straightforward coupling of both devices to the 62.5-µm fiber core diameter. Each of these two-wavelength clusters was furthermore repeated on a 250-µm pitch for

direct coupling to byte-wide multimode fiber ribbon cable. A wavelength shift between emitters of 8.9 nm was demonstrated, within our targeted wavelength separation of 8 to 10 nm required for ease of system tolerancing. The degraded lasing efficiency shown on the left of **Fig. 5** is attributed to the non-optimized device geometry. Subsequent devices are expected to show better efficiency.

We have also explored a proprietary technique for adjusting the VCSEL cavity length after a single-step growth process. This development can vastly simplify the demanding thickness control requirements otherwise needed when these arrays are fabricated with
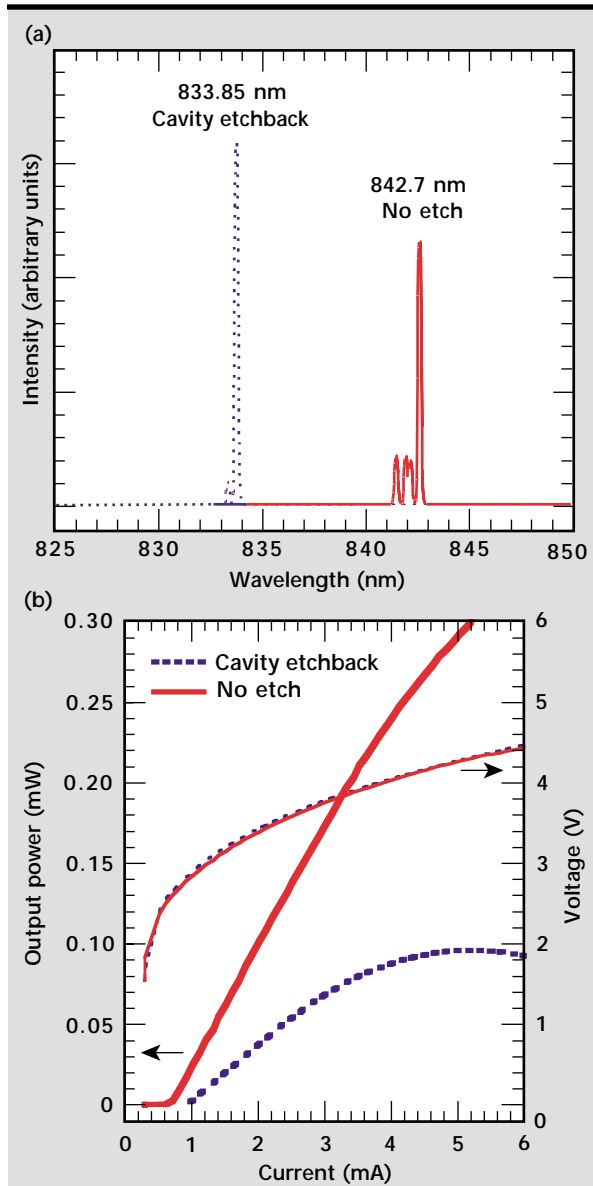
Figure 5. (a) Spectral and (b) output characteristics of first-generation monolithic WDM VCSELs using cavity etchback and multistep growth. Notice that the spectrum is plotted on a linear scale.
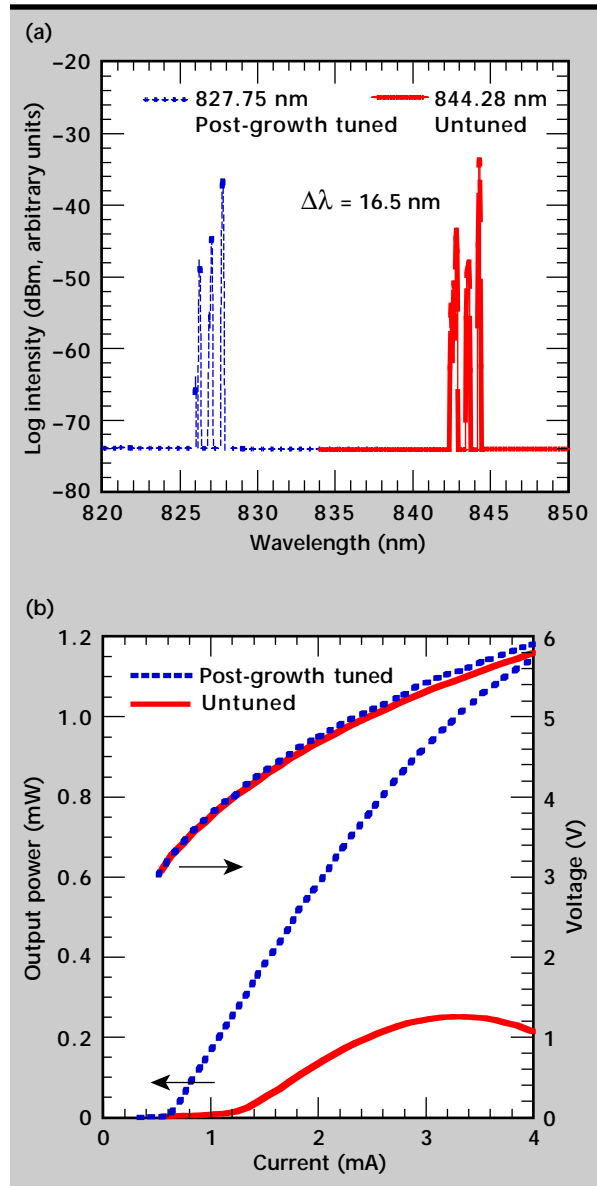

Figure 6. (a) Spectral and (b) output characteristics of first-generation monolithic WDM two-emitter VCSEL cluster using single-step growth followed by post-growth tuning of one of the devices. Notice that the spectrum is plotted on a decibel scale.

two separate growths. Initial characteristics for arrays fabricated with a similar layout as described above are shown in **Fig. 6**. A wavelength shift of 16.5 nm is considerably larger than the required 8 to 10 nm, indicating the potential of this approach for wide wavelength spacing. Current work is underway to extend these monolithic approaches to yield four wavelengths per single-fiber cluster with uniform characteristics across wavelengths.

Long-Wavelength VCSELs

Our transmitter modules have spanned the near IR spectrum with wavelengths ranging from approximately 800 to 1000 nm. For an 8 to 10 nm channel spacing, this yields a maximum possible channel count of 21 to 26 wavelengths, assuming no gaps and even spacing. To scale beyond this, we need to either choose a smaller channel spacing, which can negatively impact system robustness as discussed earlier, or use a larger portion of the spectrum. Extending to longer wavelengths is especially attractive because of improved performance of silica optical fiber, particularly at 1300 nm and beyond. Unfortunately, InGaAs/GaAs-based VCSELs are limited by strain in the active layer to a lasing wavelength of at most ~1100 nm. However, although edge-emitting lasers with InGaAsP/InP-based active layers are commonly used for 1300- and 1550-nm telecommunications applications, this material system is not suitable for fabricating the high-performance mirrors required by VCSELs. Therefore, we are exploring the GaInNAs material system for use as a long-wavelength active layer that can be directly integrated with GaAs/AlGaAs-based mirrors. Since it is a direct extension of technology proven for 850-nm and 980-nm devices, it holds great promise for viable long-wavelength emitters.

This year we fabricated simple broad-area (50-μm-square, no-oxide aperture) GaInNAs VCSELs and demonstrated room-temperature pulsed operation. As shown in **Fig. 7**, devices emitting at 1200 nm exhibited threshold currents as low as 68 mA (current density 2.7 kA/cm^2), slope efficiency above 0.06 W/A, and peak power above 17 mW. Although threshold current density is still approximately a factor of 3 higher than comparable shorter-wavelength InGaAs designs, these results represent the best yet reported for GaInNAs. Improved material crystallinity, mirror design, and use of advanced oxide-apertured geometry should yield small-area devices with considerably lower threshold currents.

Wavelength Router Development

Our original system concept used a simple broadcast element and wavelength bandpass filtering to achieve the multi-bus or crossbar implementation of the LambdaBus architecture, through a "broadcast and select" approach. A potential problem with this approach is that optical signal is wasted. With N ports and optical power at the transmitter of P, any given receiver will only receive P/N optical power. Recently, however, we conceived a power efficient wavelength routing fabric which routes a particular input port and wavelength to one particular output port rather than broadcasting to all output ports simultaneously. The multimode nature of our fiber
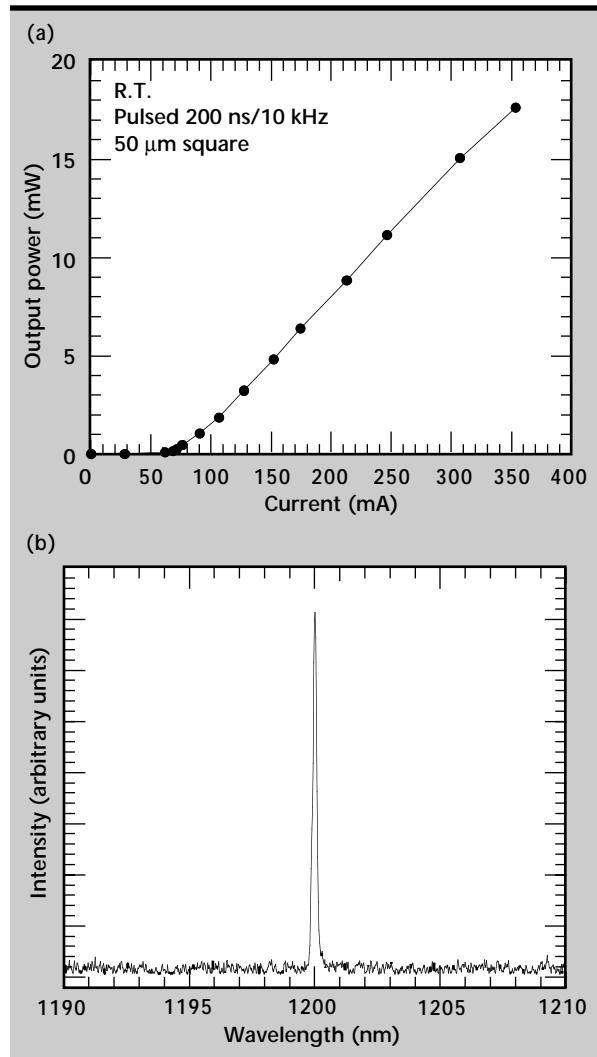

Figure 7. (a) Output power vs. injection current and (b) lasing spectrum near threshold for a GaInNAs long-wavelength VCSEL.

transmission medium prevents the use of existing arrayed waveguide grating router technology, which for single-mode fiber provides passive wavelength routing, with spectral channels being used more than once in the routing table to achieve full N-×-N interconnection with only N wavelengths.

This year, we have developed a wavelength router (N-×-N-wavelength multiplexer) for use in multimode fiber based optical networks. The device uses a blazed diffraction grating and broadband add/drop filters to provide wavelength re-use thus enabling fully non-blocking N-×-N interconnection with only N wavelengths. First, we demonstrated[4] a single-bit wavelength router with three spectral channels, resulting in a 3-×-3 fully non-blocking crossbar switch. However, to make use of wavelength routing for parallel optical interconnects a byte-wide wavelength router is required. Therefore, we also demonstrated a bit-parallel wavelength router by building upon the single-bit 3-×-3 wavelength router. Using a

ferrule with two parallel arrays of 12 fibers each, we have demonstrated a 3-input by 3-output wavelength router where each input/output channel is two bits wide. The device provides fully non-blocking interconnection between all inputs and outputs and shows virtually no bit-to-bit cross-talk.

Figure 8 shows the Routing Table for both bit-lines of the router. As seen in the figure, each output port receives all three spectral channels; however, each spectral channel comes from a different input port. (The letters next to each spectral channel on the plots indicate input ports labeled A, B, and C, or outputs labeled X, Y, and Z.) Bit-to-bit cross-talk was measurement limited at below -30 dB.

Future Work

The results described above demonstrate the required building blocks for high-performance, byte-wide, multiwavelength optical interconnects. We

Figure 8. Bit-parallel wavelength routing demonstrated with our initial 3-×-3-port prototype.
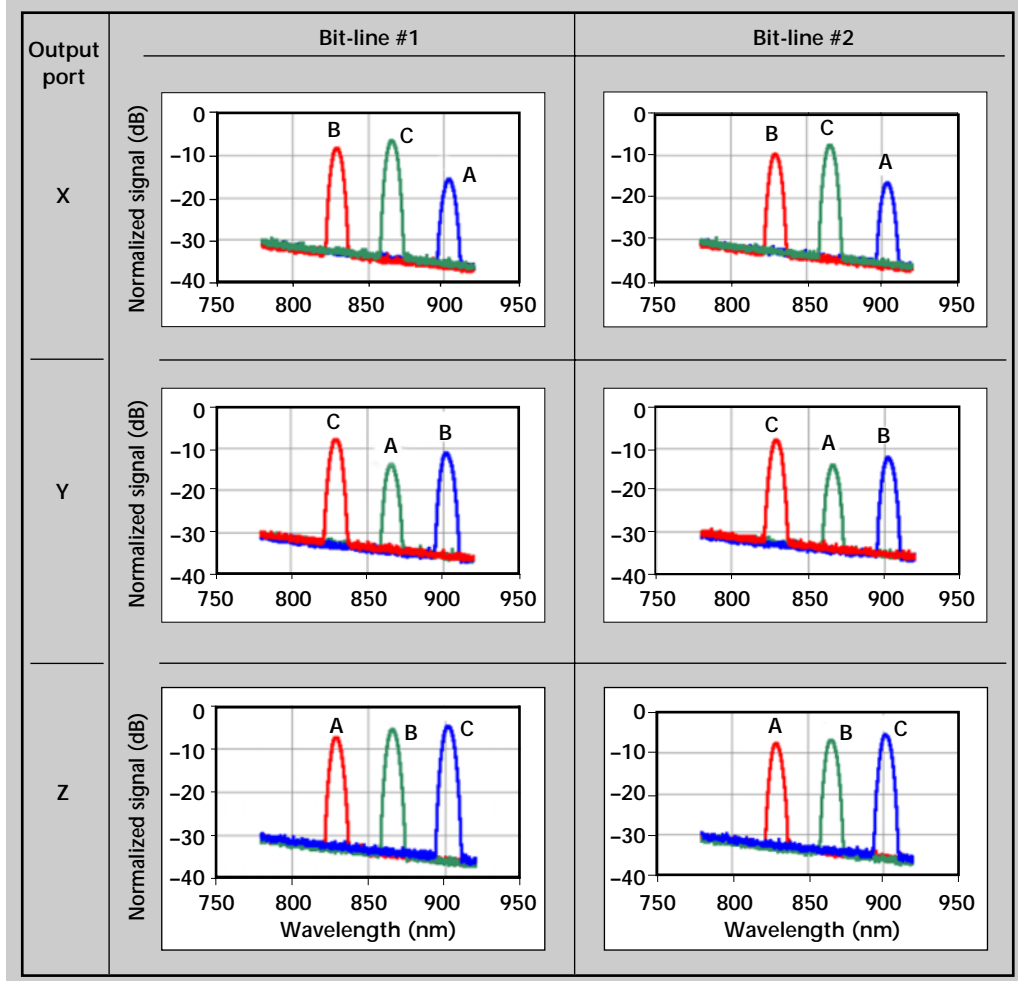
have shown low cross-talk in four-wavelength transmitters fabricated by hybrid integration, as well as demonstrating monolithic processes for achieving multiwavelength emitter arrays on a single chip. In addition, we have realized a bit-parallel wavelength router for a more efficient connection architecture.

Our goal for next year is to demonstrate manufacturable components enabling systems with higher wavelength count by combining our hybrid and monolithic integration approaches. Earlier simulations showed that eight system wavelengths are required for several interesting multiprocessing applications.[1] We also intend to extend our wavelength router to eight parallel bit-lines for a byte-wide interconnect, and to eight or more spectral channels.

Acknowledgments

References

1. A. J. DeGroot and R. J. Deri, *et al.* (1996), *IEEE Proc. Third Intl. Conf. Massively Parallel Processing using Opt. Interconnections*, October.

2. M. C. Larson, M. D. Pocha, H. E. Garrett, H. E. Petersen, S. W. Bond, R. F. Drayton, R. R. Patel, M. A. Emanuel, R. J. Deri, and M. E. Lowry (1999), "Multiwavelength VCSEL transmitter for WDM parallel optical fiber interconnects," *IEEE Lasers and Electro-Opt. Soc. Ann. Meeting,* San Francisco, California, November.

3. R. R. Patel, H. E. Garrett, M. A. Emanuel, M. C. Larson, M. D. Pocha, D. M. Krol, R. J. Deri, and M. E. Lowry (1999), "Compact, low-crosstalk, WDM filter elements for multimode ribbon fiber data links," *Forty-Ninth Elec. Comp. and Tech. Conf.,* San Diego, California, June.

4. R. R. Patel, S. W. Bond, M. C. Larson, M. D. Pocha, H. E. Garrett, and M. E. Lowry, "Multi-mode fiber coarse WDM grating router using broadband add/drop filters for wavelength re-use," *IEEE Lasers and Electro-Opt. Soc. Ann. Meeting,* San Francisco, California, November.

Low Power Wireless Modem Technology

Charles F. McConaghy
Electronics Engineering Technologies Division
Electronics Engineering

Charles Chien
University of California at Los Angeles
Los Angeles, California

A key component in spread spectrum RF systems is the modulator/demodulator (modem). We have developed a modem based on a state-of-the-art field-programmable gate array which is customized for wireless sensor applications.

Introduction

To reduce the size and power of RF communication systems for wireless sensor networks, a custom direct sequence spread spectrum transceiver was built.[1] The total RF system consists of an RF section which up-converts transmitted signals and down-converts received signals, and a modem which processes these signals. The modem takes an incoming data stream and mixes it with a pseudo-random sequence. This complex signal then phase-modulates the transmitter. On receive, or demodulation, a reciprocal process is used. However, additional complexity is required during demodulation since the phase relationship between the transmit and receive pseudo-random codes is not known and varies with signal propagation.

Part of the modem circuitry locks on a header and then stays locked via a control loop for the duration of the transmitted data packet. Such modems can be built as a custom applications-specific integrated circuit (ASIC) chip or in a field programmable gate array (FPGA). The latter has the option that design iterations can be made with no change in the hardware. Although ASICs have ultimately the smallest size and lowest power, recent advances in FPGA are yielding near comparable performance to ASICs with the advantage that such devices are re-programmable.

Progress

Initial work focused on development and reiteration of modem designs with hardware developed during FY-98. This is largely a software effort with the designs downloaded to the FPGA from a PC. After debugging, the software was transferred to an on-board boot PROM. The initial design was developed around a Xilinx XC4062XL FPGA. This 240-pin, 62,000-gate device comes in a package that is 35 × 35 mm. The modem was designed for a processing gain of 127 with a chip rate of 1 MHz. This results in a data rate of 7.8 kbits/s, which was sufficient for our wireless sensor needs.

The FPGA ability to quickly reiterate the modem design was an important aspect of this development. In the initial design the FPGA also took care of non-modem tasks such as reading an A/D converter, buffering data, and transmitting packet headers. This modem was interfaced to a 900-MHz RF board. Performance was demonstrated by transmitting accelerometer sensor data from a 2-in.-×-2-in.-×-2-in. module to a host computer where the data was displayed with Labview.

In FY-99 a second design was begun which used a smaller 10,000-gate FPGA. This design makes use of Xilinx XCS20XL 100-pin device which is in a package 14 × 14 mm. The use of the smaller package

allowed us to build the next generation wireless sensor module which uses boards that are 30 × 50 mm. The new modem design is expected to use one fifth of the power of the initial design. The higher level functions such as A/D conversion and packet formation have been moved from the FPGA and relegated to another controller within the wireless sensor module, allowing more versatility in the programming of the overall module. Although similar in design to the original modem, more finesse was required to make use of the smaller FPGA. An additional feature of the newer modem is the ability to program the processing gain with bit rates from 7.8 to 90 kbits/s Yet an additional feature of the new modem is the ability to power down the FPGA without having to reboot on power-up. This latter feature is being incorporated into the overall power management within the module.

Future Work

We are in the evaluation stage of the new modem design. We are making tests of power consumption as well as data transmission reliability. On-the-air tests will be made with the modem board interfaced to two custom designed boards, a dual conversion 900-MHz RF board and a controller-signal processing board which reads the sensor.

In the coming year we will further evaluate the current design and port the design from FPGA to a custom ASIC.

Reference

1. A. P. Lee, C. F. McConaghy, and J. N. Simon, "Wireless microsensor modules for distributed network sensing," Lawrence Livermore National Laboratory, Livermore, California (UCRL-LR-113717-98), pp. 1–10.

Wireless Micropower RF Components

Charles F. McConaghy
Electronics Engineering Technologies
Electronics Engineering

Battery size is the main limitation to producing small volume RF systems such as those used by the wireless sensor project[1]. This work has focused on power reduction techniques in receiver architectures as well as RF components such as oscillators and mixers, to enable the use of small size batteries.

Introduction

The RF section of modern spread spectrum transceivers uses a number of building blocks such as mixers, low noise amplifiers, phase locked loops, and oscillators. All of these components consume current. Generally receivers are more complex than transmitters but in many applications, transmitters dissipate more electrical power, with most of this power dissipated in the power amplifier used to amplify RF signals to the 1 W power regime. However, in low power applications where transmit power is on the order of a milliwatt and in networks which transmit with a low duty cycle, the receiver becomes the dominate electrical drain.

Table 1 shows the current requirements for two 3.3-V, 900-MHz RF transceivers. This data was obtained from specifications of state-of-the-art oscillators, mixers, and phase lock loops (PLL) as well as a single chip transceiver built in RF complementary metal oxide semiconductors (CMOS).[2] The important thing to note from the table is that the total receiver current drain (73 mA and 66 mA) is similar in both implementations. Even though the

single chip solution is a physically smaller implementation both require the same battery which dominates the physical size of the overall package.

In addition, receivers that use more complex modulation schemes such as binary or quaternary phase shift keying (BPSK or QPSK) have more parts and subsystems than simpler modulation techniques such as frequency shift keying (FSK) or on-off keying (OOK). The more advanced modulation techniques are more robust but usually come at the price of higher current consumption and additional parts. Most direct sequence spread spectrum transceivers use some form of phase modulation for modulating the RF carrier. It was one of the goals of this work to still make use of phase modulation but to reduce the complexity and power required in these receivers.

Progress

BPSK is accomplished by changing the phase of the RF signal by 180° for a logical one and leaving the phase unchanged at 0° for a logical zero. This is fairly easily accomplished on the transmit side with a single component such as a balanced mixer.

Table 1. Comparison of current* requirements for single chip RF CMOS vs. multi-chip transceivers.

	LNA	Divider	VCO	PLL	Mixer	PA	IF Amp	Misc.	RX/TX Total
RF CMOS	15 RX	14 RX	13 RX/TX	14 RX/TX	8 RX/TX	28 TX	7 RX	2 RX	73/63
RF COTS	8 RX	NA	9.5 RX/TX	7 RX/TX	23 RX/TX	35 TX	8.5 RX	10 RX	66/74.5

*Current in milliamps

Figure 1. Block diagram of BPSK receiver with differential delay line. Waveforms are shown at several places within the receiver.
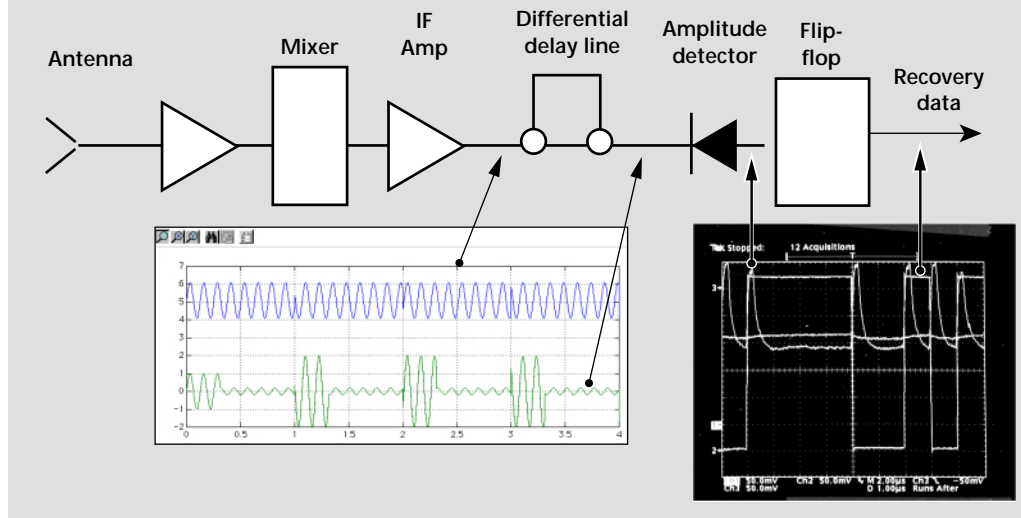
However, the typical demodulation technique on the receiver side usually requires mixing a reference source with the modulated received signal. The output of this mixer is the recovered data. The reference oscillator generally needs a control loop which adds to the complexity and current consumption of the overall receiver.

One of the accomplishments of this year's work has been a simpler receiver architecture for a BPSK receiver. **Figure 1** shows a block diagram for this receiver. The key feature of this design is the absence of a reference oscillator. Instead, a differential delay line is used to pick up the edge transitions of each phase change. The delay line is adjusted to give a 180° phase change and when summed with the direct path yields no output. However, due to the delay, a phase transition causes the output to be non-zero for a short time. Therefore, each phase transition results in a pulse output. These pulses, when used to edge trigger a flip-flop, yield a regenerated data stream. A nice feature of this technique is some frequency offset between the transmitter and receiver can be tolerated. This means high-stability oscillators are not a requirement and lower power oscillators can be used.

Although **Fig. 1** shows the differential delay line being used at an intermediate frequency, it is possible to directly use the delay line at the RF frequency, which allows for very simple receivers. We demonstrated such a receiver which used four stages of RF amplifiers and a differential delay line implemented with a surface acoustic wave (SAW) filter as the delay element. Although this receiver was not as sensitive as one which uses an intermediate frequency amplifier, it did perform well enough for short range
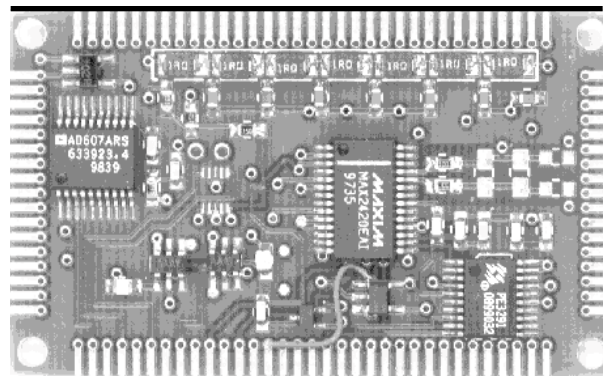

Figure 2. BPSK transceiver implemented on a 30-mm-×-50-mm board.

applications. The receiver was quite simple as it avoided the use of both oscillators and mixers.

Figure 2 shows a more sensitive intermediate frequency amplifier receiver we built that was based on an L/C delay line. This receiver occupies a 30-mm-×-50-mm board and also contains transmitter circuits. The power requirements are 3.3 V at 60 mA. Further power reduction is anticipated from duty cycling as the receiver has a power down mode, which reduces current drain to under 10 mA.

Future Work

To further reduce power we have designed a system which has the main receiver powered down and has a parallel very low current receiver (2 mA) which just detects the presence or absence of RF. This parallel receiver would then be used to switch on the main receiver only when needed. It is anticipated that this type of power reduction can provide a factor of ten improvement in battery life. We hope to test this idea experimentally in the near future.

References

1. A. P. Lee, C. F. McConaghy, and J. N. Simon (1998), "Wireless microsensor modules for distributed network sensing," Lawrence Livermore National Laboratory, Livermore, California (UCRL-LR-113717-98).

2. H. Samueli, A. Abidi, G. J. Pottie, and Y. Rhamat-Samii, "Hardware technologies for robust personal communications transceivers," *http://www.icsl.ucla.edu/aagroup/PDF_files/900MHz.pdf*.

Acoustically-Driven Microfluidic Systems

Amy W. Wang, William J. Benett, and Christopher D. Fuller
Electronics Engineering Technologies Division
Electronics Engineering

Richard G. Couch
Defense and Nuclear Technology

We have demonstrated a non-contact method of concentrating and mixing particles in a microfluidic chamber using acoustic radiation pressure. A flow-cell package has also been designed that integrates liquid sample interconnects, electrical contacts and a removable sample chamber. Experiments were performed on 3-, 6-, and 10-μm polystyrene beads. In addition, finite element modeling has been used to predict pressure profiles in fabricated chambers. Flow cell designs to maximize acoustic energy coupling into the chamber and generate standing acoustic waves have been fabricated and tested.

Introduction

The threat of chemical and biological warfare agents has made apparent the need for autonomous, portable, and fast pathogen detection systems. Sample pre-treatment is one of the most critical aspects in the development of autonomous systems, yet it remains largely an unsolved problem. Sample handling is also of key interest in private industry. The global market for microelectromechanical systems (MEMS) is currently estimated at $10 billion, with biological and medical MEMS representing the most rapidly growing sector. The medical arena brings the additional challenges of disposability and low cost. Emerging MEMS-based companies are targeting miniaturized microfluidic systems that are able to perform a complete bioassay on what is loosely defined as a "chip." A necessary goal of these systems is to obviate manual handling of samples, which is slow, requires trained personnel, and is not cost-effective. Integrated sample preparation requires a high degree of functionality to truly permit biological or chemical analysis to be performed in a miniaturized system, yet the danger of sample-to-sample contamination dictates inexpensive, disposable parts. Typically the cost of a part increases with its functionality.

Acoustic forces can be used for concentrating, mixing, sorting, and transporting particles in disposable sample chambers. The use of remotely-coupled acoustic energy into a micromachined chamber combines high functionality with an inexpensive, disposable sample chamber. A bulk PZT transducer can be used multiple times as the source of acoustic energy, while the sample chamber can be inexpensively processed and thrown away after one use. In addition, acoustic forces act over a volume, are not media-dependent, allow the manipulation of uncharged and opaque particles, and do not require integrated electrodes or magnetic beads. Thus, acoustic actuation provides features that are not met by electroosmotic, electrophoretic, dielectrophoretic, electrohydrodynamic, magnetic, or optical techniques.

Acoustic radiation pressure exerts a force on a particle. Radiation pressure generated in the presence of a standing wave induces a pressure field that forces particles to collect in the nodes or anti-nodes of the standing wave. The acoustic force exerted on a particle can be expressed as,

$$F_{ac} = -4\pi/3 \ R^3 kEA \sin(2kx),$$

where R denotes the particle radius, k is the wave number, and E is the acoustic energy density.[1–5] The compressidensity factor, A, reflects the relative density and compressibility of the particle with respect to the ambient medium, and the sign of A determines whether the particles concentrate in the nodes or the anti-nodes of the standing wave. It follows that acoustic radiation pressure can be used to differentiate particles based on their size and their material attributes.
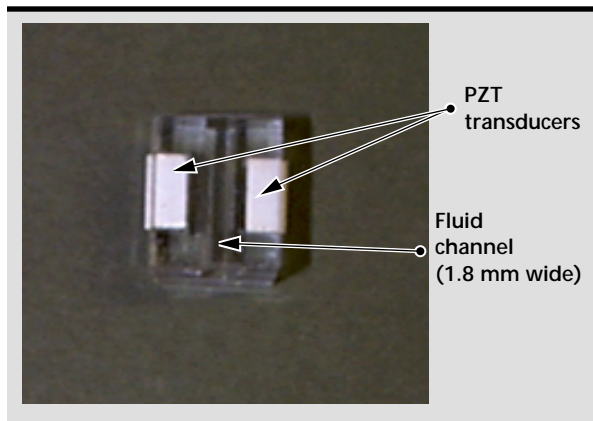
Figure 1. Photograph of prototype device for acoustic particle manipulation.

Figure 2. Evidence of bead mixing.

Progress

We have tested a prototype device for acoustic-based particle manipulation. The device consisted of a single half-wavelength width fluid channel (**Fig. 1**).

Mixing (**Fig. 2**) and concentration (**Fig. 3**) of polystyrene beads were observed in water. PZT transducers were driven at 20 Vpp. Degassing of the water was not required. **Figure 3** shows concentration of 10-μm polystyrene beads at the center of the fluid channel, an expected pressure node of the standing wave. Also shown in **Fig. 3** is separation of particles based on size. The larger beads collect at the central node of the channel, while smaller, 3-μm beads remain dispersed in solution. Bead concentration times were on the order of minutes.

To better understand the observed mixing phenomenon, we performed finite element modeling of the fluid channel geometry. One-dimensional models verified generation of a standing pressure wave given the geometry of the chamber. Three-dimensional models showed a distribution of pressure
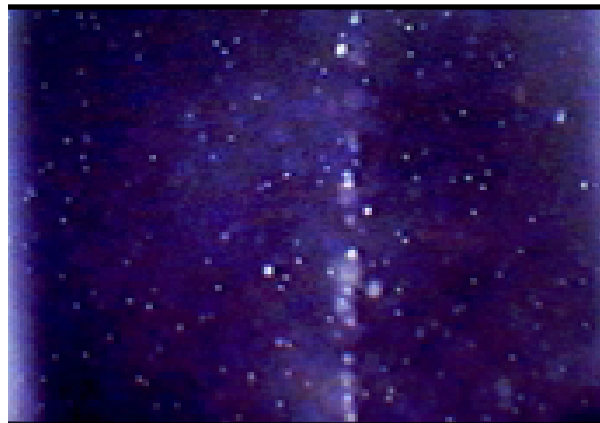

Figure 3. Evidence of size-preferential bead concentration.

across the length of the fluid channel, specifically, a higher pressure profile at the center of the wall, with decreasing energy radiating towards the channel ends. We believe this is due to the mechanical clamping at the ends of the chamber wall, which appears to cause a circular mixing motion at the clamped wall interface.

Summary

Mixing and concentration of particles in fluids have been shown in a microfabricated sample chamber with a flow cell package. We have tested prototype designs that indicate preferential geometry for mixing versus concentrating functions.

Acknowledgments

References

1. L. V. King (1934), *Proc. Roy. Soc., A*, **147**(212).

2. K. Yosioka and Y. Kawasima (1955), "Acoustic radiation pressure on a compressible sphere," *Acustica*, **5**, 167–173.

3. K. Yasuda, K. Takeda, and S. Umemura (1996), "Studies on particle separation by acoustic radiation force and electrostatic force*," Jpn. J. Appl. Phys.*, **35**, 3295–3299.

4. M. Whitworth, A. Grundy, and W. T. Coakley (1991), "Transport and harvesting of suspended particles using modulated ultrasound," *Ultrasonics*, **29**, 439–444.

5. W. H. Benett and P. Krulevitch (1999), "Flexible packaging and interconnect scheme for microfluidic systems," *Proc. Micro- and Nanofabricated Structures and Devices for Biomedical Environmental Applications*, San Jose, California, 111–118.